Université catholique de Louvain
École polytechnique de Louvain
Institute of Mechanics, Materials and Civil Engineering

Adhesion of thin films on steel and separation of the energy contributions

---

Thèse présentée par
François Strepenne
en vue de l'obtention du grade de
Docteur en Sciences de l'Ingénieur

Composition du jury

Prof. Thomas Pardoen (promoteur)	Université catholique de Louvain, Belgique
Prof. Jean-Pierre Raskin (copromoteur)	Université catholique de Louvain, Belgique
Dr. Muriel Braccini	Université de Grenoble, France
Ir. Philippe Harlet	ArcelorMittal Liège Research, Belgique
Prof. Alojz Ivankovic	University College Dublin, Ireland
Prof. Joris Proost	Université catholique de Louvain, Belgique
Prof. Grégoire Winckelmans (Président)	Université catholique de Louvain, Belgique

Louvain-la-Neuve, Décembre 2010

à Éthan

Abstract

Surfaces are more and more used to add specific properties to materials towards multifunctional systems. These properties are introduced using thin coatings deposited on the bulk material. Reliability is of prime importance for these systems and adhesion is one of the most important parameter to control and optimize. Thin films are usually deposited using physical or chemical processes. Understanding the influence of the deposition parameters on the adhesion is a very challenging issue.

Methods to properly measure the adhesion are not widely used in the industry due to experimental and conceptual difficulties. Fracture approaches to measuring, describing or predicting thin film adhesion essentially remain an academic field of research. The objective of this thesis has been to conciliate these two different viewpoints. A simple and versatile adhesion testing method, known as the wedge opening test, has been developed with a robust data reduction scheme. A plate identical to the substrate is bonded on top of the film to allow the insertion of the wedge. The adhesion is determined using geometrical parameters only without the need to a force measurement. The most difficult parameter to measure, in the case of non transparent substrate, is the crack length. An original method based of the out-of-plane displacement field of the specimen has been validated and extensively used during this thesis.

A steady-state finite element code is used to simulate the test and to study the contribution of each layer to the total fracture energy as well as to assess the model used to extract the crack length from the specimen displacement profile. The influence of the adhesive layer used to bond the extra adherent and the influence of the internal stress of the coating have also been addressed.

The simulation code allows the determination of the contribution of each layer to the total fracture energy. Specific attention is paid to the contribution of the adhesive layer which is extrinsic to the system. The dissipation in the adhesive layer can be as high as 2/3 of the total energy dissipated in the specimen during crack propagation, in the case of film thicknesses lower than 1 μm.

The methodology has been applied to TiN and Cu films produced by the company ArcelorMittal showing the complex couplings between surface treatment chemical and statistical effects, internal stress and thickness effects.

Remerciements

Quand vient le moment d'écrire les remerciements, beaucoup de noms viennent à l'esprit directement car, même si un seul nom figure sur la couverture, beaucoup de personnes m'ont aidé durant ces quatre années. Il ne me serait pas possible de les nommer toutes mais ces quelques lignes sont écrites pour chacun d'eux. Toutes ont été importantes à l'accomplissement du travail qui se trouve résumé dans cette thèse.

Merci tout d'abord à mes deux promoteurs, Thomas Pardoen et Jean-Pierre Raskin. Ils m'ont permis d'avancer sur le bon chemin tout au long de cette thèse. Thomas, tu as toujours été disponible pour parler sciences ou détendre l'atmosphère. De plus, on est toujours plus motivé en sortant de ton bureau qu'en y rentrant (quel que soit l'état d'esprit dans lequel on s'y rend). Jean-Pierre, tu as toujours eu de bons conseils à me donner grâce à tes connaissances complémentaires à celles de Thomas.

La collaboration avec les personnes du centre de recherche d'ArcelorMittal à Liège a été très importante. Claire Poirier et Philippe Harlet, vous avez suivi ce projet avec beaucoup d'attention et je me suis vraiment senti épaulé. Merci aussi à Jean-Baptiste Richir et à tous les techniciens du NCT qui m'ont aidé à réaliser les échantillons nécessaires.

Je voudrais aussi remercier le labo Termo de l'université de Grenoble qui m'a accueilli pendant quelques mois et plus particulièrement Michel Dupeux et Muriel Braccini qui ont fortement contribué à la réalisation de cette thèse. Ces quelques mois passés à l'étranger sont inoubliables grâce à toutes les personnes du labo et surtout aux doctorants.

Le programme de simulation Éléments Finis utilisé lors de ce travail a été fourni par Philippe Martiny du Cenaero. Je le remercie pour le

temps qu'il a passé à m'expliquer les détails du programme ainsi que les modifications qu'il a réalisées pour l'adapter aux besoins de ma thèse.

Merci à tous mes collègues d'IMAP. Il y a eu beaucoup de changements dans l'équipe de chercheurs mais l'ambiance est toujours aussi bonne, autant pendant les heures de boulot que lors des activités organisées en dehors. Merci tout particulier à Marc, Émile et Laurence pour leur aide.

Merci à toute ma famille de m'avoir soutenu durant ces années de doctorat. Je remercie tout particulièrement ma Nanou qui est toujours à mes côtés en toute circonstance, depuis beaucoup plus que quatre ans. Enfin, last but not least comme on dit chez nous, tu es arrivé pour m'encourager tout au long de la période de rédaction, merci Éthan pour ta bonne humeur quotidienne et tes premiers mots encourageants.

Contents

List of Symbols

α	first Dundur parameter	$[-]$
α^{th}	thermal expansion coefficient	$[\mathrm{K}^{-1}]$
A	crack area	$[\mathrm{m}^2]$
a	crack length	$[\mathrm{m}]$
β	second Dundur parameter	$[-]$
b	Burger vector	$[\mathrm{m}]$
C	substrate curvature	$[\mathrm{m}^{-1}]$
δ	blister height	$[\mathrm{m}]$
D	wedge thickness	$[\mathrm{m}]$
d	grain size	$[\mathrm{m}]$
ε	strain	$[-]$
E	Young's modulus	$[\mathrm{GPa}]$
Γ_0	work of adhesion	$[\mathrm{J/m}^2]$
Γ_p	plastic dissipations	$[\mathrm{J/m}^2]$
γ_s	surface energy	$[\mathrm{J/m}^2]$
Γ_x^{y}	energy dissipated in layer "y"	$[\mathrm{J/m}^2]$
$\mathcal{G}$	energy release rate	$[\mathrm{J/m}^2]$

$\mathcal{G}_c$	interface toughness	$[\,\mathrm{J/m^2}\,]$
$\mathcal{G}$	energy release rate associated to the external loading	$[\,\mathrm{J/m^2}\,]$
$\mathcal{G}_{ss}$	steady state energy release rate	$[\,\mathrm{J/m^2}\,]$
h	substrate thickness	$[\,\mathrm{m}\,]$
K	stress intensity factor	$[\,\mathrm{MPa}\sqrt{\mathrm{m}}\,]$
μ	shear modulus	$[\,\mathrm{GPa}\,]$
M	bending moment	$[\,\mathrm{Nm}\,]$
ν	Poisson ratio	$[\,-\,]$
n	strain hardening exponent	$[\,-\,]$
ψ	mode mixity	$[^\circ\,]$
P	loading	$[\,\mathrm{N}\,]$
p	pressure	$[\,\mathrm{Pa}\,]$ or $[\,\mathrm{bar}\,]$
σ_i	internal stress	$[\,\mathrm{MPa}\,]$
σ_y	yield strength	$[\,\mathrm{MPa}\,]$
σ_{ij}	component of the Cauchy stress tensor	$[\,\mathrm{MPa}\,]$
t	coating thickness	$[\,\mathrm{m}\,]$
w	specimen width	$[\,\mathrm{m}\,]$

Part I

Introduction

Chapter 1

General introduction

Thin films are widely used in microelectronics and microelectromechanical (MEMS) systems, as well as in a large variety of applications requiring specific surface properties. In the context of the present work, a film is defined as thin when the thickness is smaller than a few micrometers. Adhesion of thin films on a substrate or with other films within multilayer system is a critical issue in many applications. Thin films are usually deposited using physical or chemical processes. Understanding the influence of the deposition parameters on adhesion is a very complex problem. Furthermore, methods to properly measure the adhesion of thin films have been developed for many years but are still not widely used due to testing difficulties and definitely not transferred to the industry. Specifically, fracture mechanics approaches to measuring, describing, modelling or predicting thin film adhesion remain an academic field of research. Finally, the definition of adhesion itself remains an issue. Adhesion is defined on *Wikipedia* as "any attraction process between dissimilar molecular species that can potentially bring them in "direct contact"." It is a general definition, which does not give any information on what is measured and how to measure it. In the introduction of the book *"Adhesion measurement methods"* [37], Robert Lacombe begins with a basic definition of adhesion:

> "Now, from a commonsense point of view, one would like to think that adhesion is a simple matter of how well two

> different materials tend to stick together, and that adhesion measurement is some indication of the force required to separate them."

That is a good starting point but the author tries to build a scientific definition of the adhesion and three pages later, his conclusion is that:

> "At this point, we simply recognise that practical adhesion is some complex function of fundamental adhesion that we fortunately do not need to know under most circumstances. Furthermore, we recognise that the fundamental adhesion between two materials can be modified by physico-chemical means and is a powerful tool for modifying practical adhesion."

It is a good point for scientists, that adhesion is a complex phenomenon, not yet fully understood as it allows further interesting researches. From an industrial point of view, it is only a pity! Measuring adhesion is not as simple as pulling on a material specimen to measure the deformation and strength properties.

Hence, the first objective of this thesis is to develop, in collaboration with ArcelorMittal, a simple quantitative adhesion measurement method in the context of Fracture Mechanics. The development has been mainly made on the methodology of the wedge opening test and on the precise extraction of the crack length for non transparent substrates. The measurement of the crack length must be extremely accurate as it enters the expression of the energy release rate with a fourth power (see Section 3.2). The key idea is to set up a method based on the measurement of the vertical displacement profile of the specimen (over the entire crack length region). From all the points measured on the specimen, the crack length is determined. The fact that it is a field measurement and not a single point value, or a measurement taking into account only the near crack tip region, is an important contribution of this thesis. The confrontation between the scientific methodology and the industrial needs is also addressed to possibly provide a reliable adhesion testing method easily usable on coating factory.

In this thesis, we will often refer to the term "interface toughness". As will be explained in this manuscript, interface toughness is a measure of the necessary energy for crack propagation along an interface between two materials. During fracture, energy is stored and dissipated in the material, especially in the near crack tip region. The energy can come either from (visco-)elastic deformation, (visco-)plastic deformation, generation of defects and the generation of the new surfaces.

The second objective of this thesis is to provide a better understanding of adhesion by considering some parameters affecting the resistance of the interface and a scheme to separate the different energy contributions coming from the different parts of the specimen under loading. The total energy $\mathcal{G}$ entering the system to promote interface cracking can be divided into different contributions as

$$\mathcal{G} = \Gamma_0 + \Gamma^{\text{intrinsic}} + \Gamma^{\text{extrinsic}} - W(\text{relaxation of } \sigma_i) \ . \qquad (1.1)$$

This decomposition of $\mathcal{G}$ into several terms (which will be splitted in other sub-terms in Chapter 6) will be discussed in the last chapter of the thesis. Expression (1.1) provides the starting point to understand why adhesion is a complex system property. The total energy is the sum of three general contributions: the interface toughness ($\mathcal{G}_c = \Gamma_0 + \Gamma^{\text{intrinsic}}$), the extrinsic contribution due to the measurement technique and the contribution of the internal stress of the film giving energy available for cracking. Each contribution is still divided into the (visco-)elastic and (visco-)plastic dissipation of each part of the specimen. The terms of Eq. (1.1) are quantified separately by combining experimental and modelling approaches. A better appraisal of the different energy contributions, and, more specifically of the influence of the film internal stress as well as of extrinsic effects coming from the test design, is the second important contribution of this thesis.

The adhesion will be characterized by the interface toughness $\mathcal{G}_c$, which involves the thermodynamic work of adhesion Γ_0 as well as plastic deformation and elastic energy stored in the substrate and layers due to the cracking. The value measured by the experimental tests is different. It involves the interface toughness and possible extrinsic contributions.

This value, the energy release rate associated to the external loading, is designed by $\mathcal{G}$.

Finally, the third objective of this thesis is to use the testing methodology to improve the understanding of adhesion issues on specific systems produced by ArcelorMittal. The testing methodology has been first applied on TiN coating deposited on a stainless steel substrate. Secondly, copper coatings deposited on stainless steel have been tested. Variation of adhesion as a function of the coating thickness has been observed on copper coating. The goal of this study was to determine the reason of this variation, based also on the general analysis associated to the second objective.

The outline of the thesis is the following. The first part of the thesis is devoted to important background of fracture mechanics in Chapter 2. Chapter 3 provides a description of different adhesion testing methods that can be used for thin films: superlayer, blister, four-point bending and wedge opening tests.

The second part describes the adhesion testing methods used and developed during this PhD. The work has mainly been focused on the wedge opening test described in Chapter 4.

The third part addresses two different systems. Chapter 5 explains the development of the wedge opening test and the adaptations to measure thin film adhesion on a titanium nitride coating. Chapter 6 shows the work performed on the adhesion of thin copper coatings deposited on stainless steel. This chapter explains Eq. (1.1) using both experimental and numerical simulation results. Experimental results giving the evolution of $\mathcal{G}$ and the internal stress with the thickness are first addressed. Then, the properties of each layer are determined and used in numerical simulations. The simulations are first used to determine the influence of some parameters on the interface toughness. Secondly, simulations results are compared to the experimental values measured with the wedge opening test in order to separate the contribution of each layer to the global energy release rate. The interface toughness of the studied interface is then determined.

Chapter 2

Background on fracture mechanics

One of the primary goals of this thesis is to contribute to the development of testing techniques for measuring the interface toughness between a thin coating and the underlying substrate. Several testing methods will be developed in Chapter 3. All these methods are based on fracture mechanics to deduce the critical energy release rate needed for a crack to propagate along the interface. This chapter first presents some basis of linear elastic fracture mechanic (LEFM). The particular case of thin film fracture is considered in the second section, followed by thin film delamination.

This chapter borrows a lot of material from references [41, 55]

2.1 Basics of fracture mechanics

Consider a homogeneous material with an isotropic linear elastic behaviour containing a planar crack of length a. The configuration is shown in Fig. 2.1. The crack propagates along the x-axis with the y-axis perpendicular to the crack plane. The r and θ polar coordinates represent the distance and the angle from the crack tip in any plane perpendicular to the z-axis.

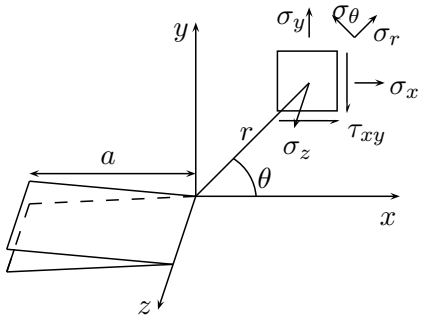

Figure 2.1: Definition of coordinates system and geometry of the crack.

The material is subjected to general loading. Locally, at the crack tip, the loading can be decomposed into the three modes shown in Fig. 2.2. Mode I is usually the most critical opening mode (meaning that the fracture toughness is usually the smallest in pure mode I), the loading is acting along the y-axis and opening the crack. Mode II corresponds to a shear loading parallel to the crack propagation direction and mode III corresponds to antiplane shear. Considering a linear elastic material, the intensity of the crack tip loading can be expressed as a linear combination of the three modes.

The stress field around the crack tip can be derived for each opening mode for isotropic linear elasticity. In this work, we only consider mode I and mode II loadings. The stress state near the crack is a superposition of the two modes writing

$$\sigma_{r\theta}(r,\theta) = \frac{K_{\mathrm{I}}}{\sqrt{2\pi r}} f^{\mathrm{I}}_{r\theta}(\theta) + \frac{K_{\mathrm{II}}}{\sqrt{2\pi r}} f^{\mathrm{II}}_{r\theta}(\theta) \ , \tag{2.1}$$

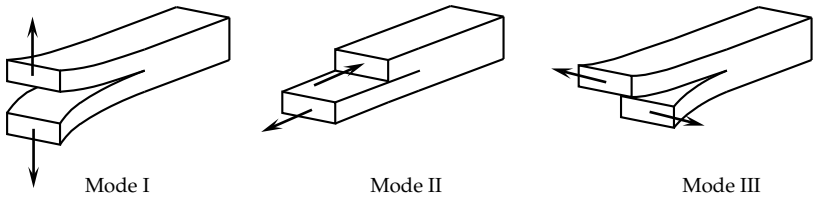

Figure 2.2: Description of the three opening modes of a crack.

where $f^{\mathrm{I}}_{r\theta}(\theta)$ and $f^{\mathrm{II}}_{r\theta}(\theta)$ are functions of the angle θ, K_{I} and K_{II} are the stress intensity factors, which are function of the external loading and the geometry of the body. The stress intensity factor has the following form

$$K = \sigma^{\infty}\sqrt{a}\,Y \ \left[\mathrm{MPa}\sqrt{\mathrm{m}}\right], \tag{2.2}$$

where Y is a dimensionless geometrical parameter and σ^{∞} is the external applied loading.

The stress magnitude computed using Eq. (2.1) is entirely dictated by the magnitude of the K_i factors. Validity of (2.1) requires the existence of a K dominated zone, i.e. the size of the non-linear zone at the crack tip must be much smaller than $a/10$ where a is the crack length. Eq. (2.1) applies in a zone smaller than $a/10$ and larger than the non-linear zone. Two cracked bodies loaded with the same K's are similar in terms of stress at the crack tip even if the external loading configuration or geometry are different.

Under mixed mode loading, the relative amount of mode II to mode I is characterised by the ψ angle defined as

$$\tan\psi = \frac{K_{\mathrm{II}}}{K_{\mathrm{I}}} \ . \tag{2.3}$$

2.1.1 The energy release rate

The energy release rate $\mathcal{G}$ $\left[\mathrm{J/m^2}\right]$ is the energetic driving force to propagate a crack and corresponds to the energy available to increase the crack surface A by one surface unit.

Consider a body with a crack of surface area A (see Fig. 2.3). Forces (F) and displacements (u) are applied to the boundary, involving the storage of internal strain energy W_e. If, due to a change of W_e, noted ΔW_e, the crack surface increases by an amount ΔA, the energy balance writes

$$F\Delta u - \mathcal{G}\Delta A = \Delta W_e \ , \tag{2.4}$$

providing an implicit definition for $\mathcal{G}$. In the absence of crack advance, the difference between the internal energy change and the work done on

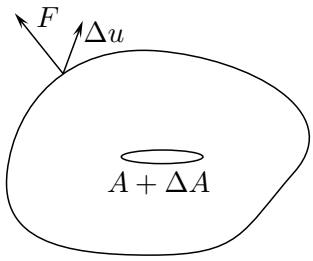

Figure 2.3: Configuration used to define the energy release rate.

the body is the variation of its potential energy (or mechanical energy)

$$\Delta U_M = \Delta W_e - F\Delta u \ . \tag{2.5}$$

Using Eq. (2.4) and (2.5) and taking the limit when ΔA tends to zero, the energy release rate is defined as the change of potential energy of the system due to an infinitesimal change of the crack area:

$$\mathcal{G} = -\frac{\partial U_M}{\partial A} \ . \tag{2.6}$$

In the case of linear elasticity, the stress intensity factors K's and the energy release rate $\mathcal{G}$ are unequivocally related: the energy release rate and the stress intensity factor are two physically equivalent ways to quantify the loading seen by a crack. The relationship between these two values, demonstrated in classical fracture mechanics textbooks [41, 55], is

$$\mathcal{G} = \frac{K_{\mathrm{I}}^2 + K_{\mathrm{II}}^2}{\bar{E}} \tag{2.7}$$

where $\bar{E} = \dfrac{E}{1-\nu^2}$ in plane strain,
$\bar{E} = E$ in plane stress.

2.1.2 Fracture criteria

The first energetic approach of fracture was proposed by Griffith [41]. Griffith modelled cracking as a reversible thermodynamic system. The

total free energy minimisation of the system requires the crack to be in an equilibrium state.

The total energy of the system is noted U. The energy associated with the crack propagation can be partitioned into a mechanical term and a surface term (neglecting other physical and dynamic effects). The mechanical term U_M has two contributions: $U_M = U_E + U_L$. U_E is the strain potential energy stored in the system by stress and U_L is the potential energy of the outer applied loading. The surface term, U_S, is the energy corresponding to the two surfaces created during crack propagation. The total energy writes

$$U = U_M + U_S \ . \tag{2.8}$$

The system is in a thermodynamic equilibrium state while the mechanical and surface contributions balance themselves during a virtual crack advance $\mathrm{d}A$. The trend in the mechanical energy is to decrease during crack propagation $\left(\frac{\partial U_M}{\partial A} < 0\right)$ because the retaining tractions across the incremental crack boundary are relaxed, allowing the propagation of the crack until a new configuration of lower energy is reached. On the other hand, the surface energy term increases with crack extension $\left(\frac{\partial U_S}{\partial A} > 0\right)$ since cohesive forces of molecular attraction must be overcome during the creation of new surfaces. This is the *Griffith energy-balance concept*, of which a formal expression is given by the equilibrium

$$\frac{\partial U}{\partial A} = 0 \ . \tag{2.9}$$

As it is a reversible thermodynamical approach, the crack will extend or heal for small displacements from the equilibrium whether the ratio (2.9) is negative or positive.

The criterion defining whether the crack will propagate is

$$\frac{\partial U}{\partial A} = \frac{\partial U_M}{\partial A} + \frac{\partial U_S}{\partial A} < 0 \ . \tag{2.10}$$

Using the definition of $\mathcal{G}$ (Eq. (2.6)) in Eq. (2.10), the criterion can be recast as

$$\mathcal{G} > \frac{\partial U_S}{\partial A} = \gamma_s \ , \tag{2.11}$$

where γ_s is the surface energy $[\mathrm{J/m^2}]$. The idea can be generalised to any cracking process in which other phenomena than surface creation dissipate energy (friction, plasticity, damage,...). Empirically, a critical energy release rate $\mathcal{G}_c$ can be defined whereby the crack expands as $\mathcal{G} > \mathcal{G}_c$. $\mathcal{G}_c$ quantifies the fracture toughness of the material, i.e. its resistance to crack propagation. As $\mathcal{G}$ and the stress intensity factors are linked, we can also define a fracture criterion in term of a critical K noted K_c. If $K > K_c$, a crack will propagate in the material.

The parameters $\mathcal{G}_c$ and K_c are material properties and represent the toughness of the material. They are intrinsic properties of the material as long as the validity rules for LEFM are met and the mode of loading is kept constant.

2.1.3 Thin film fracture

Fracture mechanics has been widely applied for bulk cracked solids. The application to thin films is more recent, the key reference being [29]. Extra parameters must be taken into account: the influence of the substrate (see Fig. 2.4) and the possible delamination of the film itself.

Consider a freestanding film of thickness t subjected to an uniform tensile stress σ. Assume that the displacement at the load point is fixed, so that the load does no work when crack extends (see Eq. (2.5)). When a crack is introduced, the stress near the crack faces is partially relieved. The zone in which the stress state is affected by the crack extension by the presence of the crack is large (see Fig. 2.4(a)) and the volume of this zone scales as a^2h, see [64]. The energy variation in the film relative to the uncracked geometry is

$$\Delta U_M = -Z\frac{\sigma^2}{2E}a^2t \ , \tag{2.12}$$

where Z is a dimensionless number depending on the elastic constants of the film and of the substrate. The expression of the energy release

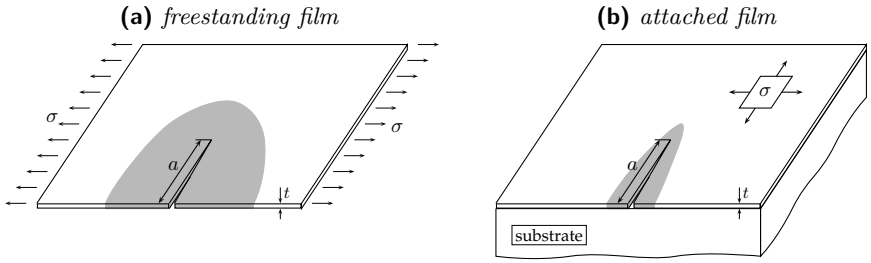

Figure 2.4: Influence zone of a crack (in grey) in a thin film while 2.4(a) the film is freestanding and 2.4(b) the film is lying on a substrate. The films are subjected to an overall stress σ(external or internal). Inspired from [64].

rate is then directly dependent on the crack length

$$\mathcal{G} = -\frac{\partial U_M}{\partial A} = Z\frac{\sigma^2}{E}a \quad \left(\text{or } K = \underbrace{\frac{\sqrt{Z}}{E}}_{Y}\sigma\sqrt{a}\right) . \tag{2.13}$$

For a film lying on a substrate, the constraint induced by the substrate limits the size of the zone affected by the crack (see Fig. 2.4(b)). Its volume scales as ah^2. The introduction of a crack changes the elastic energy by

$$\Delta U_M = -Z'\frac{\sigma^2}{E}at^2 , \tag{2.14}$$

where Z' is a dimensionless number, as Z, but not necessarily equal to Z. The value of Z or Z' must be determined by solving the boundary value problem. The expression of the energy release rate is now independent of the crack length[1]:

$$\mathcal{G} = -\frac{\partial U_M}{\partial A} = Z'\frac{\sigma^2}{E}t . \tag{2.15}$$

The expression of $\mathcal{G}$ is independent of a and crack propagation is a steady-state process. Eq. (2.15) shows that the energy release rate increases with the film thickness. For a coating with internal stress, there is

[1] We consider a crack length such as $a \gg t$.

a critical thickness above which the coating will fracture spontaneously:

$$\mathcal{G} = \mathcal{G}_c \quad \Longleftrightarrow \quad t_c = \mathcal{G}_c \frac{E}{Z'\sigma^2} \ . \tag{2.16}$$

The steady-state character of crack propagation in thin film fracture allows for a simplified mathematical analysis. It is as if the crack tip no longer felt the influence of the other end of the crack. The result is that the energy release rate $\mathcal{G}_{ss}$ can be computed by the difference of the energy of the system far away from the crack tip up and downstream

$$\mathcal{G}_{ss} = -\frac{\partial U_M}{dA} = -\frac{1}{t}\frac{\partial U_M}{\partial a} = -\frac{1}{t}\left(\frac{U_M^{upstream} - U_M^{downstream}}{\Delta a}\right) \ . \tag{2.17}$$

2.2 Application of fracture mechanics to interface cracking

All the concepts introduced previously can be applied to study interface fracture.

In the case of a crack between two different materials, the difference in elastic properties influences the crack behaviour. The elastic mismatch leads to a mixed mode loading even if the macroscopic loading is pure mode I and the geometry is symmetric. The elastic mismatch is fully determined by two parameters, called the Dundurs' parameters [65]:

- The parameter α takes into account the Young's modulus contrast

$$\alpha = \frac{\bar{E}_1 - \bar{E}_2}{\bar{E}_1 + \bar{E}_2} \ . \tag{2.18}$$

- The parameter β somehow takes into account the contrast of the shear modulus

$$\beta = \frac{1}{2}\frac{\mu_1(1-2\nu_2) - \mu_2(1-2\nu_1)}{\mu_1(1-\nu_2) + \mu_2(1-\nu_1)} \ , \tag{2.19}$$

where ν_i are the Poisson coefficients and μ_i are the shear modulus of the materials. The subscripts 1 and 2 refer to the two different materials on both sides of the interface.

In such a case, the relationship between $\mathcal{G}$ and the K's generalises Eq. (2.7) as

$$\mathcal{G} = \frac{1}{2}\left(1-\beta^2\right)\left(\frac{1}{\bar{E}_1}+\frac{1}{\bar{E}_2}\right)\left(K_{\mathrm{I}}^2+K_{\mathrm{II}}^2\right) \ . \tag{2.20}$$

The main additional difficulty while dealing with interfaces is the presence of mode mixity even in the absence of overall mode II loading. It can be seen in Eq. (2.20). The intensity factor for mode II, K_{II}, enters the expression of the energy release rate. Another influence of the mode mixity is that the crack path is determined. In the case of crack propagation in a bulk solid, the crack path is often defined by the most critical direction depending on the external loading. This direction is such that the crack reorient to be loaded essentially under mode I. In the case of interface fracture, the path is determined by the interface. Mode mixity is playing an important role in the analysis of fracture toughness of interfaces.

The propagation criterion for cracking along an interface writes [29]

$$\mathcal{G} \geq \mathcal{G}_c(\psi) \ , \tag{2.21}$$

where $\mathcal{G}_c(\psi)$ is the interface toughness between two layers. It is a function of the mode mixity ψ (see Fig. 2.5). Usually, $\mathcal{G}_c$ increases[2] when mode mixity differs from 0°. This characteristic offers an opportunity to design better interfaces by raising the local mixity at the interface, for instance by acting on the elastic stiffness difference between the two materials [72].

The adherence between two different materials depends thus on the properties of these materials and on the properties of the interface. Different contributions to $\mathcal{G}_c$ can be distinguished as

$$\mathcal{G}_c = \Gamma_0 + \Gamma_p(\Gamma_0, \text{strength of the interface}) \ , \tag{2.22}$$

[2]But not always and the shape is not inevitably symmetric

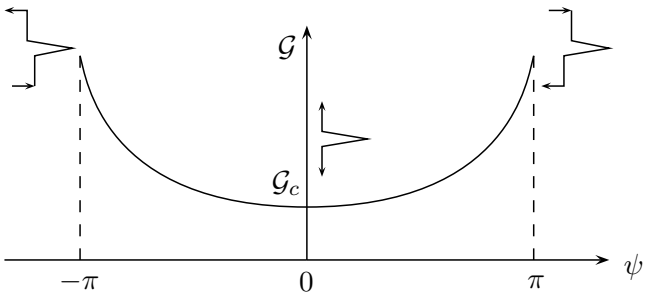

Figure 2.5: Variation of the interface toughness as a function of the mode mixity. This variation depends on the system and the shape is not always symmetric.

where Γ_0 is the work of adhesion (see next section) and Γ_p represents the other dissipations in the material layers surrounding the cracking interface. The magnitude of the dissipation is very much dependent on Γ_0 as well as on the strength of the interface. The mechanical properties of the materials close to the interface influence also the dissipation, i.e. if the yield strength of the material is low, the plastic dissipation will be bigger. The determination of Γ_p by determining its expression is one of the goal of this work in the case of the wedge opening test. The different terms contributing to the total dissipation and their influence will be discussed later in this thesis.

The interface toughness can be evaluated using a large number of methods, from the most simple to the most accurate. In the following chapter, we will focus on several methods based on LEFM, as described in the present section, in order to evaluate the interface toughness $\mathcal{G}_c$. Other methods, more qualitative but more used in the industry, are also described. Comparison between simple and qualitative methods is also performed in the last chapter.

2.3 Physics and chemistry of interface fractures

This section provides a short introduction to the physics and chemistry of the interface energy between a film and a substrate (the interface that

will crack), based on Ref. [20, 61].

The interface energy will heavily depend on the interface structure. The interface structure depends on the mechanisms of growth of the film, which are briefly described in this sub-section.

Mechanisms of film growth

During plasma sputtering deposition, the molecules coming from the target hit the surface of the substrate. While approaching the substrate, the molecule is attracted by the surface. The molecule are attracted due to the presence of fluctuating dipole moments in each atoms. These interactions between the surface and the atoms are of Van der Waals type. If the incident molecule has a permanent dipole, the attraction is stronger. The process in which the incident molecule is trapped on the surface is known as *physical adsorption*. these atoms physically adsorbed on the surface are mobile. These can either desorb by gaining enough energy, or these may undergo a further interaction consisting in the formation of chemical bounds with atoms of the surface. This second step is called *chemisorption*. During this step, the incident atom and substrate atoms rearrange their electrons. The energy of the binding due to chemisorption is greater than in physical adsorption.

The atoms deposited on the substrate, while still mobile, can be arranged in different shape to form the film. Three main modes exists: the Volmer–Weber model, the Frank–Van der Merwe model and the Stranski–Krastanov model.

- In the Volmer–Weber model, the incident atoms will be arranged in distinct nuclei that will grow independently. During deposition, both the number of nuclei and the size of a given nucleus increase until they intergrow with each other to form a continuous film.
- In the Frank–Van der Merwe model, the incident atoms form a succession of monolayers on the substrate. The interaction between the incident atoms and the substrate surface are stronger that between neighboring incident atoms. the film grows then layer-by-layer.

- The Stranski–Krastanov model combines the features of layer-by-layer growth and discrete three-dimensional nucleation. The film begins to grow layer-by-layer and then, nuclei appears on the surface during film growing.

The growth of a film during the deposition depends on the energy of the impacting particles, the Gibbs free energy. Consider the condition of equilibrium when the gas phase is in contact with the deposit. The change in the Gibbs free energy when n_p particles are transferred from the vapour to the deposit is

$$\Delta G = n_p k_B T \ln\left(\frac{p}{p_0}\right) \ , \tag{2.23}$$

where p_0 is the equilibrium vapour pressure. The ratio p/p_0 is called the degree of supersaturation. The conditions for the formation of the growth modes depends on the surface energy when a particle is deposited on a substrate as

$$\begin{cases} \text{layer growth if:} & \gamma_\mathrm{s} \geq \gamma_\mathrm{f} + \gamma_\mathrm{fs} + C k_B T \ln\left(\frac{p}{p_0}\right) \ , \\ \text{island growth if:} & \gamma_\mathrm{s} \leq \gamma_\mathrm{f} + \gamma_\mathrm{fs} + C' k_B T \ln\left(\frac{p}{p_0}\right) \ , \end{cases} \tag{2.24}$$

where C and C' are numerical constants and the different γ_x relates to the free energy density (see further). One observes that the growth mode can be changed by varying the supersaturation conditions. The layer-by-layer growth mode is favoured by a high supersaturation. A more detailed presentation of the thermodynamic analysis of the three modes of growth can be found in [20]. The actual mode of growth depends on the materials involved, the temperature of the substrate and the degree of supersaturation of the vapour.

Like free surfaces, interfaces at which materials joined can also be represented macroscopically as discrete surfaces and can be characterised by an interface surface energy per unit area. The physical origin of this energy is essentially the same as that of as free surface. The energy density of an interface is presumably less than the sum of the free surface energies of the two materials joined at that interface and greater

than the energy densities within either of the materials at interior points remote from the interface.

Suppose that a small island of film material is deposited onto the surface of the substrate. With this deposition, there is a decrease in the area of the substrate free surface, a change in the area of the free surface of the film material and an increase in the area of a shared interface. There is a surface free energy density associated with both the substrate and film materials, say γ_{s} and γ_{f}, respectively. The interface is also characterised by a free energy density, say γ_{fs}. The equilibrium shape of the island is such that the free energy for a given island volume is the lowest. by considering the angle between the substrate surface and the tangent plane to the island surface at the contact line by θ, the equilibrium condition is

$$\gamma_{\mathrm{s}} = \gamma_{\mathrm{fs}} + \gamma_{\mathrm{f}} \cos\theta \ . \tag{2.25}$$

This expression is generally known as Young's equation for the wetting angle of a fluid droplet on a rigid solid surface. The angle θ depends on the ability of for the film material to wet the substrate material surface. More details about the surface energy of solids can be found in [61].

Work of fracture

The Griffith criterion, described in Section 2.1.2, was developed as a basis for considering the onset of crack growth and fracture advance in a homogeneous material by relating the potential energy release rate $\mathcal{G}$ to the microscopic work γ_s required to create the new surfaces.

For the growth of a crack along a bimaterial interface between two materials, the process can be viewed in more or less the same way. The simplest case involves interface separation between two materials (a film and a substrate) joined along an interface, which is analogous to the original situation considered by Griffith. If the separation of the interface occurs by growth of an interface crack without inelastic deformation in either of the materials involved, then the work of fracture is

$$\Gamma_0 = \gamma_{\mathrm{f}} + \gamma_{\mathrm{s}} - \gamma_{\mathrm{fs}} \ . \tag{2.26}$$

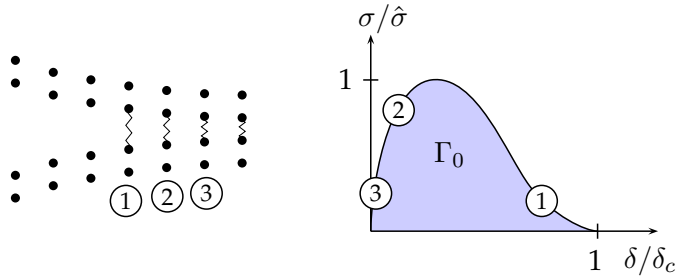

Figure 2.6: Traction separation law of the cohesive zone model.

If the two materials are identical, then $\gamma_{\mathrm{fs}} = 0$ and $\gamma_{\mathrm{f}} = \gamma_{\mathrm{s}}$, so the original picture conceived by Griffith is recovered.

Eq. (2.26) consider the substrate surface to be perfectly flat. But, the surface of a real substrate is never perfectly flat. The roughness of the substrate offers possible mechanical grip to the coating. An additional term taking into account this mechanical grip, say $W_{mech}^{\mathrm{interf}}$, can be added at the right term of Eq. (2.26).

A common representation of the behaviour implied by Eq. (2.26) within a continuum framework is that of separation of adjacent planes of otherwise elastic materials, with that separation being resisted by a cohesive traction acting across the gap between these planes. It is called the *cohesive zone model* of material behaviour. The magnitude of the cohesive traction depends locally on the amount of interface separation δ as shown in Fig. 2.6. The traction represents atomic interaction and its magnitude falls to zero beyond some separation distance δ_c on the order of the atomic spacing in the material involved. In this case, the work of fracture is the work done in overcoming this resisting traction as

$$\Gamma_0 = \int_0^{\delta_c} \sigma(\delta)\, \mathrm{d}\delta \ . \tag{2.27}$$

For this representation, the interface is characterised by the work of fracture Γ_0 and by the maximum value of traction $\hat{\sigma}$. All the different terms of Eq. (2.26) and the different mechanisms of fracture are considered as a black box and only two parameters fully characterize the interface.

The work of fracture essentially depends on the materials on both sides

of the interface and on their mutual affinity (considering perfect materials and interface). The peak stress $\hat{\sigma}$ is directly linked to the physical and chemical properties of the interface. The first point is the type of chemical bonds across the interface. Covalent bonds (e.g. used in wafer bonding) are stronger than Van der Waals interactions. The activation of the substrate surface obtained by the application of a plasma on the surface prior to the coating deposition increases the chemical interactions between the materials on each sides of the interface.

The application of a plasma on the substrate surface leads also to an effective cleaning of the surface. The strength of the interface is highly dependent on the interface contamination. The adhesion of the coating is larger while deposited on a clean surface. Chapter 5 illustrates the fact that a poor cleaning of the interface before deposition of the coating leads to large variation of the adhesion which cannot be predicted. The adhesion of the coating depends on the local poisoning of the interface and, if contaminants species remain on the substrate surface, the adhesion can vary a lot between two points close to each other.

Reaction products and brittle precipitates which might be present along the interface can significantly diminish the resistance to interface fracture. These contaminants have to be removed. Specific deposition processes can be used to allow the gettering or the diffusion of these contaminants out of the interface to produce a stronger interface strength.

Chapter 3

Interface toughness testing

There are many ways to evaluate the adhesion of thin films on a substrate. It is an objective of this thesis to develop testing techniques together with a data reduction scheme, which could provide accurate values of the interface energy release rate. Only a small number of methods allow quantitative analysis. Indeed, most methods give only a qualitative value of the adhesion, a *yes* or *no* information, i.e. the film is still attached to the substrate or not after the test. No other information can be inferred but the implementation of these methods is usually very easy. This kind of methods can be used quickly on the production line. The first section of this chapter presents some of these testing methods. The other sections detail four quantitative tests, from which the energy release rate associated to an interface can be extracted: the wedge opening test; the superlayer test; the four-point bending test and the blister test. Extensions to the first two are discussed in Part II as one of the contribution of the present thesis.

3.1 Qualitative adhesion tests

The first section explains qualitative methods daily used in the industry.

3.1.1 Variations on the tape test

The simplest test to perform is the *tape test*. The principle is to put a piece of tape on the film to test and then peel it off. Two alternatives are possible: either the film remains on the substrate, or is removed and sticks to the tape, see Fig. 3.1(a). If the film does not delaminate, it is considered to have a good adhesion. Some variation are possible and explained hereafter. There is no normalization of the test but normalized tape are used (see [30, 37]).

(a) *Tape test applied on a copper film.* **(b)** *Cross-cut test.*

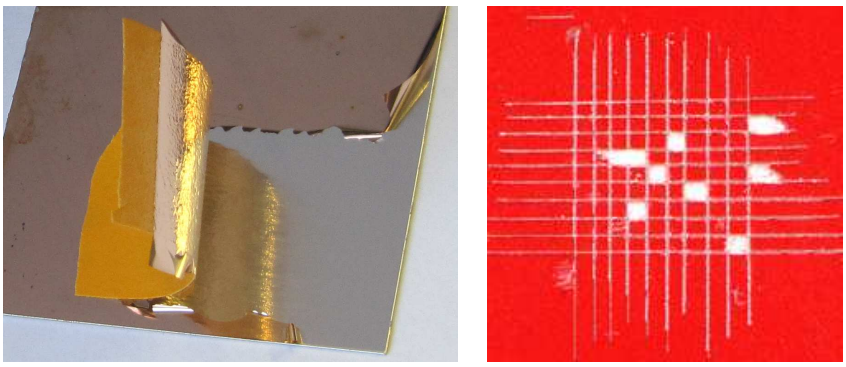

Figure 3.1: Tape test and cross-cut test applied to thin films.

The *cross-cut* is a more severe test. The surface of the specimen is cut cross-wise after coating. An adhesive tape is applied on the surface and then peeled off, see Fig. 3.1(b). Due to the high number of free edges in the film, the initiation of the delamination is made easier. The test is normalised and the way the scratches are made is strictly described (see [30]). The result of the test is a number which goes from 0 if no coating has been removed to 5 if more than 65% of the coating has been removed from the substrate. In practice, the important thing is that the scratches are parallel and approximately the same. It is easier to make the scratches with a regular rule and the result is relevant enough.

Another harsher test is the *T-bend* test. Prior to the application of the tape, the substrate is bent until the back of the substrate is touching itself (see Fig. 3.2). This is the starting point of the test. The film is

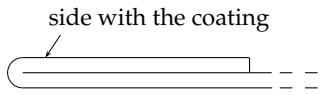

Figure 3.2: Starting point of the T-bend test.

then highly deformed before being peeled off using a piece of tape. If the coating resists to the delamination, the adhesion is sufficient and the film is said to be 0T. If the coating delaminates, the substrate is again bended until touching again itself, as shown in figure 3.3. If the coating stays on the substrate after the peeling, it is said 0T5. If it delaminates again, the procedure is repeated until the absence of delamination of the coating. The result of the test is noted, according to the ECCA T7 quotation, as *(internal radius of the plate / substrate thickness) T*.

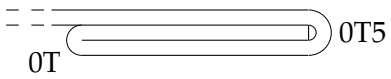

Figure 3.3: Schematic view of the T-bend test.

Other ways to bend the substrate may be used. The substrate can be either cup drawn or bent at a fixed curvature radius. Afterwards, the tape test is applied to verify the coating's adhesion after the forming procedure.

3.1.2 Semi quantitative tests

Two other tests widely used in the industry give a numerical value used to characterise the adhesion of the interface. The first is the *scratch test* and the second is a *tensile or pull test*.

The principle of the *scratch test* is to use an indenter to scratch the surface of the coating (see [11, 62]). The load imposed to the indenter increases linearly while the indenter moves until the tip reaches the substrate surface. The tip of the indenter then delaminates the coating. The value of the load while the tip touches the substrate is used to characterise the coating's adhesion.

The second is a *tensile or pull test* (see [31, 37]). A circular pad is bonded to the coating and the system is put in the grip of a universal tensile machine. The substrate and the pad are pulled off and the load needed to delaminate the coating (if it delaminates entirely) is recorded to characterise the adhesion.

3.2 Wedge opening test

The principle of the wedge opening test is to propagate a crack along the interface by insertion of a wedge within a cantilever, see Fig. 3.4 or [37].

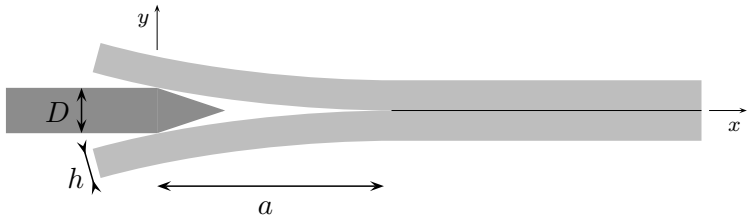

Figure 3.4: Description of the wedge opening test geometry. The different geometric parameters required to compute the interface toughness are shown.

The dimensions of the wedge and of the test specimens are known. In most cases, the equation used to compute the interface toughness is deduced from the linear elastic beam bending theory [41], as

$$\mathcal{G} = \frac{3\bar{E}h^3D^2}{16a^4} \ , \tag{3.1}$$

where $\bar{E} = E/(1-\nu^2)$ is the plane strain modulus. The other variables are defined in Fig. 3.4: D is the wedge thickness, h is the arm thickness[1] and a is the crack length. Eq. (3.1) assumes that the two beams have the same thickness h and that the specimen is deforming in the elastic regime. If the sample is not bonded over its entire width, a correction multiplicative term taking into account the ratio between the width

[1]The notation h will be use in this manuscript to design the substrate thickness. The coating thickness will be named t with usually $t \ll h$

of the sample and the width of the bonded region has to be added. For asymmetric specimens or specimens involving different materials, a small correction is necessary [41], consisting in the substitution of $\frac{1}{Eh^3}$ by $\frac{1}{2}\left(\frac{1}{E_1 h_1^3} + \frac{1}{E_2 h_2^3}\right)$ in Eq. (3.1).

3.2.1 Interface toughness measurement between transparent substrates

Some experiments using the wedge opening test have been made on transparent substrates. Microelectronic industries are using silicon as substrate, which is transparent to infra red radiations. Experiments measuring the interface toughness of wafer bonding involving the wedge opening test are reported in [7, 70]. The crack length is measured on a picture of the specimen taken during the test, see Fig. 3.5.

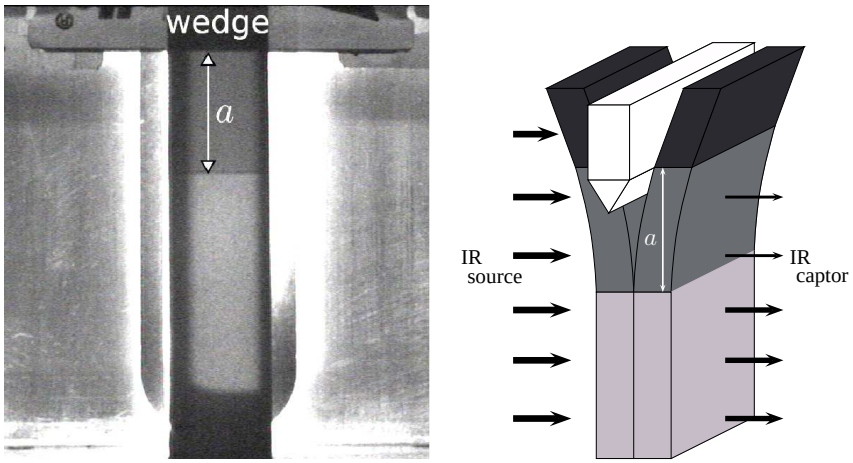

Figure 3.5: Top view of a silicon specimen illuminated by an infra red source. The air between the arms of the specimen at the crack changes the way the light passes through the specimen. The crack is then darker than the rest of the specimen.

A correction term takes into account the systematic underestimation of the crack length due to the light wavelength, because an air gap smaller than a quarter of the wavelength can not be detected. The interface toughness is then computed using Eq. (3.1).

Another use of the wedge opening test is made for measuring the interface toughness of thin films deposited on glass [5]. The crack length is measured with a transparent ruler to be used in the interface toughness equation.

In these papers, the interface toughness varies between 0.3 and 2.5 J/m^2. For such substrates (silicon or glass), plastic deformation is not possible. If the substrate is too thin or the interface toughness too high, there is a risk for the crack to propagate through the substrate and ruin the specimen.

3.2.2 Interface toughness measurement between non transparent substrates

The wedge opening test has also been used to measure the interface toughness between non transparent substrates. For such cases, the crack length cannot be directly measured. Other parameters have to be used to allow the computation of the crack length.

Sener et al. [59] have proposed to measure the interface toughness of steel or aluminium plates bonded together with an adhesive layer using the wedge opening test with the crack length measured optically on the side of the specimen. This is made possible thanks to the relatively large thickness of the wedge (1.5 mm). A complementary measurement of the displacement along the specimen arm was made using displacement sensors (see Fig. 3.6). The displacement was measured at one point during the wedge advance. An average deflection was then computed using the displacement of both sides. This deflection was compared to the analytical expression of the beam bending theory, considering different crack lengths in order to fit the experimental data.

Phillips et al. [57] have used the wedge opening test to measure the toughness of brazed joints. The measured interface toughness is in the order of 1 kJ/m^2. It shows that the wedge opening test can be used for evaluating a wide range of interface toughness. The toughness was also measured using the opening displacement of the sample. The displacement sensor was located close to the contact point of the wedge.

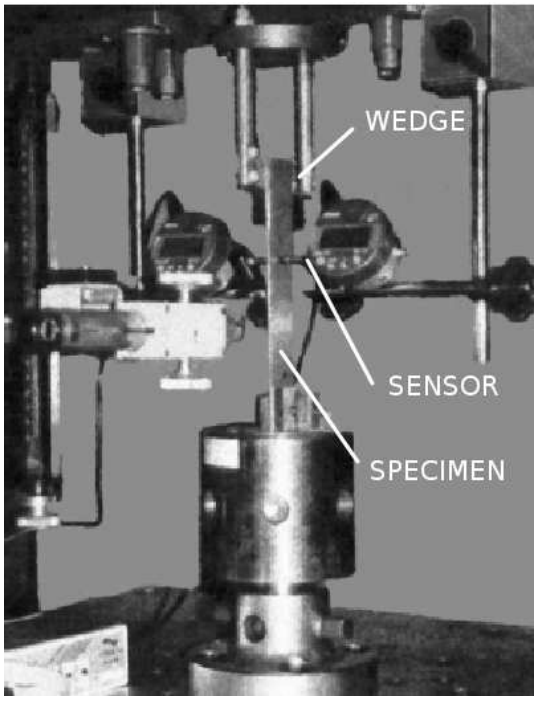

Figure 3.6: Photograph of the testing setup taken from [59]: wedge opening test for non transparent substrates.

Plastic deformation can occur while using ductile substrates. Thouless et al. [66] consider a specimen loaded with a constant bending moment M_0 imposed by the wedge. The wedge is inserted in the specimen quickly using a hammer and the residual radius of curvature of the substrate is measured. This radius is constant in the region where the adhesive is applied, validating the hypothesis that the fracture occurs under a constant moment.

Another variation of the crack length measurement for the wedge opening test has been studied during this thesis. The development of the method is explained in Part II of this thesis.

3.3 Superlayer test

The superlayer technique has been developed to measure the interface toughness based directly on microelectronics fabrication techniques without additional external loading device. First, the principle of the method is explained. Then, some extensions of the method are described.

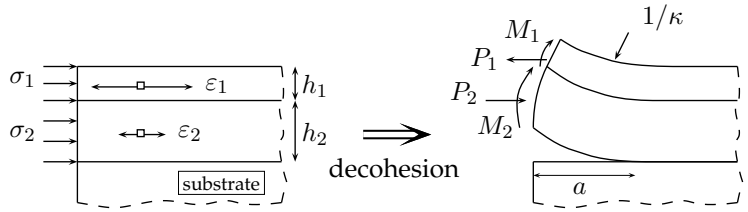

Figure 3.7: Schematic drawing showing the behaviour of a bilayer film subjected to residual tension as it delaminates from the substrate after the crack initiation. The residual stresses σ_l in each layer ($l = 1$ or 2) provides the forces P_l and the moments M_l in the free part of the bilayer, inspired by [4].

3.3.1 Basic procedure

The superlayer adhesion testing method was first proposed by Bagchi et al. [4]. The principle relies on the use of the internal stress present in the film of interest to delaminate the tested coating (see Fig. 3.7). In case the stress in the film is too low to lead to spontaneous delamination, a layer with high internal stress is deposited on top of the system, hence the name 'superlayer', in order to increase the elastic energy available to promote the delamination and meet the condition

$$\mathcal{G} \geqslant \mathcal{G}_c \ . \tag{3.2}$$

The stress gradient in the bilayer coating leads to bending after decohesion. The energy release rate during decohesion writes

$$\mathcal{G} = \sum_l \frac{\sigma_l^2 h_l}{\bar{E}_l} - \sum_l \frac{1}{\bar{E}_l} \left[\frac{P^2}{h_l} + \frac{12 M_l^2}{h_l^3} \right] \ , \tag{3.3}$$

where $l = 1, 2$ refers to the two materials of the bilayer.
The load P associated to the residual stress can be expressed in terms of the coating curvature κ and the properties of the layers as

$$P = \left[\frac{\bar{E}_1 h_1^3 + \bar{E}_2 h_2^3}{6\,(h_1 + h_2)} \right] \kappa \ , \tag{3.4}$$

with the curvature given by

$$\kappa = \frac{6\,(h_1 + h_2)\,(\varepsilon_1 - \varepsilon_2)}{\left[h_1^2 + \dfrac{\bar{E}_2 h_2^3}{\bar{E}_1 h_1} + \dfrac{\bar{E}_1 h_1^3}{\bar{E}_2 h_2} + h_2^2 + 3\,(h_1 + h_2)^2 \right]} \ , \tag{3.5}$$

where $\varepsilon_l = \sigma_l / \bar{E}_l$.
The bending moment per unit width is given by

$$M_l = \bar{E}_l \kappa I_l \ , \tag{3.6}$$

where $I_l = h_l^3/12$ is the second moment of area.

If not sufficient, the energy required to reach the critical decohesion value can be attained by an increase of the superlayer thickness, see Eq. (2.15).

The energy needed to initiate the crack is higher than the energy needed for propagation. To make cracking initiation easier, a non-adherent layer is added on top of the substrate before the coating (Fig. 3.8(a)). The coating and the superlayer are then deposited and patterned into strips (Fig. 3.8(b)). The initiation of the crack is achieved by cutting through the coating down to the interface (Fig. 3.8(c)), see [4].

The main disadvantage of this method is that a large number of specimens with varying superlayer thicknesses are required to bound $\mathcal{G}_c$ tightly.

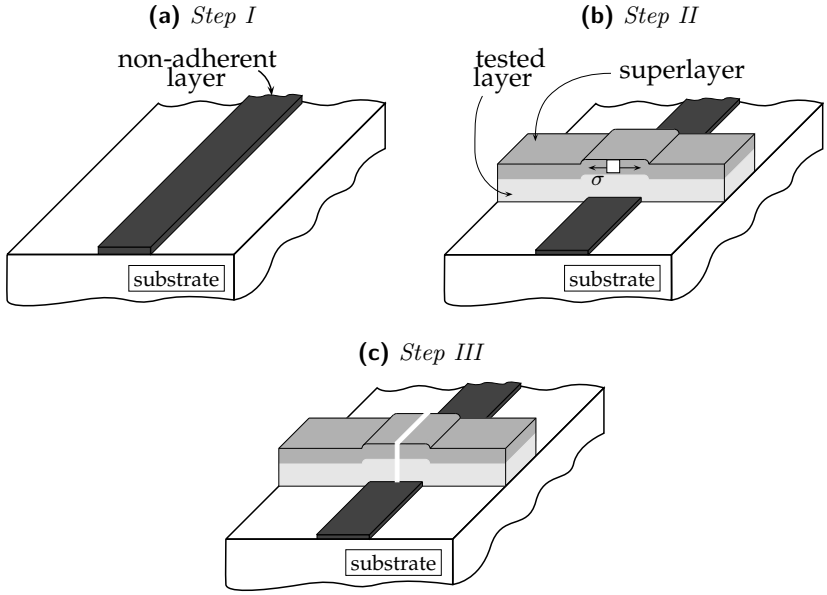

Figure 3.8: Fabrication steps required to prepare specimens for measuring the adhesion energy using the superlayer method, directly inspired by [4].

3.3.2 Modified versions of the superlayer test

Several variants of the superlayer test have been proposed to make it more direct to use.

General idea

In the absence of external loading, the energy release rate is the change of mechanical energy per crack surface unit

$$\mathcal{G} = -\frac{\partial U_M}{\partial A} \ . \tag{3.7}$$

A modification in the energy or in the crack surface will change the energy release rate. In the superlayer test, the energy release rate is modified by varying the stress in the layer (which changes U_M) while keeping the crack surface constant. The modified tests propose to impose variations of $\mathcal{G}$ by changing the width of the delaminating zone while keeping the mechanical energy constant. This enhancement is obtained by patterning the non-adherent layer between the substrate and the coating.

Modified delamination test

The first modification proposed in ref. [46] consists in adding a non-adherent strip (thinner than the coating strip) below the coating as shown in Fig. 3.9. Hence, the interface area between the substrate and the coating is reduced. The factor ζ represents the ratio between the non-adherent layer width w_n and the coating layer width w_i as

$$\zeta = \frac{w_n}{w_i} \ . \tag{3.8}$$

After initiation, the crack will propagate or not, depending on the width of the interface between the substrate and the coating. The smaller the width, the lower the energy needed to delaminate the coating. The relationship between the energy release rate and the energy needed to delaminate a strip depends on ζ as

$$\mathcal{G}_c = \mathcal{G}\,(1-\zeta)^{-1} \quad \text{for } 0 \leqslant \zeta < 1 \ , \tag{3.9}$$

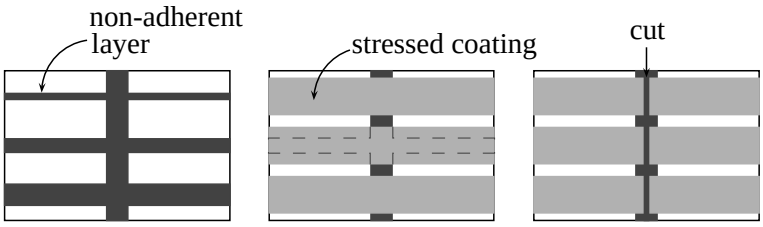

Figure 3.9: Deposition steps used in the modified superlayer test, inspired by [46]. The first step is the only one different from the basic test (see Fig. 3.8).

where $\mathcal{G}$ is the energy release rate of the interface, without considering non-adherent layer. For high values of ζ, edge effects occurring along the edges of the non-adherent layer are significant [46].

Fixtureless delamination test

Another variation, regarding the non-adherent layer design consists in producing a triangular-shaped pattern (see Fig. 3.10) as described in ref. [80]. This configuration offers the advantage of providing with only one strip the exact value of the interface toughness. The variation of the

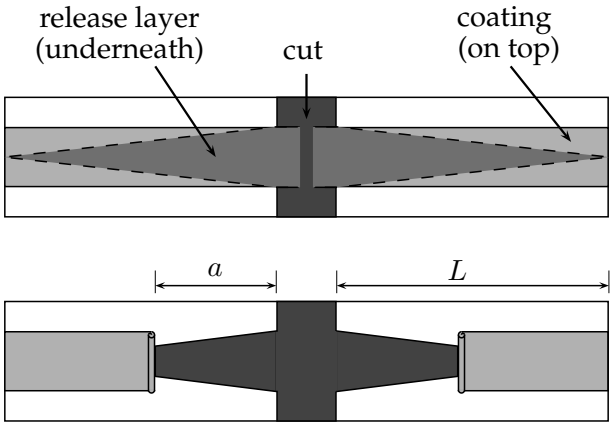

Figure 3.10: Schematic drawing of the delaminated coating strip using a triangular non-adherent layer for the superlayer test (inspired by [80]).

interface width between the substrate and the coating is continuous.

Knowing the crack length, the interface toughness is computed using

$$\mathcal{G}_c = \mathcal{G}\frac{L}{a} \ , \tag{3.10}$$

where $\mathcal{G}$ is the steady state energy release rate given by Eq. (3.3), the other parameters being defined in Fig. 3.10.

3.3.3 Extension of the superlayer test method at UCL

The superlayer method has been recently extended at UCL[2]. The test configuration as well as preliminary assessments are presented in this section.

The development of micro-lab on chip for nanomechanical testing has been done for a few years at UCL [21, 38]. These devices are used to measure the mechanical properties of thin films. The idea is here to extend these "lab on chip" to the measurement of the interface toughness using the superlayer method. The advantages of the superlayer method is that no external tool is required. The measurement is made only using thin film deposition techniques similar to those used for the lab on chip. The quantitative measurement of the interface toughness can be made based on a yes/no information.

The objectives of the master thesis were to (i) reproduce the methods described in the literature and test new extensions in order to make the method more accurate and (ii) assess the Al/SiO_2 interface toughness.

This section first describes the preparation of the specimens and the general steps of thin film processing. Description of the fabrication process used for adhesion testing and preliminary assessment of Al/SiO_2 interface are made at the end of this section.

[2]These developments were made in the course of the master thesis of Pierre Steffen and Nicolas Gosset, for which I was involved in the supervision.

Test sample preparation

The main point of the method is that the delamination is promoted by the presence of the *superlayer*, involving a large internal stress. The different deposition steps required to obtain a superlayer test as developed at UCL are the following:

- deposition and patterning of the non-adherent layer;
- deposition of the layer to be tested;
- deposition of the superlayer;
- patterning of these last two layers with different patterns;
- initiation of the crack.

A short explanation of the microfabrication methods is given in the following paragraphs for readers not used to these techniques. A full description of the methods can be found in [20, 52].

Photolithography plays an important role in microfabrication. It involves the different steps described in Fig. 3.11 with many possible variations.

1. First, a photoresist layer is deposited on top of the layer to be patterned. The resist can be either positive or negative. This means that the pattern of the resist can be exactly the same as on the mask (positive photoresist) or can be the opposite of the pattern on the mask (negative photoresist).
2. The mask is set up over the specimen. The alignement is obtained using marks previously etched on the specimen.
3. The photoresist is then illuminated by UV light. The regions protected by the mask are not affected by the light. The result is different depending on the photoresist used:
    - for the *positive* photoresist, the structure of the photoresist is altered to make it soluble;

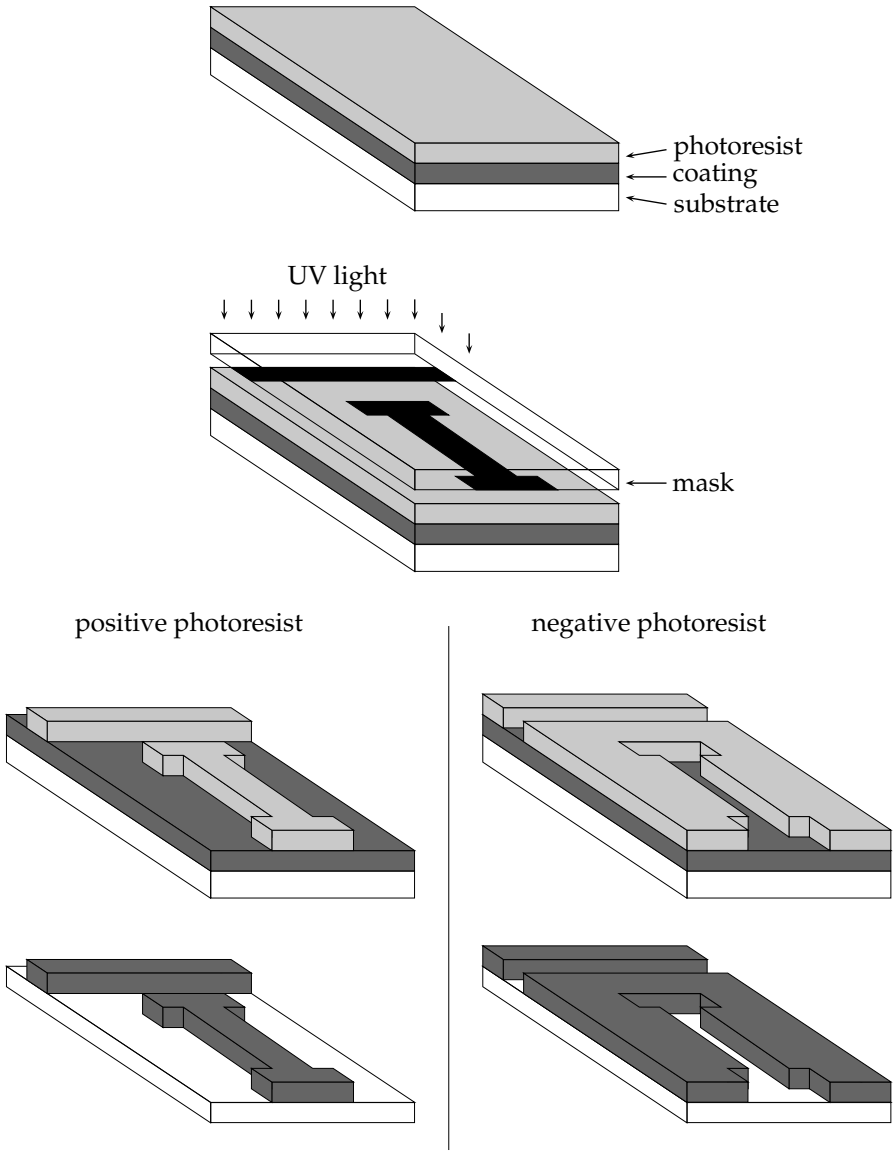

Figure 3.11: Schematic of the photolithographic process for pattern transfer from mask to film. Both negative and positive resist behaviours are illustrated.

- for the *negative* photoresist, the UV light catalyses long polymeric chains that become indissoluble.

The specimen is then put in a chemical solution to remove the soluble photoresist. The photoresist is then patterned (see the third step in Fig. 3.11).

4. The coating is etched using either a chemical solution or by plasma. After the removal of the photoresist (usually with acetone), the coating is patterned as shown in the last step of Fig. 3.11.

In a similar way, the resist can be used as a "mask" deposited on the substrate before the coating deposition. The coating is deposited on the substrate where the resist has been dissolved and on the resist where it stays. After the deposition, all the resist is dissolved and the coating is also removed. This technique, called *lift-off*, is often used when the coating is resistant to the usual etching.

Description of the design and fabrication process for on-chip adhesion testing

The fabrication process used to build the test structure involves different steps and requires a specific mask. This section describes in details the design of the structures as drawn on the masks and the different generic processing steps.

Mask used during this study

The process leading to the test structures requires four photolithography steps. A mask has been designed such that each quarter of it is devoted to one photolithography step.

1. The first quarter is devoted to the definition of the alignment marks. These marks are used to align the different parts of the mask at the correct position.

2. The second quarter defines the pattern of the non-adherent layer. Four different designs have been used. They will be described later in this section.

3. The third quarter defines the pattern of the coating and the superlayer. As the superlayer is deposited on the coating, it involves the same patterns.

4. The last quarter is used to define the zones where the crack will be initiated through a cut.

Each quarter of the mask is also divided into squares of 11×11 mm. This is necessary because some steps require the specimen maximum size to be 10 mm. There are five different zones, designated zone 1 to zone 5. Some of these zones are reproduced more than once over each quarter of the mask. The zones 1 to 3 involve different patterns of the non-adherent layer. Zone 4 is used for other processes requiring also four photolithography steps and zone 5 is the same as the zone 1 except for the coating pattern (it is designed to avoid the last step of the process, which consists in the crack initiation). Over one zone, the shape of the pattern is reproduced with different sizes. Here is the description of each zone.

Zone 1: The non-adherent layer is patterned into rectangular strips, see Fig. 3.12(a). Each strip is centered under a corresponding strip of the coating. The width of the strips is varying slowly from one to another. This design is the same as in ref [46]. This is the reference configuration, which will be used for comparison with the literature.

Zone 2: The non-adherent layer is patterned into several rectangular strips: two or three under each coating strip (see Fig. 3.12(b) for an example with two strips). The size of the structure and the total area of non-adherent material under each coating strip is the same as those of zone 1. The goal of this zone is to study the influence of the edge effect singularities on the measurement, see [46].

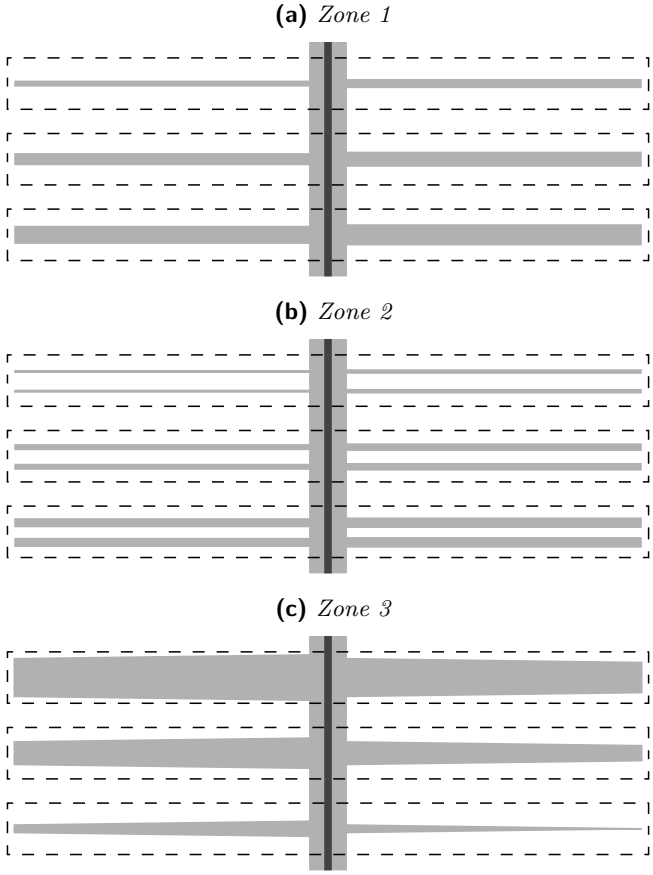

Figure 3.12: Schematic upper view of the different structures designed in the different zones on the mask. The light grey represents the non-adherent layer, the dashed lines represent the outline of the coating and superlayer strips and the dark grey line represents the zone of the cut made to initiate the crack.

Zone 3: The non-adherent layer is patterned with a trapezoidal shape. The objective is to reproduce the "fixtureless delamination test" described in ref. [80]. Instead of patterning the non-adherent layer into a triangle under each coating strip, the triangle has been divided into several parts. Figure 3.12(c) shows a schematic of this kind of structure. The base of the triangle is the top left structure and the bottom right

is the top of the triangle. The intermediate structures involve the intermediate parts designed such that all the structures put together made the entire triangle.

Zone 5: The pattern of the non-adherent layer of this zone is the same as for zone 1. The difference lies in the design of the coating and of the superlayer strips. In the previous zones, the coating strips of two facing structures are connected and an additional step is required to cut the strip and initiate the cracking. The coating strips of zone 5 are directly independent (see Fig. 3.13). The goal is to reduce the number of processing steps. Concerning the tests made up to now at the UCL, this zone is the only one which has delivered valuable results.

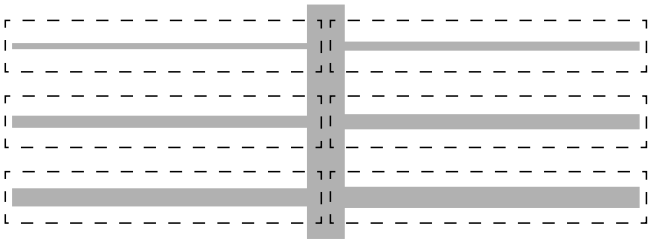

Figure 3.13: Schematic of the structure designed in zone 5 on the mask. The light grey represents the non-adherent layer, the dashed lines represent the outline of the coating and superlayer strips.

Non-adherent layer

The non-adherent layer can be made of several materials. Carbon is known to have a poor adhesion with a large amount of materials but can involve different kinds of reactions (especially with titanium, see ref. [46]). Gold has a poor adhesion on silicon and does not react with most materials. It is one of the materials which have been used in this work. The other material used in this study is silane. Silane has a good adhesion with silicon while allowing the growth on top of it hydrocarbon compounds which will prevent adhesion of the material deposited on top of the layer, see [9].

Gold non-adherent layer

A thin gold layer of 5 nm was deposited over the entire specimen by evaporation. The patterning of the gold layer was performed using the *lift-off* technique. The reason is that gold is a contaminant for microelectronic components. Gold can thus not be etched like many other metals in the UCL cleanrooms.

Due to the low adherence between gold and silicon (needed for the method), the gold layers are easily destroyed during the deposition of the photoresist during the following steps of the process. Special attention has to be paid during the processing while using a gold non-adherent layer.

Silane non-adherent layer

The silane layer has also been structured using the *lift-off* method. The silane is deposited over the wafer patterned with a photoresist. There are two ways to silanise the substrate: through a liquid process or through a gas process. The liquid process consists in immersing the substrate in a chemical solution of silane and a toluene solvent. This process has not been used during this work because the photoresist reacts with the solvent.

The silane is thus deposited using the gas process. The sample is inserted in a quartz reactor tube. Drying is performed at a temperature of 80 °C requiring several cycles of vacuum and then pressurization with argon to avoid any contamination with humidity. The silane condenses on the substrate, creating covalent links with it. A chain molecule then grows over a few nanometre in thickness from the silane. It forms a monomolecular layer on the substrate. The reactor tube has a diameter such that the specimens can have a maximum size equal to 1 cm. The distance between the alignment marks is small so the alignment of the mask is not precise enough. A small difference between the alignment of the different masks can appear and decrease the precision of the measurement (see further in this chapter).

After deposition, the layer is not visible because of the low thickness corresponding to about a chain of 12 carbon atoms. To check the region where the silane has been deposited, we put a drop of acetone on the sample and it gathers where silane is present on the surface (see Fig. 3.14).

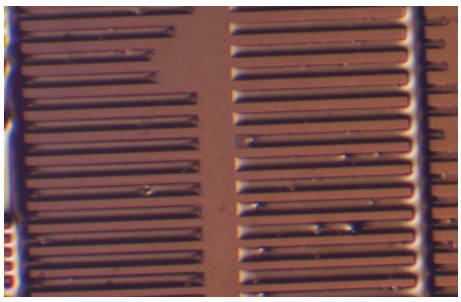

Figure 3.14: Optical micrograph of the silane layer with acetone gathered on it.

Deposition of the test layer and superlayer

The two layers (tested layer and superlayer) are deposited by evaporation. This technique provides very pure thin film materials, good control of the thickness and the homogeneity of the coating.

The measurement of the internal stress of each layer is of prime importance to be able to determine the value of $\mathcal{G}$ using Eq. (3.3). The measurement is made using the Stoney equation (see (6.10) on page 107) after both depositions of the tested layer and of the superlayer.

Crack initiation

The etching of a thin strip to initiate the crack (dark grey strips in Fig. 3.12) is not a trivial task. The notch is very narrow so that small hydrogen bubbles are not drained off easily, reducing the etching rate. Another difficulty is that the resist deposition is made by spin-coating and the centrifugal forces break the coating structures. It is an important point to check for further studies.

Preliminary assessment on Al/SiO_2 interface

The first tests have been performed to measure the adhesion of an aluminium coating deposited on a silicon substrate. The different parts of the specimen are the following:

SiO_2: a small layer of silicon dioxide is present on the surface of the silicon wafer. It is on this oxide that all the other layers are deposited;

Au: the non-adherent layer is made with gold. The layer is deposited by evaporation with a thickness of 5 nm;

Al: the coating studied is made with aluminium. The layer is deposited by evaporation with a thickness of 500 nm;

Cr: the superlayer is made with chromium because it can present a large amount of internal stress. This layer is deposited by evaporation at 15 Å/s. The thickness of the layer is 200 nm with an internal stress value of 793 MPa.

The stress in the chromium layer leads to an available energy equal to $3\,J/m^2$. This is the value of the energy release rate, $\mathcal{G}$, used in Equations (3.9) and (3.10) on pages 33–35.

Adhesion measurement results were only obtained from zone 5 of the mask. All the other zones involved fabrication problems at the last step. The deposition of the resist by spin-coating has destroyed all the existing structures. The structures of zone 5 were analysed before this last step. The result of one series of structures is shown in Fig. 3.15. The delamination occurs between the strips 10 (some amount of delamination but not of the entire strip) and 13 (first entire delamination of a strip). This leads to an interface toughness value between 1.33 and $1.67\,J/m^2$ for the interface toughness of aluminium on silicon oxide.

Figure 3.15 shows that the left part of the strips delaminates more easily than the right part. This is due to the deposition process and the difficulty to align the mask with a high precision. The patterning of the non-adherent layer and the patterning of the coating are not made exactly using the same origin. The non adherent layer strips are not exactly centered below the coating strips. As a result, the contact surface

between the coating and the substrate is not the same on both sides of the strip. The surface is smaller on the left side. This is why this side delaminates first.

Measurements using the wedge opening test have also been performed. The entire procedure used to perform the test is explained in details in Chapter 4. A silicon wafer identical to the substrate is bonded on top of the tested film with cyanoacrylate adhesive and the wedge is inserted between these two wafers to measure the interface toughness.

The energy release rate measured is $4.7\,\mathrm{J/m^2}$. As said earlier, it is not the value of the interface toughness because some extrinsic dissipation in the adhesive layer is taken into account for this value. Quantify the dissipation taking place in the adhesive layer present in the specimen used for the wedge opening test is by no means a simple matters. This will be one of the key problem addressed in Chapter 6. The estimation of the plastic work spent in the adhesive was made using FE simulation

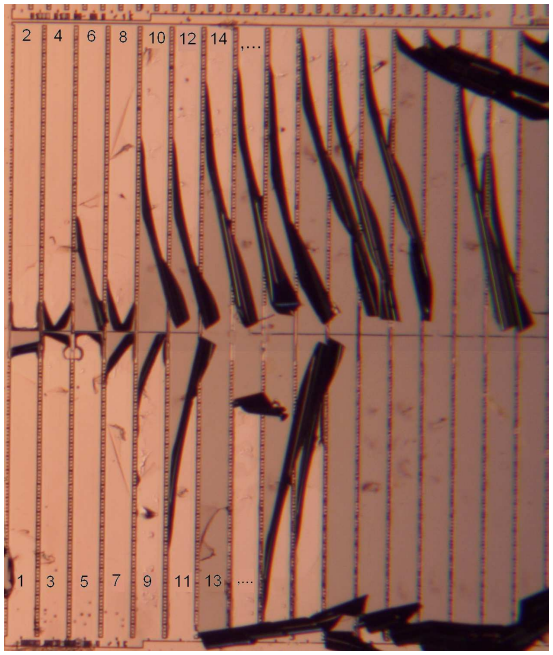

Figure 3.15: Optical micrograph of a test structure after decohesion.

according to the same procedure as in Chapter 6. Assuming a peak stress equal to 1 GPa and a value of $0.8\,J/m^2$ for Γ_0 (see Chapter 6), a value of $0.4\,J/m^2$ has been evaluated for the extrinsic dissipation in the adhesive layer. Furthermore, time plays a role in the test in the first three hours after the wedge insertion (see Section 5.2.2). The measurement we are talking about has been made only a few minutes after the wedge insertion, leading to another uncertainty on the measured value that can be evaluated to $1.3\,J/m^2$, in regards to other measurements made at different places on the same specimen. Taking into account these contributions, the expected value of the interface toughness obtained using the wedge opening test is $3\,J/m^2$.

The uncertainty on the plastic dissipation in the adhesive layer might explain part of the difference between the value measured using the superlayer test and the wedge opening test. Moreover, as said earlier, the non-adherent layer and the coating layer were not aligned exactly the same for the superlayer test. This can make the delamination easier and then lowers the apparent interface toughness. The comparison with the wedge opening test has also to be made more rigorously. Note finally that the application of the wedge opening test on silicon wafer brought an additional difficulty as the substrate is brittle. This is an advantage in terms of result analysis —there is no plastic dissipation in the substrate— but in the case of a high interface toughness, the substrate deforms a lot. This is why a large amount of specimens have failed before the initiation of the crack. Moreover, the cyanoacrilate adhesive is not adapted to bond silicon.

Taking into account these remarks, these first results are encouraging and the ways to solve some processing issues are under investigation.

3.4 Blister test

The bulge test and blister test are two closely related techniques for measuring the mechanical properties and adhesion of films. The principle is to inflate the film through a hole made in the substrate. This is made with a fluid, which imposes a pressure under the film, see Fig. 3.16.

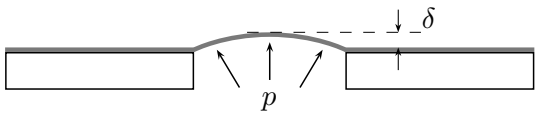

Figure 3.16: Description of the blister test principle.

3.4.1 General description

The bulge test terminology is used when the goal of the test is to deform the film to evaluate the mechanical properties. The purpose of the blister test is to delaminate the film in order to measure the interface toughness [3, 22, 60]. The interface toughness can be determined from the measurement of the blister height δ, the hole diameter and the pressure p.

The blister test can be performed now using two different configurations. In the normal configuration, the hole is made in the substrate and the fluid directly pressurises the coating. In the second configuration (called inverted configuration), the hole is made in the coating and the fluid pressurises the substrate. In this configuration, the substrate can not be thicker than 100 µm (for the device used in this work). There is no rule to choose one configuration or the other preferentially. If one of the layers of the specimen is brittle, the pressure will be applied on the ductile layer. In the case of very thin coating, the inverted configuration is preferred. Another point influencing the choice of the configuration is the ability to make a hole in the substrate. The hole has to stop exactly at the interface of interest. It is not always possible to achieve this. The description of the test made in this section is general and applies to both configurations. The part on which the fluid applies the pressure, i.e. the coating in the normal configuration and the substrate in the inverted configuration, will be called *membrane*.

The blister test involves two steps: the bulging and the crack propagation. Figure 3.17 shows graphically the general shape of the relationship between the pressure and the deflection at the centre of the membrane during both the bulging and the propagation of the crack.

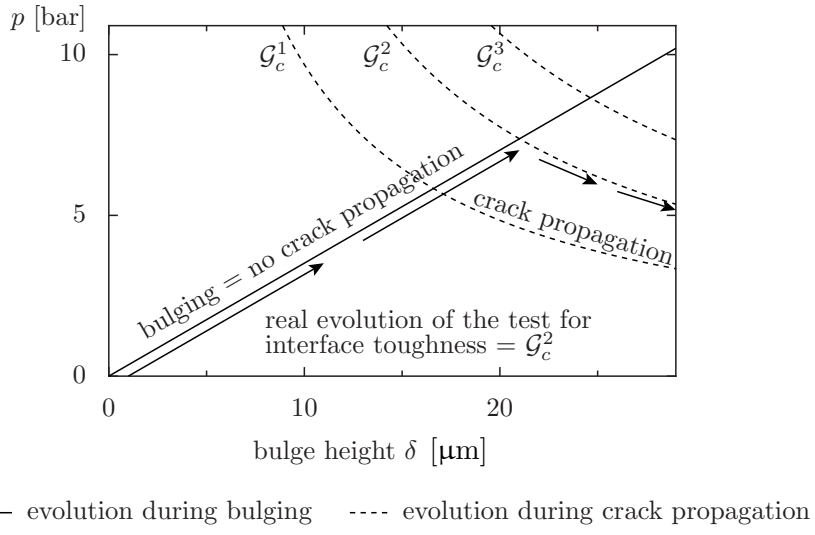

Figure 3.17: General shape of the evolution of the pressure in regards with the membrane centre point deflection during a blister test.

The bulging step is the first (continuous line in Fig. 3.17). The pressure rises and the membrane is deforming like a bulge with a constant diameter. The pressure is too low to induce debonding and the membrane simply stretches and deflects upwards according to the bulge equation

$$p(\delta) = C_1 \frac{\sigma_i t \delta}{a^2} + C_2 \frac{E t \delta^3}{(1-\nu) a^4} + C_3 \frac{E t^3 \delta}{(1-\nu^2)\, a^4} \ , \tag{3.11}$$

where a is the bulge radius, t is the membrane thickness, E and ν are the Young's modulus and Poisson ratio of the membrane, respectively, and σ_i is the residual stress. The three constants C_1, C_2 and C_3 are non-dimensional parameters depending on the membrane geometry. Several expressions for these constants have been proposed in the literature. The expressions of Pan et al. [54] for a circular membrane are

$$C_1 = 4 \tag{3.12a}$$

$$C_2 = \frac{2.667}{(1-\nu)(1.026 + 0.233\nu)} \tag{3.12b}$$

$$C_3 = \frac{14.4}{1-\nu} \ . \tag{3.12c}$$

The first term on the right side of Eq. 3.11 takes into account the contribution of the internal stress of the membrane. The second term represents the resistance to the tension imposed to the membrane. This term is dominant for a thin film membrane compared to the third term which represents the resistance to bending.

This first step of film bulging is often used alone to determine the mechanical properties as explained in ref. [50, 71, 75].

The delamination step follows the bulging (dashed line in Fig. 3.17). While the pressure reaches a critical value, the membrane begins to delaminate. Ideally, a circular crack propagates from the initial hole. During this second step, the pressure lowers and the height of the bulge raises as the crack propagates. According to Hohlfelder's PhD thesis [24] and [47], the expression describing this step is

$$\mathcal{G} = Cp\delta \ , \tag{3.13}$$

where $\mathcal{G}$ is the energy release rate of the interface, p and δ have been defined previously. The dimensionless parameter C is given by

$$C = \frac{1.62}{\pi}\left(\frac{4+5\psi}{4+4\psi}\right) \ , \tag{3.14}$$

with

$$\psi = \frac{C_2}{C_1}\frac{E}{(1-\nu)\sigma_i}\left(\frac{\delta}{a}\right)^2 \ , \tag{3.15}$$

where a, C_1 and C_2 have been defined above.

3.4.2 Experimental procedure for measuring the interface toughness with the blister test

The toughness of the interface between the coating and the substrate is deduced by comparing the experimental (p, δ) curves with the analytical curves described in the previous section. The value of $\mathcal{G}$ is modified until the analytical curve matches with the experimental points in the least square sense.

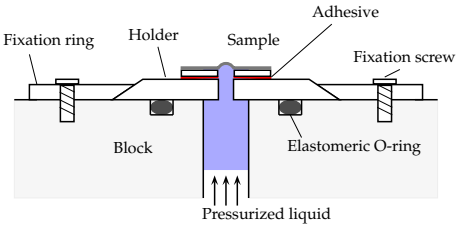

Figure 3.18: Schematic description of the experimental device used for the blister test.

A schematic description of the experimental device is shown in Fig. 3.18. The specimen is glued to the support, which is attached to the testing block. The pressurisation system is included in the block and a pressure sensor is connected to the system. The fluid used to inflate the membrane is demineralized water. The pressure during the test is controlled by varying the injected fluid volume. This way of controlling the test allows more stable delamination. A direct control based on the pressure leads to an unstable crack propagation.

The fringe projection method [60] is used to measure the displacement of the membrane during the test. A laser beam is splitted in two beams, which are combined to produce a set of parallel interference fringes, and projected under a certain angle, on the specimen upper surface. While the surface is deformed by the pressurised fluid, the interval between the reflected laser lines become non uniform as shown in Fig. 3.19.

A top view picture of the specimen is taken by a CCD camera. This image is compared with the reference image taken while the pressure is zero. After image processing done by the program FringeAnalysis from HOLO 3 company, a vertical mapping of the specimen can be made (see Fig. 3.20), from which the deformed profile is determined. The value taken into account is the maximum value of the specimen deflection. The measured value and the corresponding pressure are then used to evaluate the membrane adhesion. The measured values are plotted in a graph and compared with the analytical curves.

A typical (p, δ) curve resulting from a blister test is shown in Fig. 3.21.

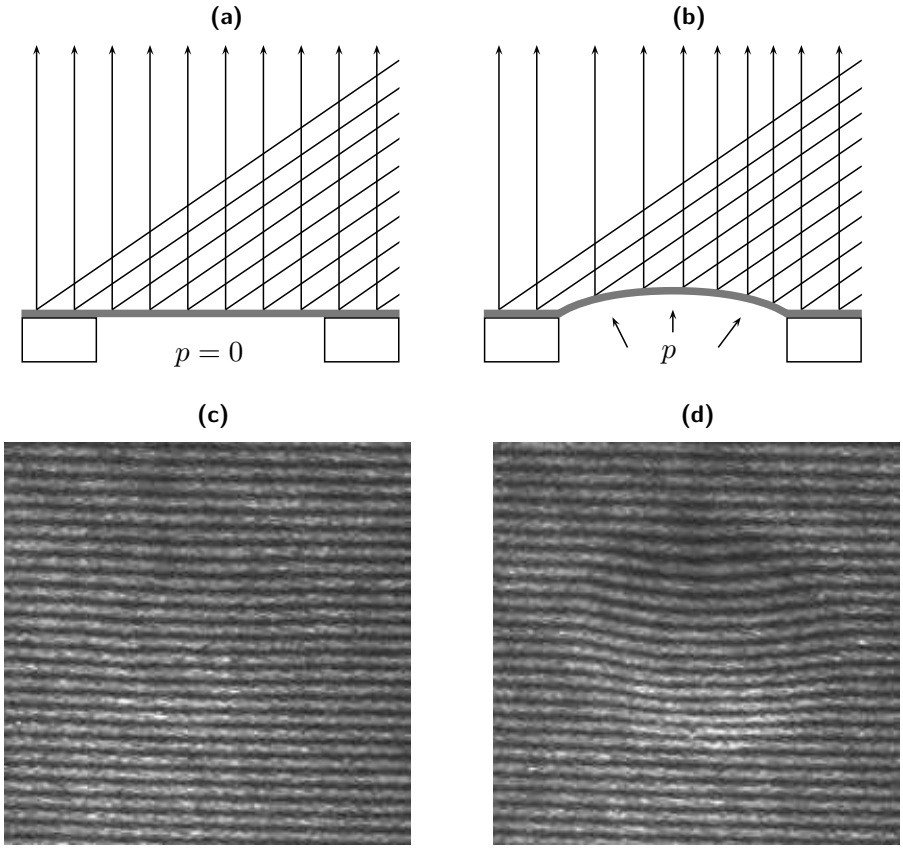

Figure 3.19: Side and top view of the laser beams reflexion of a non-deformed specimen (a,c) used as reference and of a deformed specimen (b,d) taken from [42].

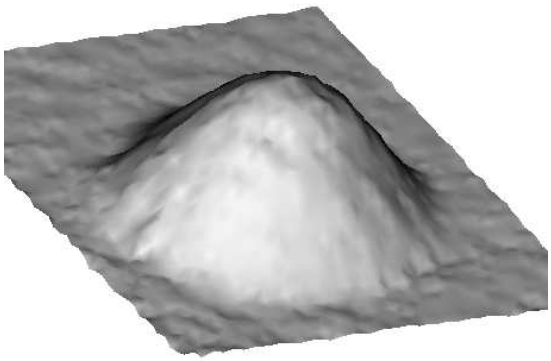

Figure 3.20: Mapping of the deformed specimen.

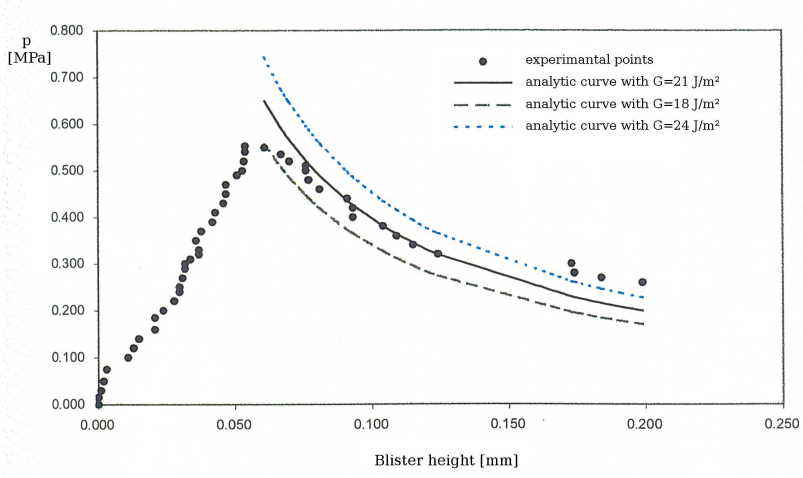

Figure 3.21: Typical curve obtained after a blister test. The points represent the experimental data measured during the test and the lines represent the analytical expression (3.13) for different values of $\mathcal{G}$. Picture from ref. [40].

3.5 Four-point bending test

3.5.1 General description

The configuration of the four-point bending test is shown in Fig. 3.22. As it is for the wedge opening test, the specimen is a bilayer. In the case of a thin film, an extra plate is adhesively bonded on top of the system of interest to increase the elastic energy stored. A cut is made through the upper part of the specimen (the upper substrate) right down to the interface of interest. This cut is performed in order to initiate the crack at the right interface. Upon loading, the crack jumps along the interface and propagates in a stable way along the interface.

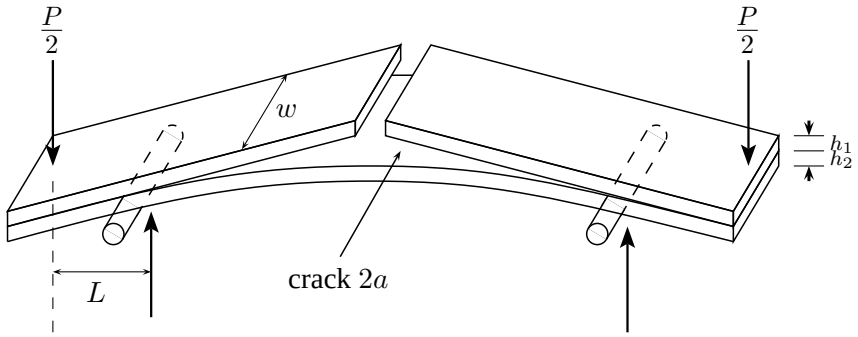

Figure 3.22: Geometry of the four-point bending test.

The test is performed using a universal testing machine. The lower part of the specimen rests on two supports. The loading P is applied on the upper part of the specimen with two supports separated by a distance L from the lower supports (see Fig. 3.22). In the rest of this section, the number '1' (thickness h_1, mechanical properties E_1 and ν_1) refers to the upper part of the specimen, which is relaxing the stress during the test and the number '2' (thickness h_2, mechanical properties E_2 and ν_2) refers to the substrate, which remains loaded during the entire duration of the test.

The main advantage of the four-point bending is that crack propagation takes place under constant applied moment M. Indeed, for a sufficient

crack length $a > h_1$ and h_2, the energy release rate is independent of the crack length (as long as it remains between the inner supports) [12], as explained in the next section.

3.5.2 Analytical expression for the energy release rate

A simplified schematic configuration of the four-point bending test is shown in Fig. 3.23. The grey part represents the coating (one or more thin layer(s)) and the adhesive layer. The interface of interest is the interface between #2 and the coating.

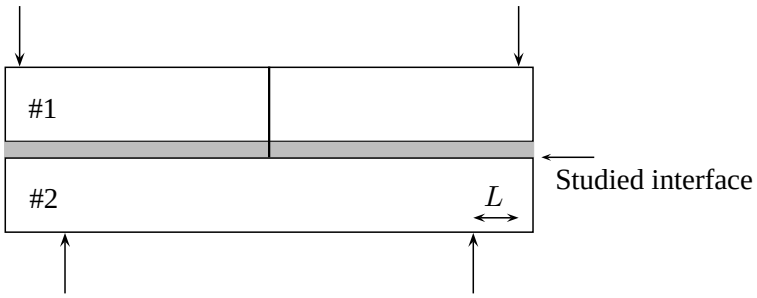

Figure 3.23: Simplified schematic of the four-point bending test. The grey part represents the different layers between the two substrates (coating and adhesive in the present case).

As for all the tests presented up to now, solving the problem in terms of the energy release rate is easier than in terms of the stress intensity factor K. Indeed, the energy release rate can be directly derived from simple energetic considerations if the grey layer shown in Fig. 3.23 is neglected (because $t \ll h_1 \simeq h_2$).

The bending moment between the two inner supports is constant

$$M = \frac{PL}{2} \ , \tag{3.16}$$

as derived from basic beam bending theory. After crack initiation, propagation takes place at constant loading and M remains thus constant [14]. Looking at a section of the delaminating specimen (Fig. 3.24) with constant bending moment, the problem is reduced to a well known

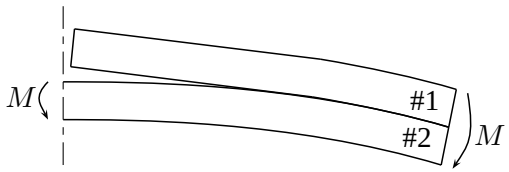

Figure 3.24: Bounding conditions used to determine the analytical expression of $\mathcal{G}_{ss}$.

configuration (see for instance [65]). During crack propagation, the stress field at the crack tip simply translates. The change of elastic energy due to the propagation (i.e. the energy release rate) can be determined from the difference between the elastic energy far away in front of the crack tip and far beyond the crack tip. The elastic energy in front of the crack tip is stored within the entire thickness of the specimen (composite beam formed by #1 and #2) but behind the crack tip, elastic energy is only stored in the lower beam, #2.

Using the Euler-Bernouilli beam theory, see [67], the elastic energy by unit length stored in a beam of width w in bending is given by

$$U = \frac{M^2}{2\bar{E}I} \ , \tag{3.17}$$

where I is the second moment of area [16]. Eq. (3.17) is used to calculate the energy upstream and downstream, respectively, as

$$U_{up} = \frac{M^2}{2\bar{E}_C I_C} \quad \text{and} \quad U_d = \frac{M^2}{2\bar{E}_2 I_2} \ , \tag{3.18}$$

where

$$\begin{aligned}
&\bar{E}_C = \bar{E}_1 \ , \\
&I_C = w\left(\frac{h_1^3}{12} + \frac{\bar{E}_2 h_2^3}{12\bar{E}_1} + \frac{\bar{E}_2 h_1 h_2 (h_1+h_2)^2}{4(\bar{E}_1 h_1 + \bar{E}_2 h_2)}\right) \qquad \text{(see [67], p.400)}, \\
&I_2 = w\frac{h_2^3}{12} \ .
\end{aligned}$$

The energy release rate during crack propagation is determined as the difference between U_{up} and U_d, i.e.

$$\mathcal{G}_{ss} = \frac{1}{w}(U_d - U_{up}) \tag{3.19}$$

$$= \frac{1}{8}\frac{P^2L^2}{\bar{E}_2 w^2}\left(\frac{1}{\frac{h_2^3}{12}} - \frac{\frac{\bar{E}_2}{\bar{E}_1}}{\frac{h_1^3}{12} + \frac{\bar{E}_2 h_2^3}{12\bar{E}_1} + \frac{\bar{E}_2 h_1 h_2 (h_1+h_2)^2}{4(\bar{E}_1 h_1 + \bar{E}_2 h_2)}}\right) \tag{3.20}$$

$$= \frac{1}{8}\frac{P^2L^2}{\bar{E}w^2}\left(\frac{21}{2h^3}\right) \quad \text{while } h_1 = h_2 = h;\ E_1 = E_2 = E. \tag{3.21}$$

3.5.3 Procedure for measuring the interface toughness using the four-point bending test

During a four-point bending adhesion test, three main steps can be distinguished with respect to crack initiation and propagation as explained in ref [27]. The load-displacement curve in Fig. 3.25 explicitly shows these 3 steps.

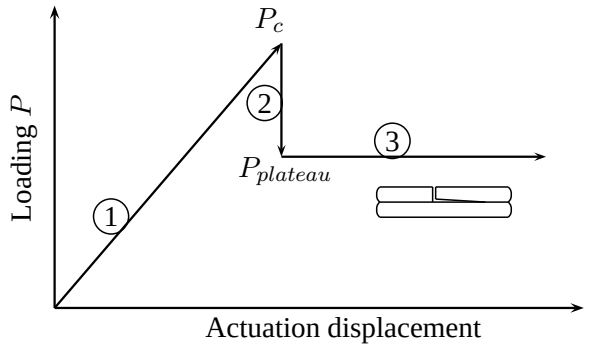

Figure 3.25: Typical load-displacement curve resulting of a four-point bending adhesion test, highly inspired from [27].

1. The first step is the loading before crack initiation. The two parts of the specimen remain bonded together and elastic energy is stored in both arms. The load increases linearly with displacement.

2. The second step begins once the specimen has stored enough elastic energy to initiate the crack. The load reaches the critical value P_c and then falls due to unstable crack propagation and the reduced amount of energy needed to sustain cracking as the crack length increases. The crack is finally stopped by the interface and bifurcates along the interface.

3. The third step is the most important. The loading remains constant. The crack propagates steadily along the interface. The value $P_{plateau}$ of the loading is used in Eq. (3.20) to determine the interface toughness of the coating.

In some cases, the difference between P_c and $P_{plateau}$ can be important. The specimen stores a lot of energy before crack initiation. This energy relaxes just after the cracking initiation. The amount of energy available can be high enough to propagate the crack instantaneously throughout the specimen along the interface. The plateau loading is then no longer captured.

In order to avoid this problem and to produce a long third step, it is sometimes helpful to pre-initiate the crack. This can be achieved by starting the test with a *three*-point bending configuration. During three-point bending, the moment is maximum below the middle support and decreases while the crack starts running along the interface. The risk for the crack to propagate throughout the entire specimen is then reduced.

Part II

Development of the testing method

Chapter 4

Extended wedge opening test

This chapter describes the extension of the wedge opening test procedure developed during this thesis. The key parameter of the interface toughness measurement using the wedge opening test is the crack length as it enters the equation to compute the energy release rate, Eq. (4.1), at a fourth power. An important part of this work has been devoted to setting up a reliable measurement of the crack length value, a, for non transparent substrates using the displacement profile of the bended arms behind the crack tip, as initially suggested by [8].

4.1 Principle of the test

The wedge opening test consists in propagating a crack by insertion of a wedge between the two parts of the specimen as shown in Fig. 4.1. The dimensions of the wedge and of the specimen are known. For a symmetric specimen, the energy release rate is deduced using linear elastic beam bending theory [41], as

$$\mathcal{G} = \frac{3\bar{E}h^3D^2}{16a^4}\left(1 + 0.674\frac{h}{a}\right)^2 . \tag{4.1}$$

where $\bar{E} = E/(1-\nu^2)$ is the plane strain modulus and D is the wedge thickness. The other variables are defined in Fig. 4.1: h is the arm

thickness and a is the crack length. The correction multiplicative term $(1+0.674h/a)^2$ takes into account the effect of the root rotation associated to the presence of shear stresses in the near crack tip region [43]. Details of the developments leading to Eq. (4.1) can be found in Appendix A on page 181. Comparison between two expressions of the energy release rate, Eq. (3.1) which does not takes into account the shear at the crack tip and Eq. (4.1) which includes shear, to the exact solution determined by finite elements simulation is made in the following section. The expression without shear from Eq. (3.1) is designed by $\mathcal{G}^{\text{base}}$ and the more accurate value from Eq. (4.1) by $\mathcal{G}$.

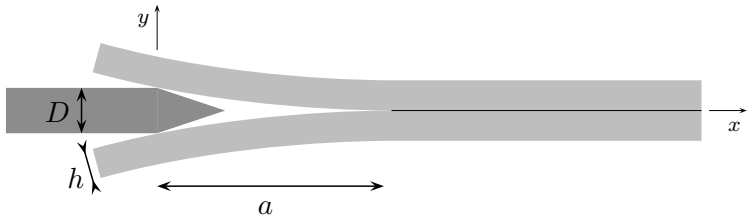

Figure 4.1: Description of the wedge opening test geometry. The different geometric parameters required to compute the interface toughness, the wedge thickness, the specimen thickness and the crack length are shown.

4.2 Crack length measurement

As indicated earlier, the measurement of a must be very accurate to limit the error on $\mathcal{G}$. In the case of transparent specimens, the crack length can be measured directly [5,7,70]. When using a non transparent substrate, the crack length must be deduced by another method. Such an indirect method has been developed in the present thesis following an earlier attempt by Bertholet et al. [8] and Olbrechts et al. [53]. The idea is to determine the crack length a from the full out of plane displacement profile of the specimen. The fact that it is a field measurement and not a single point value is an important contribution of this thesis. This method, which has been used extensively during this work, is explained in the present section.

4.2.1 Analysis of the displacement profile

One arm of the wedge opening test specimen can be compared to a beam deformed by an imposed displacement at distance a from the crack tip. This situation is shown in Fig. 4.2. Two cases are considered: a beam on an elastic foundation and a built-in beam. In the case of a beam on an elastic foundation (Fig. 4.2(a)), the configuration is close to the real specimen deformation but it requires introducing proper properties for the foundation. The specimen can also be compared with a built-in beam (Fig. 4.2(b)) which is less accurate at the near crack tip but does not require any additional information. Different modelling of the specimen vertical displacement are compared in this section.

(a) *Comparison with a beam on elastic foundation.*

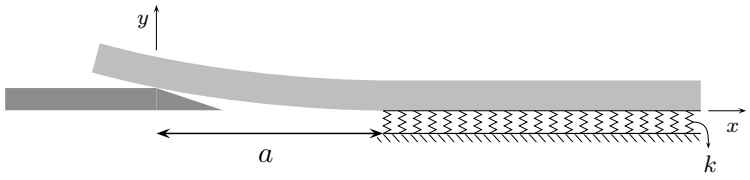

(b) *Comparison with a built-in beam.*

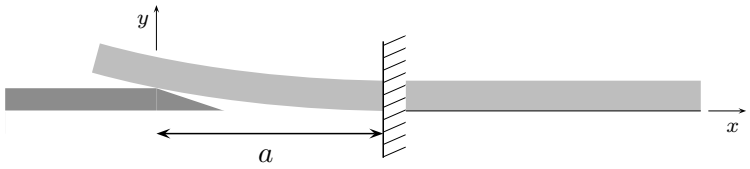

Figure 4.2: Comparison between the wedge opening test configuration (Fig. 4.1) and a beam on (a) an elastic foundation or (b) clamped with an imposed displacement at the end.

Euler-Bernoulli clamped beam

The basic model used in this thesis relies on an Euler-Bernoulli clamped beam. This model was used in a former work [8]. The specimen is compared with a clamped beam with zero thickness. The analytic solution for the vertical displacement $u_y^{\text{E-B}}$ along the x-axis of the clamped

beam of length a and displacement $D/2$ imposed at the extremity (see Fig. 4.2(b)) writes

$$u_y^{\text{E-B}}(x) = \frac{D}{4}\left(2 - 3\frac{x}{a} + \frac{x^3}{a^3}\right) . \tag{4.2}$$

Timoshenko clamped beam

The Timoshenko theory improves of the Euler-Bernoulli theory by taking into account the effect of shear within the beam. Considering a beam of thickness h, the analytic solution for the vertical displacement u_y^{T} along the x-axis of a clamped beam of length a and displacement $D/2$ imposed at the extremity (see Fig. 4.2(b)) writes

$$u_y^{\text{T}}(x) = \frac{\Delta}{2}\left[\left(\frac{\nu}{2a} - \frac{2a(1-\nu)}{h^2} - \frac{1}{a}\right)x + \frac{2(1-\nu)}{3ah^2}x^3 + \left(\frac{4(1-\nu)a^2}{3h^2} + 1\right)\right] , \tag{4.3}$$

with

$$\Delta = \frac{D}{\frac{4}{3}(1-\nu)\frac{a^2}{h^2} + 1} . \tag{4.4}$$

This expression reduces to Eq. (4.2) when h/a is small meaning that the terms involving h^2/a^2 can be neglected.

Euler-Bernoulli beam on elastic foundation

The two preceding beam formulations consider a built-in beam which means that the fixation prevents any deformation in the beam at the fixation point. For crack propagation, the stiffness of the interface in front of the crack tip is not infinite. The beam deforms in front of the crack tip. This phenomenon is called *root-rotation*. Different formulation have been proposed to take into account the root-rotation [13, 33, 74]. We will use the formulation made by Kanninen [33] which consider an

Euler-Bernoulli beam and a Winkler type foundation. The beam of length L is attached using an elastic foundation over a length c (with $L = c + a$). The analytical expression for the vertical displacement u_y^{ef} along the x-axis of the beam for the interval $(0, a)$ is given by

$$u_y^{\text{ef}} = \frac{3D}{h^3\lambda^3\Phi}\left(\frac{\lambda^3(x-a)^3}{3} + a\lambda^3(x-a)^2 - A\lambda(x-a) + B\right) , \quad (4.5)$$

where

$$A = \left[\frac{\sinh^2\lambda c + \sin^2\lambda c}{\sinh^2\lambda c - \sin^2\lambda c}\right] + 2a\lambda\left[\frac{\sinh\lambda c\cosh\lambda c - \sin\lambda c\cos\lambda c}{\sinh^2\lambda c - \sin^2\lambda c}\right] \quad (4.6a)$$

$$B = \left[\frac{\sinh\lambda c\cosh\lambda c + \sin\lambda c\cos\lambda c}{\sinh^2\lambda c - \sin^2\lambda c}\right] + a\lambda\left[\frac{\sinh^2\lambda c + \sin^2\lambda c}{\sinh^2\lambda c - \sin^2\lambda c}\right] \quad (4.6b)$$

and

$$\Phi = \frac{2}{\lambda^3h^3}\left[2\lambda^3a^3 + 6\lambda^2a^2\left(\frac{\sinh\lambda c\cosh\lambda c - \sin\lambda c\cos\lambda c}{\sinh^2\lambda c - \sin^2\lambda c}\right)\right.$$
$$\left. + 6\lambda a\left(\frac{\sinh^2\lambda c + \sin^2\lambda c}{\sinh^2\lambda c - \sin^2\lambda c}\right) + 3\left(\frac{\sinh\lambda c\cosh\lambda c + \sin\lambda c\cos\lambda c}{\sinh^2\lambda c - \sin^2\lambda c}\right)\right] . \quad (4.7)$$

The stiffness of the interface is determined by the factor λ which writes

$$\lambda^4 = \frac{3k}{Ebh^3} , \quad (4.8)$$

where k is the stiffness of the spring modelling the foundation (see Fig. 4.2(a)). In his paper, Kanninen gives an expression for k which does not depend on the interface but on the elastic properties of the specimen only: $k = 2Eb/h$. In this thesis, an up to date value given in [43] will be used as

$$k = 1.615\frac{Eb}{h} , \quad (4.9)$$

with the numerical constant determined more precisely by comparison with FE simulations.

4.2.2 Comparison between the theoretical expressions

The three analytical expressions for the vertical displacement profiles given in the previous section will be compared to FE simulation results. Details about the numerical code used to model the wedge opening test are given in Chapter 6. These three profiles will be compared on the same basis and the profile resulting of the numerical simulation will be used as the reference profile. Mean square fit of each analytic equation with respect to the reference profile will be made independently to determine the value of a which best fits the simulation profile. One important parameter of the problem is the ratio h/a. Two cases will be considered: a specimen with a value of $h/a = 0.02$ and another with a value of $h/a = 0.12$. The parameters used for the simulations are shown in Table 4.1. These parameters correspond to a typical interface response such as addressed in Chapter 6.

Table 4.1: Parameters of the materials and of the interface used to compare the analytic profiles with FE simulations.

h	$100\,\mu m$
E	$200\,GPa$
$\hat{\sigma}$	$2\,GPa$
Γ_0	$1.34\,J/m^2$

The wedge thickness D is set to $100\,\mu m$ which is the thickness of the wedge used for the experimental tests.

The comparison between the analytical expressions (4.2), (4.3) and (4.5) and the profile obtained with FE simulation are shown for the different values of h/a on pages 67–68. The profiles are given in Fig. 4.3 and 4.4 with a zoom close to the near crack tip region. The coordinate x refers to the axes shown in Fig. 4.1. The numerical values of the crack length and of the energy release rate are given in Table 4.2 and 4.3. The exact values corresponding to FE simulations are given at the bottom of each table.

As expected, the analytical expressions give very similar results for a small value of h/a (see Fig. 4.3). A small value of h/a lead to small

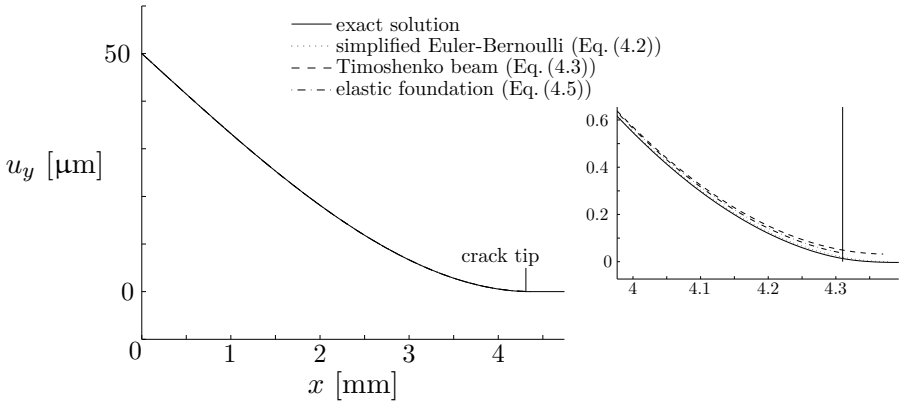

Figure 4.3: Comparison between the different beam bending models and the exact profile from extracted numerical simulations. A zoom close to the crack tip (vertical line) has been made to show clearly the differences between the different curves.

Table 4.2: Comparison between the predictions of the different beam bending models regarding the crack length and between the two expressions used to compute the energy release rate in the case of $h/a = 0.02$.

	$a\,[\mu\mathrm{m}]$	$\mathcal{G}^{\mathrm{base}}\,[\mathrm{J/m^2}]$	$\mathcal{G}\,[\mathrm{J/m^2}]$
Euler-Bernouilli beam	4.38 +1.62%	1.12 −6.76%	1.15 −6.38%
Timoshenco beam	4.38 +1.52%	1.12 −6.30%	1.16 −5.92%
E-B beam on elastic foundation	4.31 +0.05%	1.19 −0.19%	1.23 +0.21%
Simulation (exact solution)	4.31	1.19	1.23

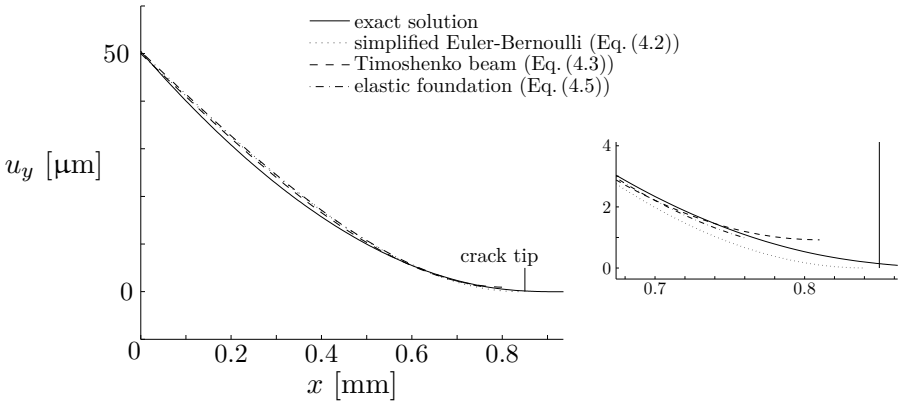

Figure 4.4: Comparison between the different beam bending models and the exact profile from extracted numerical simulations. A zoom close to the crack tip (vertical line) has been made to show clearly the differences between the different curves.

Table 4.3: Comparison between the predictions of the different beam bending models regarding the crack length and between the two expressions used to compute the energy release rate in the case of $h/a = 0.12$.

	$a\,[\mu\mathrm{m}]$	$\mathcal{G}^{\mathrm{base}}\,[\mathrm{J/m^2}]$	$\mathcal{G}\,[\mathrm{J/m^2}]$
Euler-Bernouilli beam	0.84	825.33	955.79
	−1.12%	+4.35%	+6.77%
Timoshenco beam	0.81	955.14	1111.94
	−4.88%	+17.35%	+19.86%
E-B beam on elastic foundation	0.76	1218.91	1432.10
	−11.47%	+35.23%	+37.78%
Simulation (exact solution)	0.85	789.43	891.07

shear stress contribution. The three analytical profiles are also close to the exact profile, even near the crack tip. The values of the crack length given in Table 4.2 confirms that the evaluated value of a is close to the real value. It is the profile with elastic foundation which gives the best value of the crack length but the other models gives a value larger by about 2%.

The comparison between the analytical profiles and the exact solution is worst for a high value of h/a (see Fig. 4.4). The three estimations of the crack length are smaller than the true crack length. In this configuration, the beam on elastic foundation gives the worst evaluation of the crack length. The numerical values of the crack length for the different profiles are given in Table 4.3 and the beam on elastic foundation model lowers the crack length by more than 10%. All the models overestimates the energy release rate value.

The comparisons given above are made with two extreme values of the parameter h/a and the variations are large between the two cases. The experimental tests made during this thesis and explained in Chapter 6 involves an intermediate value of the ratio h/a around 0.05. A FE simulation has been made for such a value of the ratio h/a and the

Table 4.4: Comparison between the predictions of the different beam bending models regarding the crack length and between the two expressions used to compute the energy release rate in the case of an intermediate value of the ratio $h/a = 0.05$.

	$a\,[\mu m]$	$\mathcal{G}^{base}\,[J/m^2]$	$\mathcal{G}\,[J/m^2]$
Euler-Bernouilli beam	2.16 +2.25%	18.98 −9.53%	20.12 −9.67%
Timoshenco beam	2.15 +1.80%	19.33 −7.55%	20.50 −7.66%
E-B beam on elastic foundation	2.09 −1.06%	21.69 +4.13%	23.04 +4.19%
Simulation	2.11	20.79	22.07

comparison values are given in Table 4.4. The error made on a and $\mathcal{G}$ are the higher for the simple Euler-Bernoulli model but the two other do not differ very much in absolute value. The model using a Timoshenko beam overestimates the crack length by 1.8% and the model using the beam on an elastic foundation lowers the crack length by 1.1%. Both are acceptable and the reason to choose one or the other should be based on the studied system and mainly on the expected ratio h/a.

The impact of $\hat{\sigma}$ on the root rotation has been studied earlier in [43]. The value used to determine the effect of the cohesive strength is $\bar{E}\Gamma_0/\hat{\sigma}^2 h$. For values lower than 0.4, the cohesive strength has a negligible effect on the deformation and fracture of the specimen. In the present case, the value of this ratio is lower than 10^{-3}. The effect of a variation of $\hat{\sigma}$ was then not been studied in this work.

Experimental evaluation of the crack length

The evaluation of the crack length is made through the vertical displacement of the specimen. The precision on the measurement is of prime

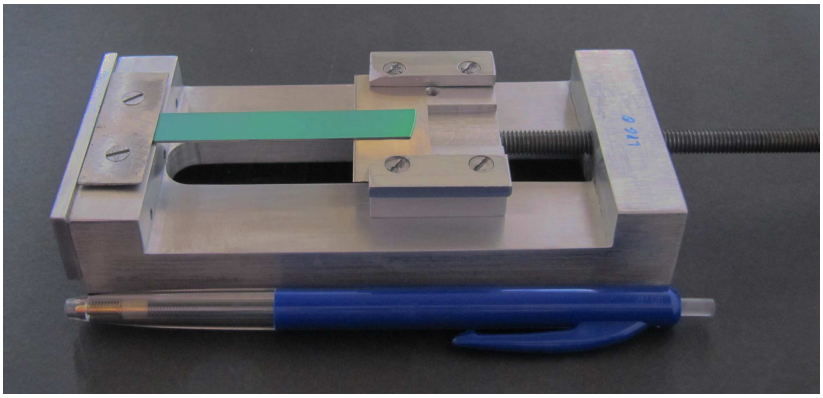

Figure 4.5: Experimental testing stage used to perform the static wedge opening test and measure the out of plane displacement field under a profilometer (plans are given in Appendix B on page 187). The specimen (in green) is fixed on the left and the wedge is inserted in it from the right of the picture.

importance for the accuracy of the method. The vertical displacement of the test specimen can be measured using different techniques: by laser measurement [18], by optical profilometry or by a common contact profilometry method. In this work, the vertical displacement field is measured using a very sensitive recent contact profilometer Veeco Dektak 150. A simple testing stage has been designed to allow a precise positioning of the wedge within the specimen and to allow also the measurement of the vertical displacement fields under the profilometer. An image of the testing stage is shown in Fig. 4.5. The plans of the testing stage are given in Appendix B on page 187.

In order to extract the value of a, the best analytical expression (between Eqs. (4.2), (4.3) and (4.5)) is fitted on the measured profile using a numerical least square optimisation algorithm with the crack length a as the free parameter (see Appendix C on page 191). An example of the fit obtained for a typical experimental measurement is shown in Fig. 4.6. The grey crosses represent some of the measured values of the specimen displacement field. The black lines represents the analytical expressions Eqs. (4.2), (4.3) and (4.5) with the crack length values obtained equal to 8.35, 8.31 and 8.07 mm, respectively.

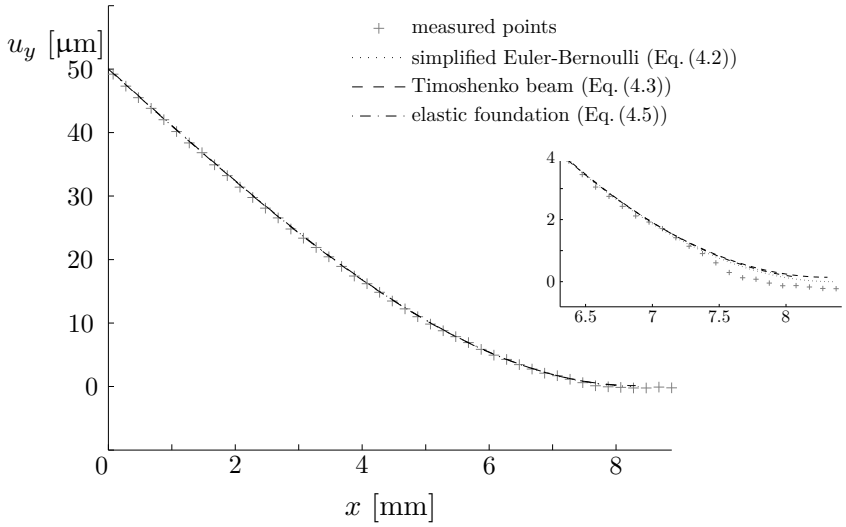

Figure 4.6: Comparison between the measured displacement field (grey cross) and the analytical expressions (Eqs. (4.2), (4.3) and (4.5)) for the best fit crack length a (8.35, 8.31 and 8.07 mm, respectively). The estimated crack length is different for each model and the different values of a are equal to 8.35, 8.31 and 8.07, respectively. A zoom close to the crack tip is shown on the right.

4.2.3 Validation in an application on Si/Si interface

The wedge opening test methodology with crack length estimated from the out of plane displacement field has been validated on an ideal system before being applied to thin films deposited on a steel substrate. The specimens were made of two 380 µm-thick silicon beams joined by wafer bonding (i.e. by molecular interaction between very flat surface) see [7]. The specimens present the advantage of being transparent to IR radiation allowing also a direct measurement of a (see Fig. 4.7). The testing stage used to perform the test (see Fig. 4.5) is designed to allow the measurement of the crack length using both methods without changing the wedge position.

The crack lengths obtained by the two methods are shown in Fig. 4.8. The measurements are made on the same specimen with the wedge ex-

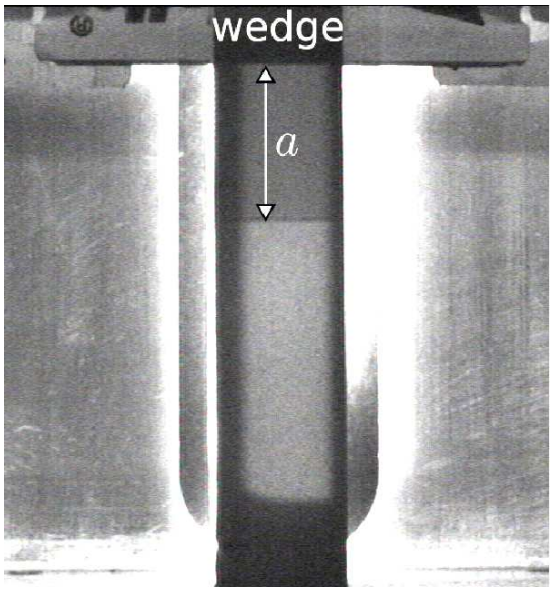

Figure 4.7: Optical image of the crack during the test in the case of silicon substrates, transparent to infrared light. The wedge is inserted from the top of the picture.

actly at the same position. The measurements are made one after the other so there are just a few minutes between the measurements made by the two different methods.

The effective crack length extracted by the measurement of $u_y(x)$ with Eq. (4.5) (the triangle in Fig. 4.8) is larger than the crack length measured directly on the IR image (the square in Fig. 4.8) by typically 3%. The main reason for this small discrepancy is related to the minimum height of the air gap, which can be detected using IR radiation (see [6, 68]). The error writes

$$error(a) = \frac{a_{real} - a_{measured}}{a_{real}} \approx 4.3\% \tag{4.10}$$

while not taking into account the vertical displacement of the specimen at the crack tip due to the root rotation which is low as $h/a = 0.03$ (see Section 4.2.2).

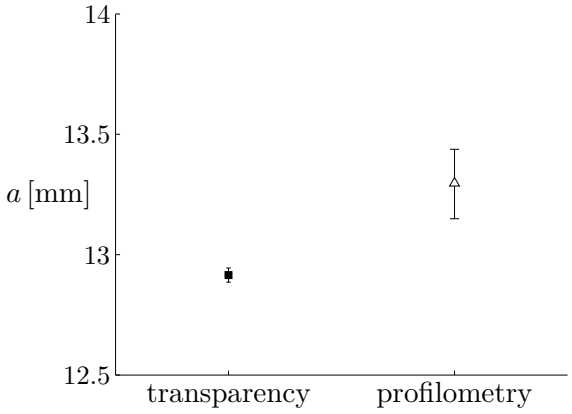

Figure 4.8: Comparison between the two crack length measurement methods. The results correspond to an average over several repetitions at the same wedge position. The error bars shows all the measurements made on the same crack. It corresponds to the scattering related to the instrumentation.

4.3 Application of the wedge opening test to thin film adhesion

The wedge opening test cannot be directly applied to measure the interface toughness of a thin film on a substrate. The insertion of the wedge between the film and the substrate is not possible. Moreover, the film is too thin to store the elastic energy needed for the propagation of a crack. The solution used during this work consists in bonding another plate, identical to the substrate, on top of the film[1] as shown in Fig. 4.9.

The upper substrate is identical to the base substrate in order to avoid global mode mixity effects. The computation of the crack length and the energy release rate is also simplified using a symmetric specimen. The coating and the adhesive layer used to bond the upper substrate are much thinner than the substrate thickness and are neglected in the

[1] In the rest of this document, this second substrate will be called *upper substrate* (another term used by some authors is 'superstrate', tough this word does not exist in the English dictionary).

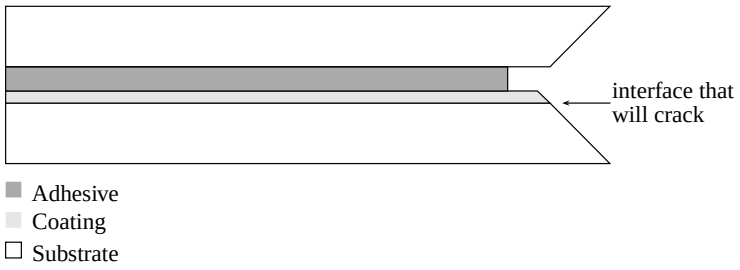

Figure 4.9: Schematic view of the specimen with the different layers: substrate, coating, adhesive and the upper substrate.

analytical analysis of the wedge opening test.

In order to facilitate the wedge insertion, a groove is made on the substrate and the upper substrate. In addition, the adhesive layer is not applied on the entire specimen surface (see Fig. 4.9). The coating is very thin so the crack can easily cut through and propagate along the interface between the substrate and the coating. But, the interface selected for decohesion is not controlled. The crack propagates along the weakest interface. The two interfaces on each side of the adhesive have thus to be as strong as possible. The preparation of these two surfaces is important and made as follows.

- The coating is rinsed with norvanol[2] and dried with hot air. No additional 'aggressive' preparation is allowed on this surface in order to avoid changing the coating properties.
- The upper substrate is ground using SiC abrasive paper in order to increase the roughness and the mechanical adhesion with the adhesive layer. The surface of the upper substrate is, afterwards, cleaned with demineralized water, rinsed with norvanol and dried with hot air.

The upper substrate is then bonded using a commercial cyanoacrylate adhesive (Loctite SuperGlue-3 Easy Brush[3]). The adhesive is applied

[2]a combination of ethanol (83.5%), ether (2.5%) and water (14%).

[3]The worksheet of the adhesive can be find on the internet website

with a brush to obtain a layer as uniform as possible. The two parts are then pressed together during at least 12 hours.

The interface between the coating and the substrate is considered to be the weakest. After the delamination of the specimen is complete, the surface of decohesion is analysed in order to determine the real decohesion interface.

The specimen preparation is similar for the four-point bending test. The preparation for the blister test does not require any special preparation of the specimen and the superlayer method is integrated in the deposition process. This is the reason for which only the specimen preparation for the wedge opening test is presented in details.

The development of the method to measure thin film adhesion has been made on nitride coatings deposited by sputtering on a stainless steel substrate. The observations and results are developed in Chapter 5.

`http://www.rectavit.be/fr/ProductTechnischeFiche.aspx?productid=75` (last visited on October 5th 2010)

Part III

Adhesion of thin coatings

Chapter 5

Application of the wedge opening test to titanium nitride coating on stainless steel

Titanium nitride is an ultra-hard material with the appearance of gold [1]. The most common use of TiN coating is for edge retention and corrosion resistance of machine tooling (i.e. drill bits or milling cutters), providing a lifetime improvement by a factor of three or more. Because of its goldish colour, TiN is also widely used as a top-layer in jewellery or other domains for decorative purposes. TiN coatings are used as the top-layer on all these applications and the adhesion is thus of prime importance. This is the reason, for which the first coating selected to apply the adhesion measurement method, in collaboration with Arcelor-Mittal, has been TiN. Thicknesses lower than 100 nm have been chosen, corresponding to the thicknesses produced on the industrial line.

The wedge opening test to measure thin film adhesion has been applied first to thin nitride films deposited by plasma sputtering on a stainless steel substrate. The coating has been deposited under different process conditions to study their influence on the interface toughness. This coating has been used primarily to set up a robust testing procedure for the wedge opening test. It turned out that the scatter in the interface toughness did not allow quantitative analysis of the different sources

of energy dissipation. The scatter is the result of the absence of etching (cleaning of the surface) during the deposition process, which was decided to lower the interface toughness.

The first section of the chapter describes the plasma sputtering deposition method. The next section provides the process parameters used to deposit the nitride film. This chapter continues with the description of the interface toughness measurement results obtained by the wedge opening test and a discussion of these results.

5.1 Plasma sputtering

The plasma sputtering deposition method belongs to the physical vapour deposition (PVD) processes. The PVD processes are used to make coatings (ceramic or metallic) in a wide range of fields. From a general point of view, the coatings are made under high vacuum in three steps: the creation of a metallic vapour from a source (the *target*), its transport in a reactor and its condensation at the surface of a substrate.

The word PVD refers to a large number of processes, which can be classified under three main categories following the way the metallic vapour is obtained: (i) by thermal effect, called then 'evaporation' or (ii) by mechanical effect, called then 'sputtering' or (iii) by combination of the two previous effects, called then the 'cathodic arc under low pressure'.

Plasma sputtering belongs to the second category. The use of magnetron plasma sputtering constitutes a way to increase the efficiency of the deposition. It is more used than the classic plasma sputtering method.

Sputtering

A high vacuum is created in the reactor chamber prior to filling it with a low pressure inert gas atmosphere. Argon is mostly used for economical reasons. The target is brought to a highly negative polarisation and a plasma is created between the target (cathode) and the chamber (anode). The Ar^+ ions created in the electric discharge are accelerated towards the cathode surface and release the acquired energy during the

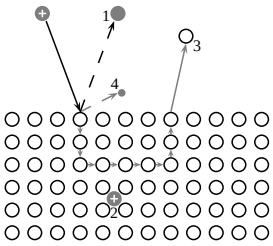

Figure 5.1: Possible scenarios resulting from the impact of an accelerated ion. The result of the incident ion can be: (1) elastic reflexion of the ion; (2) implementation of the ion in the target; (3) expulsion of a surface atom; (4) secondary electronic emission. Inspired from [10].

impact with the target (see Fig. 5.1). The way the energy is released depends on the characteristics of the electric discharge and on the physical and chemical properties of the target.

The spatial distribution of the metallic atoms released by the target is an important parameter of the deposition. In a first approximation, it has an ellipsoidal distribution. The shape of the ellipsoid is function of the fraction of ejected metal in a direction matching an angle θ with the normal to the target. An increase of the ion impact energy and a lower mass of the target metal leads to a less dispersed sputtering of the metal. The gradient of the coating thickness on a non-moving substrate is then more important.

Magnetron effect

The two main disadvantages of the deposition by sputtering are: (i) the low ionisation rate leading to a low deposition speed ($<0.1\,\mu m\,h^{-1}$) and (ii) the high number of collisions of the metallic atoms and of the plasma ions leading to a low speed of the metal atoms while hitting the substrate. These two effects often lead to a porous coating structure.

These two problems can be avoided by addition of a magnetron, which consists in a circular magnet introduced just behind the target (see Fig. 5.2). The target should be amagnetic and the magnetic flow lines are closing the circuit through the plasma. The secondary electrons are

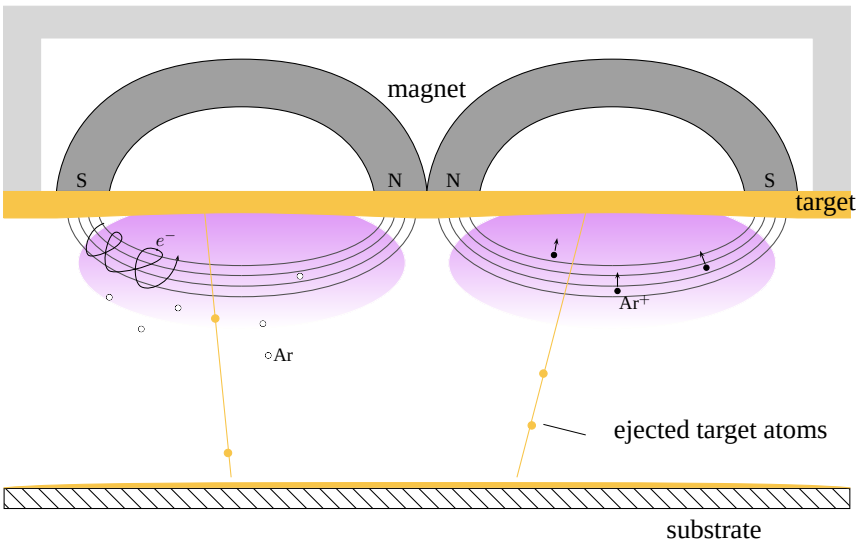

Figure 5.2: Principle of the magnetron plasma sputtering.

then captured by the magnetic field and their density is high near the target. The probability for the electrons to hit an argon atom to maintain the plasma becomes then higher. The plasma can be generated at a lower pressure and thus with a longer mean free path. The atoms from the target have a lower probability to hit other atoms in their way to the substrate. A dense plasma is created close to the target in the magnetic field. This leads to a non homogeneous erosion of the target but the deposition speed is increased to around $10\,\mu m\,h^{-1}$ and the coating is also more dense.

Reactive sputtering

The preparation of ceramic coatings (oxides, nitrides, carbide) can be done in two ways. The first way is to have a target made of the desired material and the second is the sputtering of a metallic target with the metalloid contribution coming from gas injection. The first method has several disadvantages. The most negative aspect is that the deposited coating and the target have not the same stoichiometry. An external contribution of reactive gas is necessary. We will focus in this section

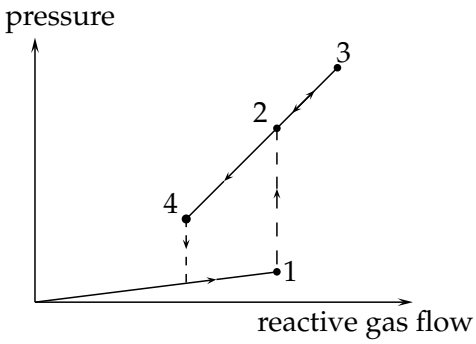

Figure 5.3: Schematic evolution of the pressure in the deposition chamber while increasing the reactive gas flow rate at constant sputtering power.

on the second method with external reactive gas, which we have used to produce our specimens.

The injected gas and the sputtered metal have in some cases a high chemical affinity and the system is highly reactive. This is the case for nitrogen and titanium and also for oxygen and the majority of the metals. In this regime, instability sometimes occurs depending on the gas flow. The deposition regime is changing with the amount of reactive gas injection. This change can be determined by looking at the variation of the pressure in the deposition chamber as a function of the gas flow rate under constant sputtering power. This evolution is schematically shown in Fig. 5.3. First, the pressure rises slowly with the gas flow. The reactive species are trapped on all free surfaces of the deposition chamber (including the target and the substrate). The pressure remains low and the deposited coating is essentially metallic. Once the gas flow reaches a critical value, i.e. the reactive gas flow rate into the chamber becomes higher than the absorbing rate of the chamber (point 1 in Fig. 5.3), a small increase of the gas flow rate leads to a significant increase of the chamber pressure (transition between points 1 and 2). The reactive gas reacts, then, with the sputtered molecules. At higher gas flow rates, the target is completely contaminated by the reactive gas and the sputtering is again stable (zone between the points 2 and 3 in Fig. 5.3). During this regime, the sputtering rate is significantly lower. The sputtering rate from compound targets (metal – ceramic) is lower than that of pure

metallic (or metallic alloy) targets. This results in a smaller amount of metal sputtering and a decrease of the gas consumption. This is why the pressure rises suddenly.

If the gas flow rate is reduced following an increase of the total pressure to a high level, the pressure value will not decrease following the same trajectory as during the increase. The rate of decrease of the total pressure will remain constant down to a reactive gas flow rate lower than the one corresponding to point 1 (until point 4 in Fig. 5.3). This is because the reactive gas pressure remains high until the compound layer on the surface of the target is removed and the metal of the target is directly exposed to the plasma once more. As a result, the consumption of the reactive gas increases (lowering the pressure) and the deposited film is again essentially metallic.

The specimens used in this work have been deposited in the fully reactive regime (zone between points 2 and 3).

Substrate preparation

The preparation of the substrate before the deposition is made in 2 steps. The first consists of a chemical cleaning outside the deposition chamber and the second is an ionic etching in the deposition chamber.

The chemical cleaning is performed within an ultrasonic bath using methyl acetate. In order to remove all impurities and contaminants from this ultrasonic bath, the substrate surface is then rinsed with ethanol and dried with hot air using a hair dryer. The ionic etching is made in the deposition chamber just before the deposition of the coating. The polarity between the target and the substrate is inverted. The ions of the plasma are accelerated towards the substrate, and hit the substrate instead of the target. The purpose of this step is to remove the residual layer of oxide or contaminants. During the etching, it is necessary to hide the target with a shield to avoid the contamination of the target with the particles removed from the substrate as these particles would be susceptible to return on the substrate in the beginning of the deposition. The deposition of the coating follows the substrate preparation for the time required to obtain the desired thickness.

At the end of all these steps, a system made of a substrate and a thin coating is generated and our objective is to measure the interface toughness. The specimen must finally be adapted to the measurement method.

Specimen preparation

The use of the wedge opening test method to measure thin film adhesion requires the bonding of another plate on top of the film. The procedure to prepare the specimen and bond the upper substrate is described in Section 4.3. The plate with the coating is cut to the right dimensions and the upper substrate is bonded. Assuming that the adhesive sticks correctly (i.e. better than the coating to the substrate), the coating will delaminate between the two plates of the specimen.

The dimension of all the specimens used during this work are 10×70 mm to cope with the testing stage size, see Fig. 4.5.

5.2 Interface toughness measurement results

The specimens used to perform the wedge opening tests are all extracted from one stainless steel substrate of A4 paper size. The thickness of the substrate is equal to 0.4 mm. The deposition has been performed using a vacuum deposition machine under a pressure of 0.43 Pa for 3 min. The partial pressure of nitrogen was 6.7×10^{-3} Pa. The substrate was moving under the target in the direction coinciding with its long side. No ionic etching has been performed prior to the TiN deposition. The reason was to promote a lower interface toughness. The TiN coatings are indeed known in the literature to present a good adhesion [79], especially at low thicknesses [23]. The development of the method being easier if the adhesion is poor, the way chosen for diminishing the interface toughness has been to skip the etching step.

Other coatings have been realised for the development of the method. The results of these first tests are not reported here because the energy release rate has not been measured by the same way for each specimen (if it has been measured). They were used to tune the specimen preparation and try some ways to make the crack initiation easier.

The specimens tested by the blister test have been processed on thinner substrates to cope with the restrictions of the method. The specimens used for the four-point bending test have been made on another deposition device and with a cleaning of the substrate with an ionic etching.

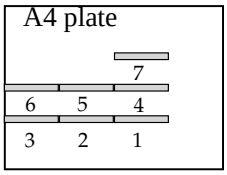

Figure 5.4: Specimens locations.

The test specimens have been cut with the proper dimensions using a manual guillotine from the entire plate with the size of an A4 paper, see Fig. 5.4. Each specimen was designated with a number corresponding to the specimens referenced in Table 5.1. An overlayer, i.e. additional substrate, of the same dimensions has then been glued on top of the coating using cyanoacrylate adhesive Loctite® super glue-3. The specimens were taken from different locations distributed over the plate surface in order to study possible spatial variation of the adhesion.

5.2.1 Interface toughness variations over the surface

The evaluation of the crack length using the out of plane displacement profile requires the measured profile to be properly rotated when treating the data. Indeed, the points taken after the crack tip, corresponding to the non debonded part of the specimen (i.e. $x > a$ in Fig. 4.1 on page 62), must be perfectly horizontal. This levelling can be made directly on the measured points by the software of the profilometer equipment. In this thesis, the first measurements in 2007 – 2008 have been made using an old profilometer without any automatic levelling. The levelling was made manually. A first profile was taken and the location of the bonded region of the sample is determined by analysing the profile. The tilt of the profilometer test table is then adjusted so that the points corresponding to this region are at the same level. This procedure is repeated until the measured profile has the desired shape. For this reason, some time was spent between the wedge insertion and the measurement of the profile. At each wedge location in the specimen, at least three measurements of the profile were taken in order to enhance precision in the extracted crack length. Due to the profilometer tip speed (max 1 cm/s), each

profile measurement took 2 to 3 min. By taking all steps into account, around half an hour was needed for the measurement of one crack length.

This procedure is repeated along the specimen at different locations. The wedge is moved forward by a few millimetres and, after levelling, multiple profiles are measured. The data points extracted from the profilometer are then the input of a home made Scilab program (see Appendix C on page 191), which computes the crack length and the corresponding interface toughness. More precisely, four to six crack length measurements are made along one specimen. The first is taken at 15 mm from the edge and the others every 5 to 10 mm. The measurements are made over a distance of 35 mm to avoid the possible edge effects, which have been previously reported in the case of wafer bonding [6, 7].

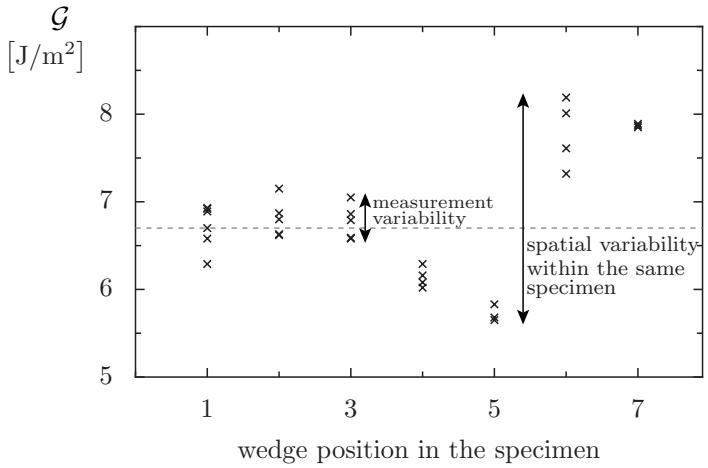

Figure 5.5: Example of measurements taken at different locations on one specimen corresponding to different wedge positions. Several measurements were taken at each wedge position without moving it. This illustrates the variability of the experimental measurement at one point of the specimen and the variability of the measurement along the specimen. The dashed grey line represents the value of $6.7\,\mathrm{J/m^2}$ given by [48].

Figure 5.5 shows measurements taken at different positions on one specimen corresponding to different positions of the wedge. A large number of measurements with the profilometer were taken to analyse its variabil-

ity. These measurements were taken using the old profilometer which has a low precision. This means that for the same wedge position, 2 different profile measurements give a slightly different values of the crack length. Using the new profilometer, the difference on the crack length from two different profiles taken at the same wedge position is less than 5 µm, meaning typically a 0.01 J/m^2 variability over 4.7 J/m^2, representing less than 1%. A reliable crack length value can thus only be obtained if the measurement of the profile is very accurate. Remember that it is important to have a high precision on the crack length as is enters as a fourth power in the equation to compute $\mathcal{G}$, see Eq. (4.1) on page 61.

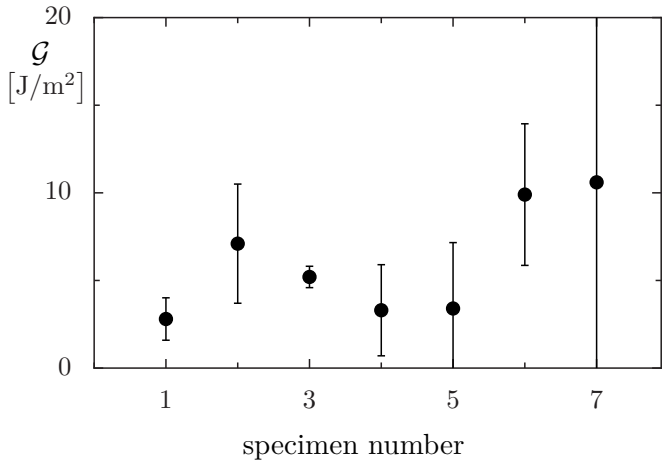

Figure 5.6: Variation of the energy release rate over the whole plate. The size of the error bars represents the variability presented in Table 5.1.

The average interface toughness over all specimens correspond to the value given in [48], which reports an interface toughness of 6.7 J/m^2 for a 1 µm thick TiN coating deposited on a steel substrate without etching. In addition, no trends about clear gradient of interface toughness can be extracted at the scale of the entire plate, see Fig. 5.6.

The measured energy release rate associated to the external loading and the corresponding specimen position over the plate surface are given in Table 5.1. The interface toughness varies a lot over the plate surface. The mean values measured for the different specimens vary between 3 and 10 J/m^2. Some local toughness values are larger than 15 J/m^2.

This high variability most probability comes from the absence of etching during the coating deposition process.

Table 5.1: Interface toughness measured at different positions over the plate surface. Each corresponds to the mean value measured on one specimen at different positions of the crack. Furthermore, four repetitions are made at each position of the crack tip. The variance of the value resulting from one specimen (corresponding to different position of the wedge) is given in the last column. The coordinates given for each specimen are taken from the bottom-right corner of the plate. The positive x-coordinates are pointing toward the left.

specimen #	coordinates [mm]	mean $\mathcal{G}$ measured $\left[\mathrm{J/m^2}\right]$	$\mathcal{G}$ variance [-]
1	(70 ; 60)	2.8	1.2
2	(140 ; 60)	7.1	3.4
3	(210 ; 60)	5.2	0.6
4	(70 ; 100)	3.3	2.6
5	(140 ; 100)	3.4	3.8
6	(210 ; 100)	9.9	4
7	(70 ; 140)	10	37

For the sake of avoiding this spatial variability of the adhesion, one coating has been processed with an ionic etching before the TiN deposition. As expected from literature [23, 48, 79] and industrial experience, this coating involved very high interface toughness with the crack propagating essentially in the adhesive layer and a corresponding energy release rate associated to the external loading equal to about $100\,\mathrm{J/m^2}$, which is a reasonable value for a weak adhesive.

Interface toughness has been measured on different places over the substrate surface. High variability has been observed while no etching has been performed prior the coating deposition. The etching largely increases the coating adherence, making impossible the delamination at the interface of interest.

5.2.2 Time dependent crack propagation

Another important observation is a change of crack length with time. After the wedge insertion, the crack continues to grow, even if the wedge remains at a fixed position. Figure 5.7 shows the evolution of the en-

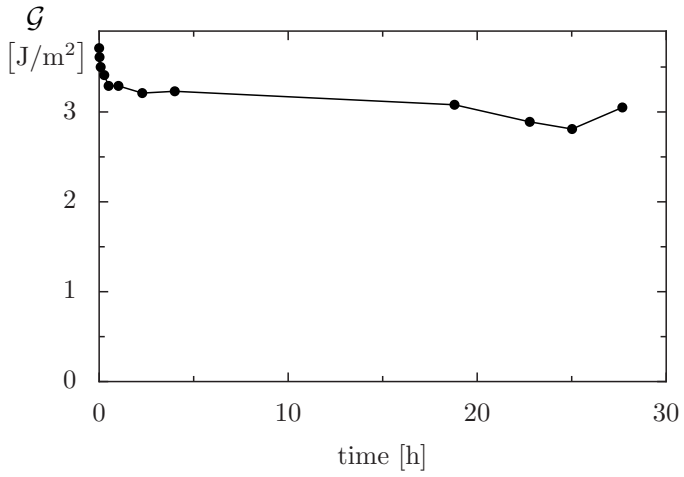

Figure 5.7: Time evolution of the energy release rate measured with the wedge opening test at fixed wedge position. This shows the evolution of the crack length after the positioning of the wedge. Three hours after the wedge insertion, the crack is considered stable.

ergy release rate associated to the external loading measured values at different times after the wedge introduction. The decrease of the energy release rate associated to the external loading value results in an increase of the crack length. The energy release rate associated to the external loading decreases by about $0.5\,\mathrm{J/m^2}$ in the first 3 hours after the wedge insertion. This decrease is attributed to the relaxation of the stress in the adhesive layer. This layer is a viscoelastic material so time has an impact on its behaviour. As a consequence, the measurements of the energy release rate will always be made more than three hours after the wedge positioning for a better repeatability. Crack length measurements are also made just after the wedge insertion (between 0 and 1 min after wedge positioning). In this way, the value change of the measured energy release rate associated to the external loading can be evaluated.

No direct relationship between this variation and the film thickness or stress has been observed. No further study has been made on the adhesive (except the energetic dissipation in this layer). Even if some other adhesives on the market could have better structural properties, the adhesive properties and layer thickness have been held constant for all the results shown in this thesis. The adhesive has been chosen for the ease to bond the upper substrate and the repeatability of the procedure.

At a fixed wedge position, the crack length keeps increasing with time. The crack length measurement has then been performed at a fixed time after the wedge positioning, corresponding to around 3 hours.

5.2.3 Attempts with blister and four-point bending tests

Several attempts have been made to measure the adhesion of TiN on stainless steel using two other methods: the blister test and the four-point bending test. These two methods have been used mostly at INP Grenoble under the supervision of Pr. Michel Dupeux and Dr. Muriel Braccini.

Blister test results

The device used to perform the blister test has been set up at the INP Grenoble. Because of the low thickness of the TiN coating (40 nm), the inverted blister test configuration has been chosen. This configuration imposes the substrate thickness to be smaller than 100 µm. Depositions on thin substrates have been made for this test. This should not influence the value of the interface toughness. The configuration of the

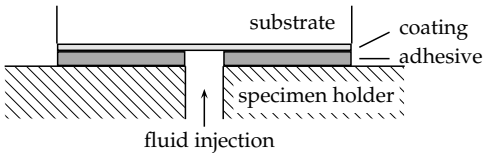

Figure 5.8: Schematic view of the sample configured for the inverted blister test.

specimen is shown in Fig. 5.8. The specimens have been bonded using a bi-component epoxy adhesive (Araldite 90) and the specimen and support have been pressed together for at least 24 h.

The main difficulty has been to initiate the crack at the right interface. Even by removing the coating over the surface corresponding to the fluid injection hole, the crack was propagating along the coating – adhesive interface. Due to the difficulty to prepare new specimens during my stay at the INPG, the limited hope of success and the variability problems exhibited with the wedge opening test, no more investigation to adapt the TiN coating to the blister tests have been made.

Four-point bending test results

Measurements have also been attempted using the four-point bending test. The specimens have been prepared in the same way as for the wedge opening test with the bonding of a plate on top of the coating. The upper substrate of the specimen has been then cut using a circular saw with a blade thickness of 0.5 mm. The depth of this cut was estimated to be long enough to reach and even cross the interface of interest. The goal is to increase the stress at the interface of interest and lower the external load needed to initiate the crack. This was unfortunately not enough to avoid the load jump at crack initiation (segment ② in Fig. 3.25 on page 56).

The solution has then been to load the specimen by three-point bending without reaching the plastic deformation of the specimen. This allows the initiation of the crack without propagating it, because the moment applied decrease while moving away from the centre of the specimen.

The load – displacement resulting curve is shown in Fig. 5.9 for the four-point bending configuration. The test has been performed on a specimen composed with a 0.8 mm thick stainless steel substrate and a 60 nm thick TiN coating deposited after an ionic etching. The upper substrate has the same thickness as the substrate and has been bonded using cyanoacrylate adhesive (Loctite® super glue-3). The size of the specimen is 10×70 mm. The test has been performed in a universal

tensile machine. The speed of the cross head was 0.5 mm/s and the space between the supports $L = 15\,\text{mm}$.

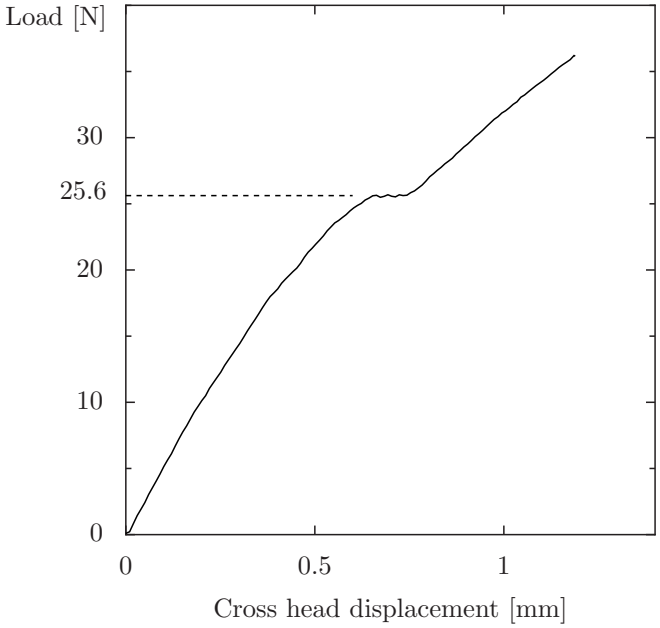

Figure 5.9: Variation of the load applied to the specimen as a function of the machine cross head displacement during a four-point bending test. The interface toughness is computed from the value of the plateau load.

The plateau is clearly visible in Fig. 5.9 and long enough to allow the measurement of the load. There is no peak before the plateau owing to the first loading of the specimen in the three-point configuration. The crack has been initiated and is propagating during the four-point bending test. The value of the interface toughness is computed by inserting the mean load value of the plateau $P_p = 25.6\,\text{N}$ in Eq. (3.21), resulting in

$$\mathcal{G} = \frac{1}{8}\frac{P_p^2 L^2}{\bar{E} w^2}\left(\frac{21}{2h^3}\right) = 17.2\,\text{J/m}^2\ . \tag{5.1}$$

The value of the interface toughness is in agreement with the literature [48], when an ionic etching has been used. Other tests have been

performed with similar specimens made with exactly the same procedure. In these tests, the crack did not propagate at the right interface and was mostly in the adhesive (without any plateau in the load – displacement curve) with a high plastic deformation of the substrate. The reason of these different behaviours is not fully understood.

The attempts with the blister and four-point bending tests have not been conclusive. The initiation of the crack and the repeatability of the specimen preparation are in both cases difficult to perform.

5.3 Conclusions

In this chapter, the wedge opening test interface toughness measurement technique has been adapted to thin films. The deposition process used to deposit the coatings tested in this work has also been explained. The same deposition process (with some variations in the parameters) has been used to produce all the coatings during this work.

Titanium nitride coatings have been used to manage the adhesion measurement of thin film on steel. This coating was an opportunity to set up the wedge opening test, involving: the crack length measurement, the need of an accurate specimen displacement measurement, the measurable adhesion range and its variability. The preparation process of the specimen has also been tuned to make it easy to handle and repeatable. It also puts into light some unwanted effects linked either to the deposition process (i.e. ionic etching) or to the measurement method itself (i.e. the presence of the adhesive layer).

Now, the high dispersion of the results, from 1.5 to 15 J/m^2, makes it difficult to investigate in deeper details the adhesion mechanisms as well as the speculation of the different energy contributions. Furthermore, given the good adhesion of TiN coatings on steel (after ionic etching), further study on this coating regarding the adhesion was not necessary. The decision has been made to change the coating for further development of the method. Copper coating have been chosen, in agreement with the industrial partner ArcelorMittal. The reasons are explained in next chapter, discussing the study on this new coating and the parameters influencing the adhesion and its measurement.

Chapter 6

Adhesion of copper films on steel and separation of energy contributions

This thesis deals with the adhesion of metallic coatings. The ultimate goal of this thesis —and as a matter of fact, in most research efforts addressing the measurement and analysis of interface cracking— is to determine a value of the interface toughness that is as intrinsic as possible (by extracting the extrinsic contributions).

6.1 Introduction

Only intrinsic values can be safely compared when addressing different systems. This requires the capacity to separate the extrinsic and intrinsic energy contributions from the total work. This objective goes along with another important aspect of this part of the thesis: to understand the effects of different parameters on the interface toughness such as the coating thickness, microstructure and possible internal stress. A better understanding of the fracture mechanisms will guide the development of more adherent coatings. In this work, we have used the wedge opening test to measure the adhesion of copper films on stainless steel. The results are developed in this chapter.

The first section of the chapter recalls the basis of the method and gives a short analysis of what can be deduced from the measurements. The next section presents the microstructure and basic properties of the coatings and how they have been determined. The deposition process characteristics are also detailed for all coatings performed in the course of this study. Section 6.5 explains the foundations of the numerical FE code used for simulating the wedge opening test. The results of the simulations are presented in the two following sections. First, an idealized model has been used to determine the influence of the internal stress of the film and of the adhesive layer. Then, the FE code has been used to model the real specimen geometry. The influence of the interface characteristics are addressed. The last section compares the results of the numerical modelling to the experimental results for different coating thicknesses in order to identify the parameters controlling the interface toughness and quantify the different energy contributions for the Cu/steel system.

6.2 The wedge opening test method

The wedge opening test is a widely used technique to measure the adhesion of bonded [5, 7, 59] or welded systems [57], see Section 3.2 on page 26. A wedge is inserted between two beams in order to propagate a crack, as shown in Fig. 6.1. Here, we deal with two beams made of the same material. The interface toughness can be extracted using only geometrical parameters and the Young's modulus of the specimen. There is no need to measure the applied force.

For a symmetric elastic configuration, the energy release rate $\mathcal{G}$ can be determined from an elastic beam bending analysis as

$$\mathcal{G} = \frac{3\bar{E}h^3D^2}{16a^4}\left(1 + 0.674\frac{h}{a}\right)^2 , \tag{6.1}$$

where $\bar{E} = E/(1-\nu^2)$ is the plane strain modulus. See Chapter 4 for more details on the wedge opening test.

The measurement of the adhesion of a thin coating on a substrate using the wedge opening test is a relatively new application of the method,

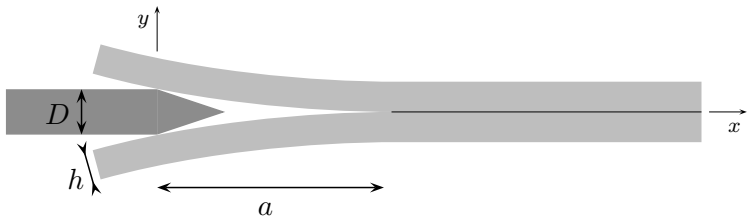

Figure 6.1: Description of the wedge opening test geometry. The different geometric parameters required to compute the interface toughness are: D, the wedge thickness; h, the substrate thickness and a, the crack length.

see [7]. Applying the wedge opening test to the measurement of interface toughness between a thin coating and a substrate requires bonding an additional plate on top of the coating to store enough energy for crack propagation, see Section 4.3 on page 74. This additional layer, involving also a thin glue line for bonding, can introduce different artefacts in the measured interface toughness if it involves internal stress and/or it dissipates energy during fracture. The energy release rate associated to the external loading, $\mathcal{G}$, involves several contributions

$$\mathcal{G} = \underbrace{\Gamma_0 + \Gamma_p^{\mathrm{s}} + \Gamma_p^{\mathrm{f}} + \Gamma_{el}^{\mathrm{s}} + \Gamma_{el}^{\mathrm{f}}}_{\mathcal{G}_c} + \underbrace{\Gamma_p^{\mathrm{adh}} + \Gamma_{el}^{\mathrm{adh}} + \Gamma_p^{\mathrm{upper}}}_{\text{extrinsic contribution}} - \mathcal{G}(\zeta\sigma_i) \ , \quad (6.2)$$

with

Γ_0 : the thermodynamic work of adhesion of the interface;

Γ_p^{s} and Γ_p^{f} : the plastic dissipation in the substrate and coating;

Γ_{el}^{s} and Γ_{el}^{f} : the locked-in elastic deformation in the substrate and coating due to the inhomogeneous plastic deformation occurring during cracking;

Γ_p^{adh} : the plastic dissipation in the adhesive layer;

$\Gamma_{el}^{\mathrm{adh}}$: the locked-in elastic deformation in the adhesive layer due to the inhomogeneous plastic deformation occurring during cracking;

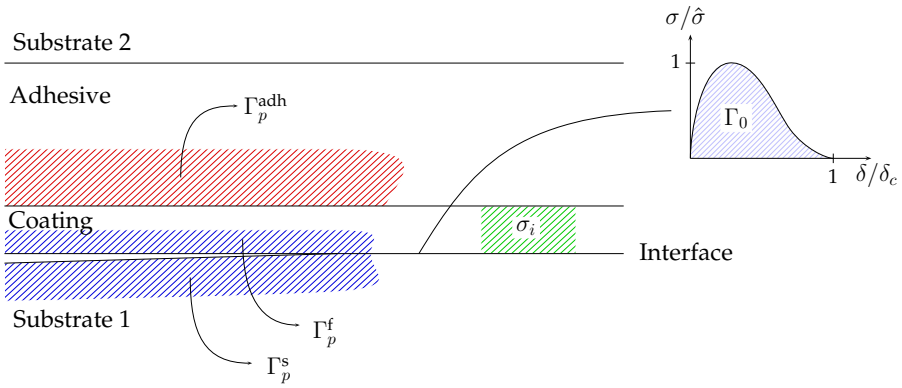

Figure 6.2: Different energy contributions entering the total dissipated energy crack propagation.

Γ_p^{upper} : the plastic dissipation in the upper substrate;

$\mathcal{G}(\zeta\sigma_i)$: the energetic contribution of the internal stress to the crack propagation, which might not fully relax depending on the problem (see further).

These energy contributions depend on the thickness of the coating and each of them has an influence on the measured interface toughness. The origin of each term and its influence on the adherence is addressed in this chapter in the context of copper films. This part of our work extends the theoretical analysis by Wei and Hutchinson [73] in the case of systems with an overlayer, in the frame of the wedge opening test.

Several contributions in the energy dissipation have to be distinguished.

• A first distinction has to be made regarding the energy dissipation between the intrinsic and extrinsic contributions, schematically represented in blue and red in Figure 6.2, respectively. The intrinsic energy dissipation is inherent to the system and will always be present when a crack propagates. The intrinsic contribution is, in our case, the sum of the work of adhesion and of energy associated to (visco)plasticity and possible viscoelastic dissipation in the substrate and the coating ($\Gamma^{\text{s}} + \Gamma^{\text{f}}$), as well as some elastic energy locked in the layers. This energy will always have to be spent in the system while the coating delaminates.

Now, this does not mean that all these terms are fully independent of the loading conditions. For instance, the amount of plastic dissipation in the film will depend on the film thickness. Even the work of adhesion could depend on the loading conditions.

The extrinsic energy contribution is specific to the testing method and the specimen preparation. It needs to be removed from the measured value. More precisely, the additional bonded plate adds two layers to the system: the adhesive layer and the upper substrate. The energy dissipated in these two layers is, in our case, the extrinsic contribution[1]. It does not play a role in the delamination of the coating during normal use of the system. The relative contribution of the terms Γ^{s}, Γ^{f} and Γ^{adh} in Eq. (6.2) has been studied using a finite element (FE) model simulating the wedge opening test. The model is described in section 6.5. Note that exactly the same difficulty associated to possible dissipation in the overlayers exists in the four-point bending test when applied to thin coatings.

• Another contribution to the total measured energy is coming from the initial stress present in the coating. The initial stress in the coating provides an additional contribution to the driving force that is already available in the system. For a film that fully relaxes during decohesion, the energy available for delamination is

$$\mathcal{G}(\sigma_i) = \int \frac{\sigma_i^2(t)}{2\bar{E}}\,\mathrm{d}t\ , \tag{6.3}$$

where σ_i is the stress in the coating and t its thickness [29,64]. Equation (6.3) is exact only if the stress in the coating is fully relaxed downstream of the crack tip. Due to the adhesive layer, the film is not freestanding after delamination and the stress cannot fully relax. The value of the term $\mathcal{G}(\zeta\sigma_i)$ in Eq. (6.2) is thus a fraction of the total energy potentially available (Eq. (6.3)). This fraction is computed using the fraction of the internal stress relaxed during crack propagation $\zeta\sigma_i$ in Eq. (6.3) (with $\zeta \in [0;1]$). A numerical study on an idealised FE model has also been performed to address this point, and is explained in section 6.5.

[1]The energy dissipated in the upper substrate will always be negligible. In the system of interest here, the extrinsic contribution reduces thus to the energy dissipated in the adhesive layer Γ^{adh}

The system of interest — on which the measurement method and data reduction scheme based on the separation of the different terms entering Eq. (6.2) are used — is a thin copper coating deposited on a stainless steel substrate. The copper coating has been chosen for this study in collaboration with the company ArcelorMittal. It is mainly used to give a metallic aspect to a non metal or to give a metal an aspect of copper (e.g. in the renovation of the roof of old buildings). One of the motivations for characterising the adhesion of Cu films was the observation that the adhesion seems to vary with the coating thickness, leading sometimes to spontaneous delamination for thick films (thicker than 3 μm) deposited under standard conditions. Copper films are easily deposited on a large number of materials (metal or not).

6.3 Materials and experimental method

This section describes the copper coating. The deposition process and the film microstructure are presented first, followed by an analysis of the internal stress in the coating.

6.3.1 Thin copper film deposition and microstructure

The copper coating is deposited by plasma magnetron sputtering under a low pressure of argon atmosphere. The substrate preparation is an important parameter influencing the interface between the substrate and the coating, hence the adhesion of the coating. The substrate is first cleaned in an ultrasonic bath with Methyl Acetate before being introduced in the deposition chamber. The purpose of this step is to clean the substrate surface of all impurities and grease. Just before deposition, the substrate is subjected to ionic etching to remove the residual oxide layer or other contaminants. The coating is then deposited at a pressure between 0.4 and 0.7 Pa.

The deposition has been performed on square 0.4 mm thick stainless steel substrates of 115×115 mm sideways. A high vacuum (less than 10^{-2} Pa) is attained in the deposition chamber before injecting argon gas to reach

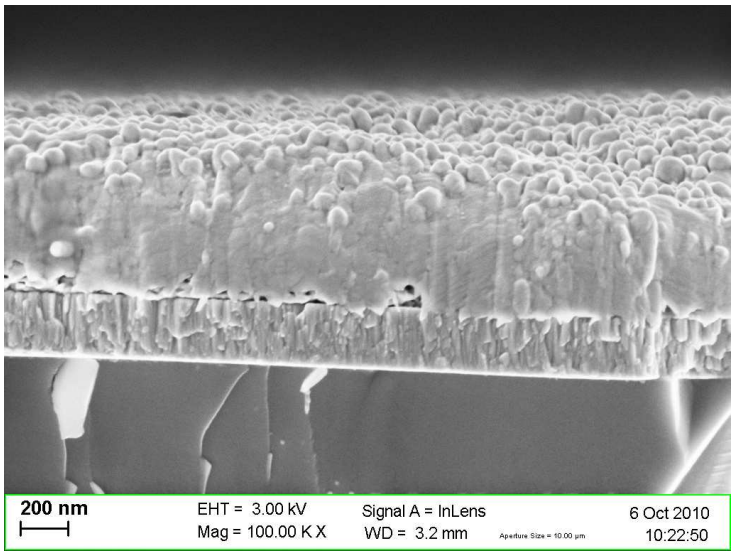

Figure 6.3: Micrograph of a side view of the coating. The substrate is made by silicon (bottom of the picture), on with an layer of 300 nm of stainless steel has been deposited (see Section 6.4) and the coating is deposited on top of this layer with a thickness of 1 µm. The columnar shape of the coating can be observed on this micrograph.

the deposition pressure. The generator used to induce the plasma is an Advanced Energy Pinnacle plus +10 kW. The target has a diameter of 150 mm and the distance with the substrate is 70 mm. The etching was performed using a pulsed DC current source at 1.5 A. The deposition was performed under DC current at an intensity of 0.5 A. The processing conditions of the different specimens are gathered in Table 6.1. The last two columns of the table show the grain size of the coating, and the ratio between the coating thickness and the grain size. The grains are supposed to present a columnar shape (see Fig. 6.3 for a micrograph of a 1 µm thick copper coating deposited on silicon, with a 300 nm thick stainless steel interlayer). The grain size has been measured on SEM micrographs (see Fig. 6.4) from a top view. The value given in Table 6.1 is an average approximate over 20 grains.

The wedge opening test and four-point bending tests require the bonding

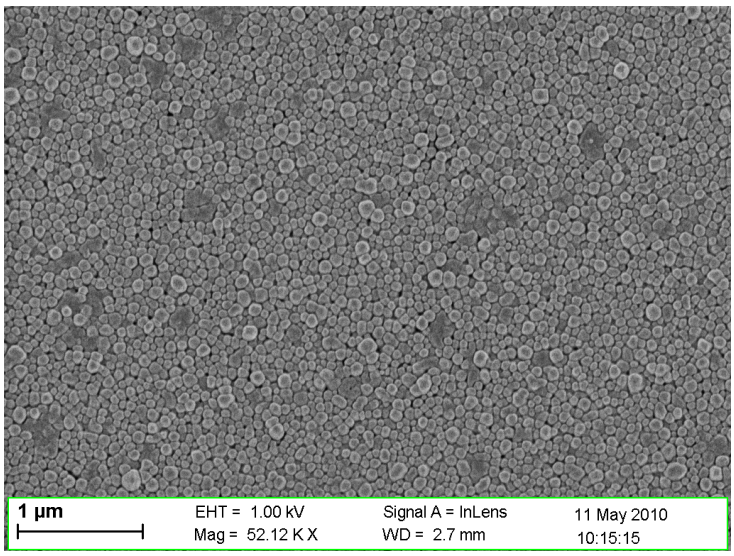

Figure 6.4: Typical micrograph used to measure the grain size.

Table 6.1: Properties and deposition parameters of the specimens. The last column shows the evolution of the ratio between the film thickness t and the grain size d.

thickness	deposition parameters			grain size d	t/d
[µm]	date	p [Pa]	duration	[µm]	[-]
0.5	02/09/2008	0.45	3 min 20 s	0.036	14.1
1	01/12/2008	0.47	6 min 40 s	0.066	15.2
1.5	15/10/2009	0.58	10 min 14 s	0.107	14.0
2	15/10/2009	0.62	13 min 39 s	0.085	23.5
2.5	15/10/2009	0.58	17 min 04 s	0.077	33.3

of an extra plate on top of the coating. This upper substrate (identical to the substrate) is bonded with a cyanoacrylate adhesive. The two surfaces are cleaned with norvanol[2]. The bonding of the adhesive on the upper substrate is artificially improved by increasing the roughness of the substrate surface.

6.3.2 Origin of the internal stress

The internal stress in a thin coating can have three main origins presented hereafter. This section is inspired from the lecture notes of Nix [51] and Francis et al. [19]. The specific origin of the stress in the copper coating will be discussed in the next section.

A thermally-induced internal stress appears when the **thermal expansion** coefficient α^{th} is different for the substrate and the coating. The stress results from the change in the temperature when the system cools down to room temperature after deposition. The reference temperature being the deposition temperature.

Knowing the thermal expansion of both materials, the stress can be computed as

$$\sigma_i^{\text{th}} = \bar{E}\Delta\alpha^{\text{th}}\Delta T \ , \tag{6.4}$$

where $\bar{E}$ is the biaxial modulus of the film $E/(1-\nu)$, $\Delta\alpha^{\text{th}}$ is the difference in the thermal expansion coefficients between the two materials and ΔT is the temperature variation.

An epitaxially-induced internal stress may appear when a thin crystalline film (a few nm) is deposited on a crystalline substrate at low deposition speed. In order to match the substrate lattice size l_s, the lattice of the film l_f has to be adapted. The interface can then be perfectly adjusted owing to deformation of the film, see Fig. 6.5.

In the case of an elastic deformation, the misfit strain of the film can be evaluated from the lattice parameters of the film and the substrate as

$$\varepsilon_{mf} = \frac{l_s - l_f}{l_f} \ . \tag{6.5}$$

[2] a combination of ethanol (83.5%), ether (2.5%) and water (14%).

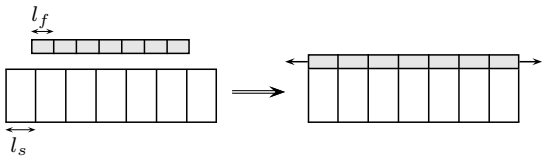

Figure 6.5: Origin of the epitaxial stress in a thin film.

The stress can be deduced from Eq. (6.5) using the elastic properties of the film.

Perfectly matching thin films can be deposited on a crystalline substrate only if the lattice parameter of the film is close to the lattice parameter of the substrate. If the difference is too high, dislocations will be generated to relax the stress in the film. These dislocations are called misfit dislocations. This happens when the energy needed to create a defect is lower than the stored elastic energy in the film. This occurs only if the deposition is made at low rate, allowing the system to remain in an equilibrium state. The strain energy per unit area of the film is

$$E_s = \bar{E}\left(\varepsilon_{mf} - \frac{b}{s}\right)^2 t \ , \tag{6.6}$$

where b is the length of the Burger vector and s is the distance between two dislocations. The dislocation energy per unit area is

$$E_d = \frac{2}{s}\,\frac{b^2}{4\pi(1-\nu)}\,\frac{2\mu_f\mu_s}{\mu_f+\mu_s}\ln\left(\frac{\beta t}{b}\right) \ , \tag{6.7}$$

where the μ are the different materials shear modulus and β is the dislocation core energy parameter which is usually fitted with experiments. Misfit dislocations form if it is energetically favourable, which means

$$\left.\frac{\partial E_{tot}}{\partial\left(\frac{b}{s}\right)}\right|_{\frac{b}{s}=0} < 0 \quad \text{or} \quad \frac{t_c}{\ln\left(\frac{\beta t_c}{b}\right)} = \frac{2\mu_f\mu_s}{\mu_f+\mu_s}\,\frac{b}{4\pi(1-\nu)\bar{E}\varepsilon_{mf}} \ , \tag{6.8}$$

where t_c is the critical thickness of the film at which dislocations are created [45].

Growth stress also called *intrinsic stress*, arises during the deposition process, due to microstructure evolution. The stress in the film may vary during the deposition process (see Fig. 6.6). Three different phases can be distinguished corresponding to the three numbers in figure 6.6.

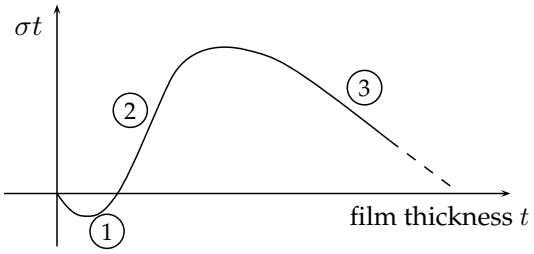

Figure 6.6: Typical behaviour of the growth stress as a function of the coating thickness during the deposition process. The mean stress of the coating is represented by the slope of the line linking the origin of the graph to the corresponding point on the curve.

1. At the beginning, the coating is deposited in the form of islands, also called crystallites. The islands are negatively stressed. This compression is due to the surface stress effects. The surface stress f_{ij} is the force per unit length of exposed edge applied to a terminating surface in order to keep it in equilibrium. The surface stress is related to the surface energy γ by the relationship

$$f = \gamma \frac{\partial \gamma}{\partial \varepsilon} + \gamma \tag{6.9}$$

2. The stress then rises due to crystallite coalescence (see Fig. 6.7). The stress increases and becomes tensile.

3. After the coalescence of the crystallites, the stress can be partially relaxed. If the atoms have enough energy to move at the boundary between two crystallites, the stress lowers and is finally relaxed in the upper part of the film thickness, see Fig. 6.8. Another source of stress relaxation is the formation of dislocations. The dislocations induce a compressive stress offsetting the tensile stress.

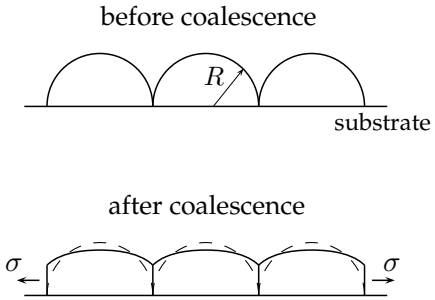

Figure 6.7: Schematic of crystallites coalescence and the induced stress.

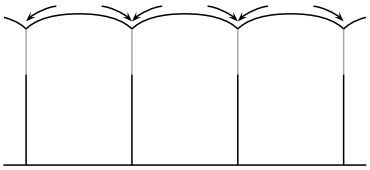

Figure 6.8: Schematic of boundary stress relaxation during crystallite growth.

Moreover, a tensile stress can develop when the *growth mechanism* does not allow the depositing atoms to attain their lowest energy position. Some model explained it by a constrained shrinkage of deposited material resulting in lattice parameters greater than normal [34]. The grain boundary model attributes the origin of the internal stress to the development of grain boundaries [35]. It has been proposed that the coalescence of lattice defects into microvoids cause the tensile stress. The mechanical properties of the grain material are important to the resulting stresses and impurity incorporation and reaction with the deposited film material can also be important factors in the stress generation.

The deposition pressure and the deposition technique have also an influence on the internal stress building up in the deposited film, as the morphology of the coating also affects the internal stress. A columnar coating generally involves a tensile internal stress and a compact coating morphology induces a compressive stress. Using the plasma sputtering deposition process, the pressure in the deposition chamber influences the morphology of the coating. Changing the pressure is also another way

to change the stress in the deposited film.

The presence of impurities in the chamber changes the way the stress develops. A study made on evaporated copper shows that an oxygen partial pressure of 10^{-7} mbar in the chamber makes the stress become tensile for a thickness of around 100 nm [2]. It is true that the evaporation process is much more sensitive to impurities than sputtering. But, before the depositions, the initial pressure in the deposition chamber is more than 10^{-6} mbar. Considering that there is around 20% of oxygen in the air, the partial pressure of oxygen is much higher than the values studied in [2]. It is also a criterion to take into account.

6.3.3 Internal stress measurement

The average internal stress of the coating (noted σ_i) has been determined using the Stoney method [32, 63]. The Stoney equation relates the curvature of a substrate to the stress in the coating as

$$\sigma_i = \frac{E_s t_s^2}{6\,(1-\nu_s)\,t_c}\,(C - C_0)\ . \tag{6.10}$$

The substrate and the coating thickness are noted t_s and t_c, respectively. The Young's modulus and Poisson ratio of the substrate writes E_s and ν_s, respectively. Stoney formula relies on the assumption that the film is much thinner than the substrate, see [63]. The curvature of the substrate is measured before and after the deposition of the coating, their value are named C_0 and C, respectively (see Fig. 6.9). Knowing these parameters and the properties of the substrate (E_s and ν_s), the stress is computed using Eq. (6.10).

The internal stress measurements are performed using silicon wafers ($E_s/(1-\nu_s) = 180$ GPa; $t_s = 380\,\mu$m) producing a well defined curvature C_0 needed to get high precision on the measurement. Only the wafers with a clean constant initial curvature are used to measure the coating stress. The curvature of the wafer is measured with a profilometer Veeco Dektak 150. A profile of the vertical displacement along the wafer diameter is measured, see an example in Fig. 6.9. An arc of circle is fitted to the data points using the least-squares method from which

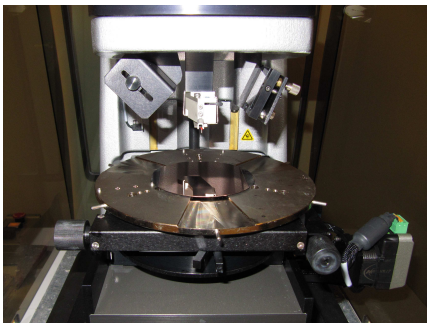

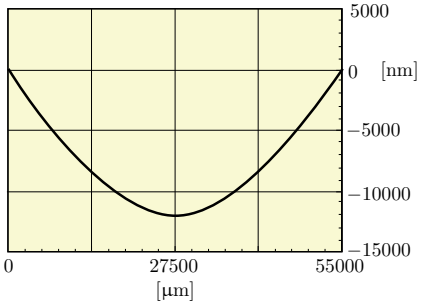

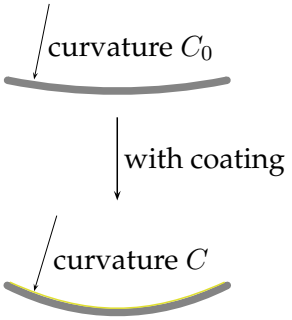

$$\sigma_i = \frac{E_s t_s^2}{6\,(1-\nu_s)\,t_c}\,(C - C_0)$$

Figure 6.9: Description of the measurement of the stress in the coating using the Stoney method. The profile (above right picture) is measured by the profilometer (above left picture). The difference in the curvature before and after the deposition of the coating (lower left picture) enters the equation to measure the stress (6.10).

the radius is extracted. The curvature is computed as $C = 1/R$ and the curvature sign is determined by looking at the measured profile. The profile picture in Fig. 6.9 has been taken on a 2 µm copper film. The corresponding stress is close to 180 MPa.

Different values of the Young's modulus of silicon can be used depending on the loading conditions and orientation of the specimen. Here, the condition are equibiaxial and there is no orientation effect. The value of the Young's modulus to be used in Eq. (6.10) is 180 GPa, see [26].

The following procedure has been chosen in the present study. The curvature of the wafer is measured before any deposition to get C_0. A

thin layer of stainless steel is then deposited on the wafer. The idea is to be as close as possible to the real system of copper deposited on stainless steel. The curvature of the wafer C_1 is measured the day after the deposition of the steel layer. The copper film is then deposited on the stainless steel layer and the final curvature C_2 is measured the day after the second deposition. Additional measurements have been made after a month to verify that internal stress does not relax. An etching of the surface is performed before any deposition. In order to take into account the possible change of the steel layer thickness and stress due to the etching, a wafer with a steel layer is etched without any further deposition and its curvature is also measured. The coating thicknesses are the same as reported in Table 6.1

The steps of the procedure are summarised as follows:

1. selection of the wafers with the most constant curvature;
2. measurement of the thickness of the wafer t_s;
3. measurement of the initial curvature C_0;
4. deposition of the steel interlayer[3];
5. measurement of the thickness of the layer and C_1;
6. deposition of the coating;
7. measurement of the thickness of the coating t_c;
8. measurement of the final curvature C;
9. evaluation of the stress using Eq. 6.10.

6.4 Experimental results

This section presents the internal stress measurements followed by the adhesion measurements with the wedge opening test. The discussion about these results and the comparison with the numerical simulation are made in Section 6.8.

[3]The steel interlayer is required to avoid that the substrate affects the stress of the coating.

6.4.1 Internal stress of the coating

The internal stress in the copper coatings has been measured using silicon wafers. For some wafers, a small stainless steel layer (300 nm thick) has been deposited before the copper film to be as close as possible to the real system.

Effect of the substrate

Figure 6.10 shows the variation of the internal stress with the film thickness for coatings deposited either directly on silicon or on the stainless steel interlayer. A difference in the stress value and in the grain size has been observed for the same copper coating, deposited directly on the silicon wafer or deposited on a small layer of stainless steel. The difference observed for the internal stress is larger than 100 MPa, see Fig. 6.10. Figure 6.11 compares the microstructure of the coatings with and without the steel interlayer. Figures 6.11(a) and (b) compare the 0.5 μm thick coatings. The coating with the steel interlayer is more uniform and the grains are significantly smaller. The two lower micrographs (micrographs c and d) compare the 1 μm thick coatings. The coating with the steel interlayer is again more uniform. Large aggregates can be observed on the coating without interlayer (Fig. 6.11(c)), which are much smaller in Fig. 6.11(d). The grain size for a copper film deposited directly on silicon is equal to 51 and 182 nm for a thickness of 0.5 and 1 μm, respectively. The values have to be compared to the values given in Table 6.1, i.e. 36 and 66 nm, respectively for a 0.5 and 1 μm copper film deposited on a stainless steel interlayer.

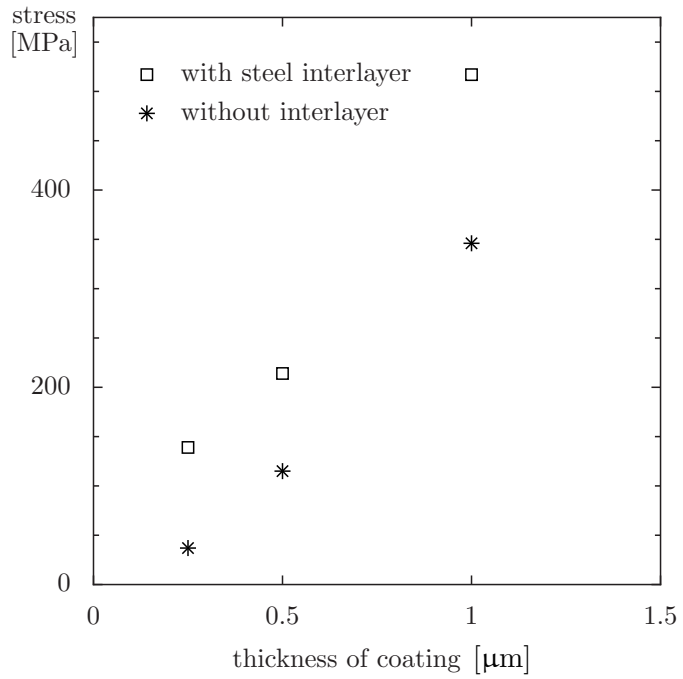

Figure 6.10: Comparison between the internal stress in a copper coating deposited directly on a silicon wafer (system Cu/Si: ✳) or on a thin stainless steel interlayer (system Cu/$Fe_{(300\,nm)}$/Si: □).

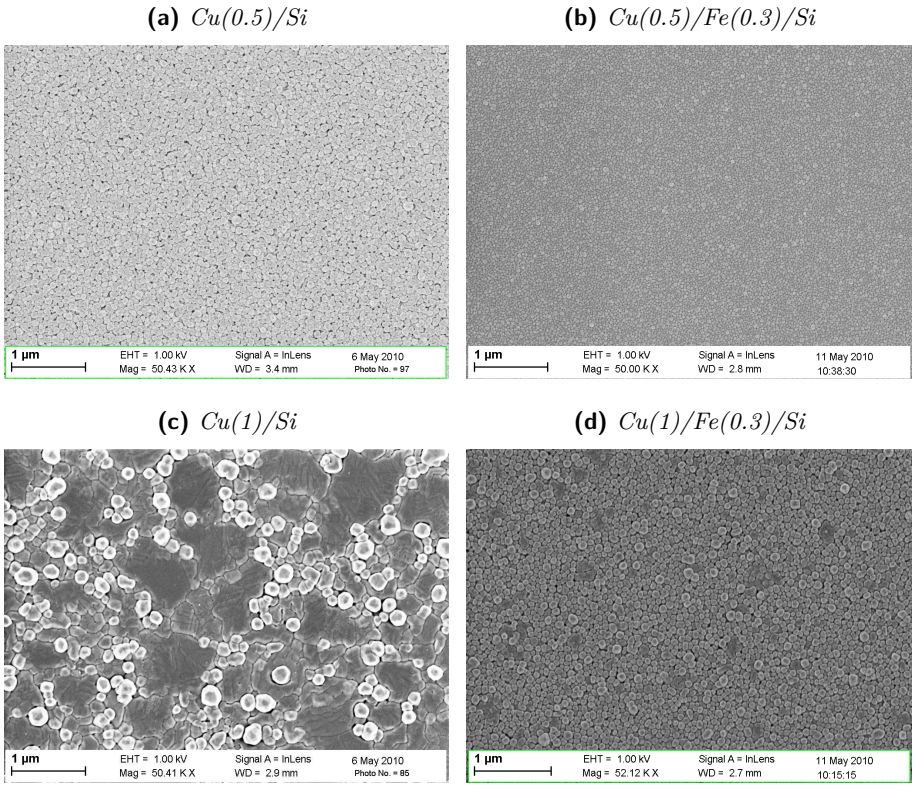

Figure 6.11: Micrographs of the copper coating deposited on silicon. The comparison is made between the system with a steel interlayer (b and d) and without the interlayer (a and c) for two copper film thicknesses (0.5 and 1 µm).

Effect of the thickness and dispersion among few batches

The following results address the system with the stainless steel interlayer only. The distinction is made between three distinct series of coatings. The main difference between these batches is the date of the deposition. The deposition process conditions are shown for each batch in Table 6.2. The evolution of the stress with respect to the coating thickness is represented in Figure 6.12 for the different batches. In each case, the stress raises linearly with the thickness until 1 µm and then remains constant. These results are discussed in the next section.

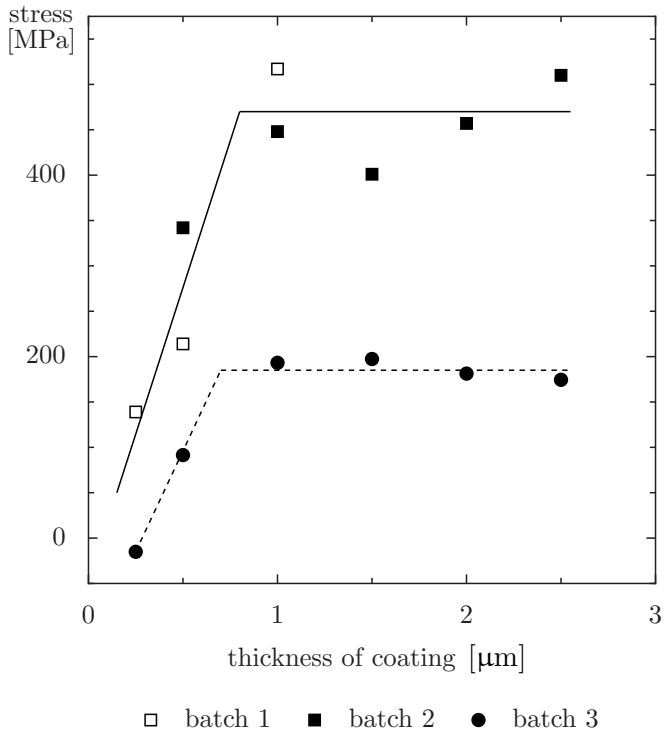

Figure 6.12: Variation of the stress in the coating as a function of the thickness. The coatings have been processed at different time in three distinct batches.

Table 6.2: Deposition conditions and internal stress of the different specimens. The different parts of the table correspond to different deposition series made at different dates, corresponding to the different series of results in Fig. 6.12. The last part corresponds to the coatings deposited directly on the silicon wafer.

thickness	deposition parameters			internal stress
[μm]	date	pressure [Pa]	duration	[MPa]
batch 1 : □				
0.25	31/03/2009	0.45	1 min 42 s	139
0.5	31/03/2009	0.45	3 min 20 s	214
1	31/03/2009	0.54	6 min 40 s	517
batch 2 : ■				
0.5	12/10/2009	0.65	3 min 20 s	342
1	12/10/2009	0.64	6 min 40 s	448
1.5	12/10/2009	0.67	10 min 14 s	401
2	12/10/2009	0.67	13 min 39 s	457
2.5	12/10/2009	0.67	17 min 04 s	510
batch 3 : ●				
0.25	22/12/2009	0.53	1 min 42 s	−15
0.5	22/12/2009	0.57	3 min 20 s	91
1	22/12/2009	0.57	6 min 40 s	193
1.5	22/12/2009	0.57	10 min 14 s	197
2	22/12/2009	0.53	13 min 39 s	181
2.5	22/12/2009	0.53	17 min 04 s	174
System without steel interlayer				
0.25	01/12/2008	0.47	1 min 42 s	37
0.5	18/09/2008	0.47	3 min 20 s	115
1	—	—	—	346

The stress measurement is made on a silicon wafer with the copper deposited on a small stainless steel interlayer. The stress raises linearly with the thickness until 1 µm *and remains nearly constant for thicker coatings.*

6.4.2 Origin of the internal stress in the copper films

The coatings studied in this thesis are deposited using a *cold* magnetron sputtering process. At the pressure used for deposition, the coatings have a columnar shape. This shape favours tensile internal stress. This is one possible origin of the internal stress in the studied coatings. But other reasons can be invoked.

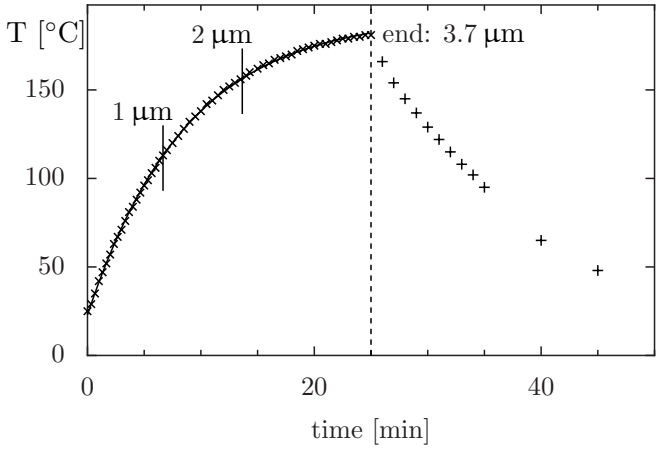

Figure 6.13: Evolution of the temperature during the deposition of a copper film measured at the back surface of the substrate, near the centre. After 25 min of deposition (dashed vertical line), the plasma has been shut down. The last point (after 45 min) has been recorded just before the opening of the deposition chamber. The deposition has been made under a pressure of 0.45 Pa and with a current intensity of 0.5 A.

The deposition process is said to be "cold" because the substrate is not heated. However, the temperature of the substrate raises up during the deposition due to the target atoms showering. The evolution of the temperature has been measured by fixing a thermocouple near the centre of

the substrate back surface. The results are shown in Fig. 6.13. The initial temperature of the substrate was 25 °C. The thickness of the coating increases linearly with the deposition time in the case of the copper coatings considered in this work. The evolution of the temperature during the deposition can then easily be expressed as a function of the coating thickness. In the case of copper coating, the thickness evolves linearly with the deposition time. The expression of the substrate temperature as a function of the coating thickness, fitted from the data on Fig. 6.13 is

$$T = 192 - 169\, e^{-0.75t} \ , \tag{6.11}$$

where the temperature is expressed in °C and the coating thickness is expressed in micrometers. The copper coating is deposited at a rate of 146.5 nm/min. The evolution of the stress in the copper film shown in Fig. 6.10 is compared with the thermal stress contribution in Fig. 6.14. The evolution of the thermal contribution to the internal stress is computed by inserting Eq. (6.11) in Eq. (6.4) while using $\alpha^{\text{th}}_{\text{Cu}} = 16.5\,10^{-6}\,\text{K}^{-1}$, $\alpha^{\text{th}}_{\text{Si}} = 2.3\,10^{-6}\,\text{K}^{-1}$ and $\bar{E}_{\text{Si}} = 180\,\text{GPa}$.

The α^{th} coefficient of Cu is higher than the α^{th} coefficient of the silicon by a factor of ten. The evolution of σ_i^{th} shows that the increase of the internal stress with the film thickness can be attributed to the thermal effect. Furthermore, the change of the temperature during deposition might also vary from one batch to another.

Growth stress and possible impurities affect also the internal stress of the film. A review of stress in thin metallic films [35] explain the influence of the presence of oxygen in the deposition chamber on evaporated copper films, see Fig. 6.15. This result is made for evaporated films but the general trend of the internal stress is the same for sputtered films. See [36] for a comparison between the two techniques.

A very small presence of oxygen in the deposition chamber leads to a variation of the internal stress from compressive to tensile. During the deposition of the coatings for this work, the residual air pressure in the chamber before the introduction of argon is between 10^{-2} and 10^{-3} Pa. Considering 20% of oxygen in air leads to a partial pressure of oxygen close to the upper curve of Fig. 6.15. This means tensile stress in the film.

Now, other contributions can also play a role. The epitaxial stress is generally taken into account only for very thin films (lower than 100 nm). The films considered in this work are much thicker. The lattice correspondence does not affect the stress but the substrate is affecting the stress, see Fig. 6.10. The way the substrate affects the stress is still to determine.

6.4.3 Yield strength

The mechanical properties of thin film materials vary with the film thickness, mainly due to grain size differences among different film thicknesses. This phenomenon is known under the general statement that *smaller is stronger*, see [20, 58]. The decrease of the thickness of the

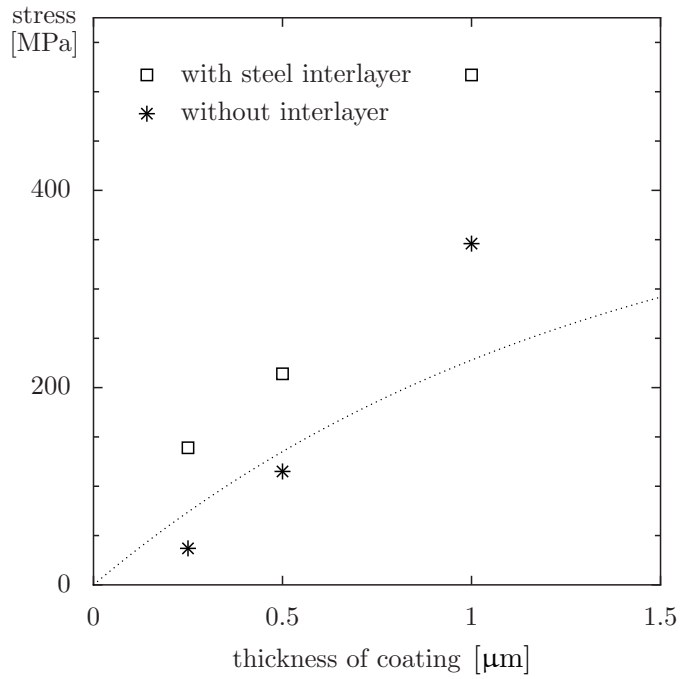

Figure 6.14: Evolution of the stress in the coating (same as Fig. 6.10) with the dotted line representing the evolution of the stress of thermal origin computed using Eq. (6.11).

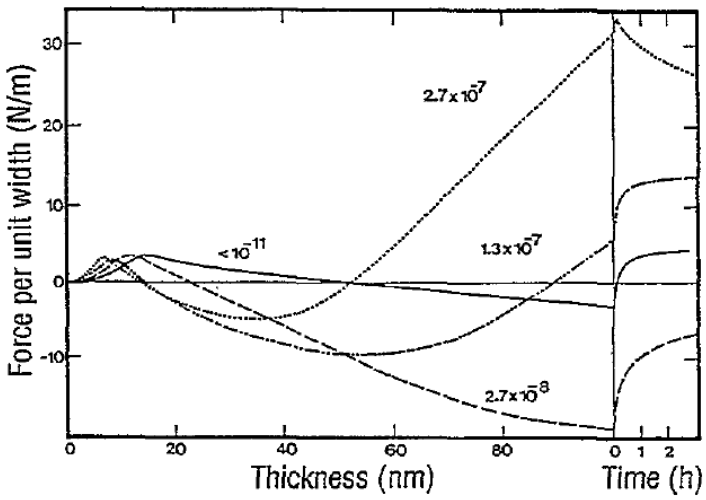

Figure 6.15: Variation of the internal stress of evaporated copper films at various O_2 partial pressures (taken from [35]).

film and of the grain size can increase the yield stress significantly. The determination of this variation requires specific techniques, which have not been used during this work. Nanoindentation is the easiest one. Some methods rely on thin film bending. Other techniques, more sophisticated, have been developed in the last decade using microelectronic processes, like the bulge test, the compression of micropillars, uniaxial tensile testing on freestanding films, or tensile testing made by a MEMS-based actuator. A review of these techniques can be found in [21, 58].

The mechanical properties of the deposited films have been obtained from the literature. Experiments have been indeed made on copper films with a thickness ranging between 0.3 and 3 µm in the group of Professor Vlassak at Harvard University [50, 76–78]. These measurements were performed using the bulge test method (see Section 3.4 on page 47 or [76] for more details). Experiments have also been made using micro-tensile test on a 1 µm thick copper film on a polyimide substrate for different grain size [25]. The results are reported in Fig. 6.16, showing a clear decrease of the strength with increasing film thickness. This effect is directly connected to the change of the grain size when varying the film

thickness.

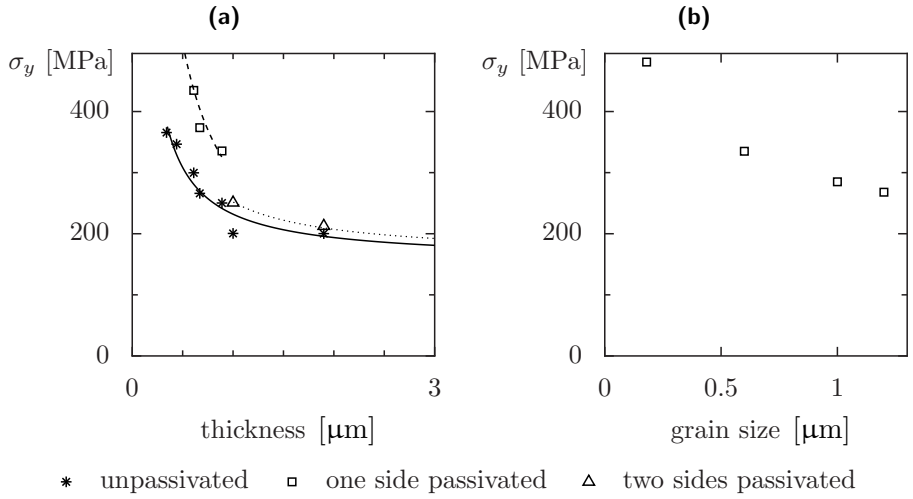

Figure 6.16: Variation of the yield strength of a film following the variation of its thickness (a) or the size of the grains (b). The experimental data are taken from [78] for (a) and from [25] for (b).

A polynomial fit has been performed on these experimental values as an indication of the strength that can be expected for our system. The deposition parameters and substrate are of course different. The microstructure is also different. The grain size in the study made by Vlassak is in the order of the film thickness, with a value of the ratio t/d between 1.06 and 1.93 for the sputtered films. The value of this ratio is in our case around 15 for the film thicknesses under 2 μm and increases to 33 for the thicker film, see Table 6.1. The grain size of the films used in this study is typically ten times smaller than the one studied in the literature. Hence, there is no guarantee that the values apply to our copper films, but they provide the best available estimation. The FE computations have been performed using values extrapolated from these results [77, 78].

Link with the internal stress in the film

Internal stress plays also a role in the determination of the yield strength of the film. Indeed, if the internal stress of the film σ_i is higher than the yield strength of the film σ_y, the value of the yield strength raises so that

$$\sigma_y = \sigma_i \ . \tag{6.12}$$

The stress state in the film is equibiaxial with $\sigma_{11} = \sigma_{22} = \sigma_i$ and $\sigma_{33} = 0$. If plasticity takes place when the Von Mises stress is equal to the yield strength then

$$\sigma_e = \sigma_y \quad \Longleftrightarrow \quad \sigma_i = \sigma_y \tag{6.13}$$

because here

$$\sigma_e = \sqrt{\frac{1}{2}\sigma_{11}^2 + \frac{1}{2}\sigma_{22}^2} = \sigma_i \ . \tag{6.14}$$

This leads us to four different possibilities for determining the yield strength of the film. Two extreme cases are possible for the internal stress in the film coming from the variations from batches to batches (see Fig. 6.12) and two cases considered in this work for the evolution of the yield strength coming from the literature (see in 6.16(a) the curve for a film unpassivated and for a film passivated on one side). The fitted analytical evolution of the yield strength with the thickness is

$$\sigma_y = 178.5 + \frac{67}{h} \ , \tag{6.15}$$

for an unpassivated film and

$$\sigma_y = 84.5 + \frac{214}{h} \ , \tag{6.16}$$

for a one side passivated film, with thickness h in micrometer and the corresponding stress σ_y in MPa.

The four possible evolutions of the yield strength in the film are shown in Fig. 6.17(b) for an unpassivated film and in Fig. 6.17(c) for a film passivated on one side. These four possibilities will be used in the FE simulations developed in Section 6.8. In principle, the present problem is closer to the “one side passivated” configuration as we do not expect much confinement of the plasticity due to the adhesive layer.

(a) *Superposition of Figures 6.16(a) and 6.12, linking the yield strength of the film σ_y to the internal stress σ_i.*

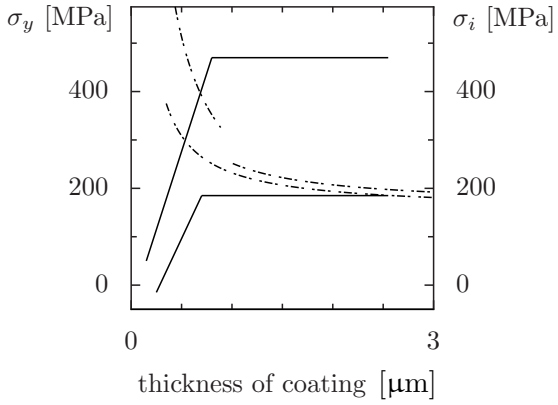

evolutions of σ_y depending on the passivation

different possible evolutions of σ_i from Fig. 6.12

(b) *Evolution of the yield strength of the film with the thickness if unpassivated.*

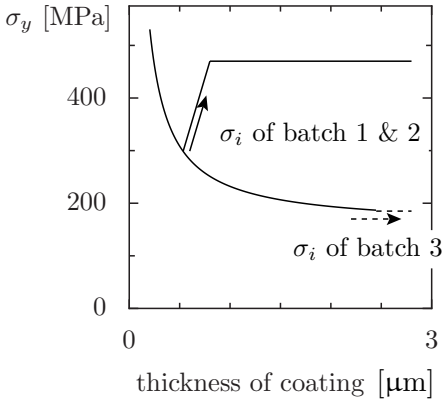

(c) *Evolution of the yield strength of the film with the thickness if passivated on one side.*

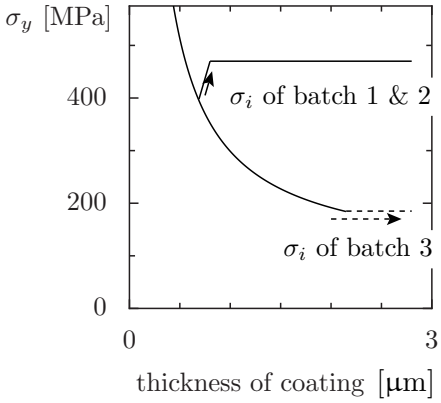

Figure 6.17: Comparison between the evolution of the yield strength of the film with the thickness observed by the group of Vlassak and the internal stress of the film. Two different cases are considered in the comparison, depending on the evolution of the internal stress as shown in Fig. 6.12.

6.4.4 Interface toughness

The results of the wedge opening test measurements for the different coating thicknesses are shown in Fig. 6.18. The error bars show the maximum and minimum values measured with the wedge opening test, from a large number of specimens, as documented in Table 6.3.

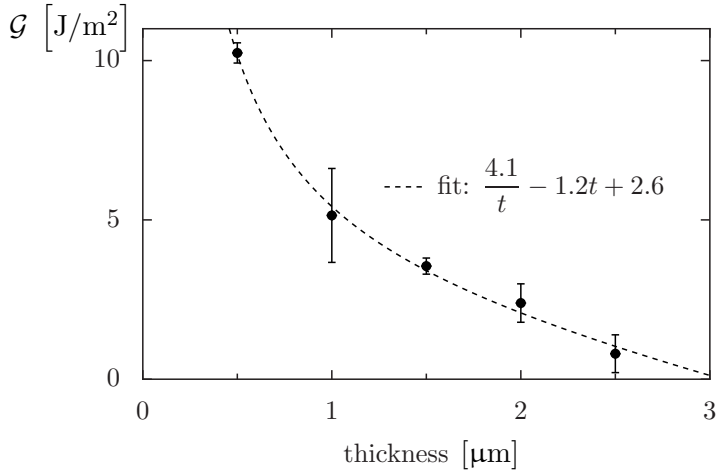

Figure 6.18: Variation of the measured interface toughness as a function of the coating thickness. The points represent the mean value of the measurements on each thickness with the standard deviation shown with the error bars. The number of different measurements made for each film thickness is given in Table 6.3.

The interface toughness significantly decreases with increasing thickness. The wedge opening test is a measure of the total energy release rate associated to the external loading. It includes the dissipation in all the layers of the specimen, i.e. involving the layers not included in the "intrinsic" system, which is the thin copper coating on steel. The internal stress in the coating is also playing a role. As will come out from the modelling later in the chapter, the value of these contributions are not negligible and significantly vary when changing the coating thickness.

A typical set of adhesion measurements is shown in Fig. 6.19. All the measurements made on three different specimens are represented, including involving non valid points, see further. As said earlier, the

Table 6.3: Experimental data of the points in Fig. 6.18. The standard deviation and the number of points taken into account are given for each coating thickness t.

name	t	$\mathcal{G}$	std dev.	nr pts	deposition parameters			meas. dates
	[µm]	[J/m^2]	[-]		name	date	p [Pa]	
Cu500_0801	0.5	10.2	0.32	14	BA080906	02/09/08	0.45	25/09 – 06/10/08
Cu1000_0801	1	5.7	0.91	14	BA081201	01/12/08	0.47	18/12 – 07/01/09
Cu1000_0902	1	4.3	1.75	10	BA090104	14/01/09	0.48	30/01 – 20/02/09
Cu1000 : all	1	5.1	1.48	24	BA081201	01/12/08	0.47	18/12 – 07/01/09
Cu1500_0902	1.5	3.6	0.25	12	BA091038	15/10/09	0.58	22/01 – 03/02/09
Cu2000_0902	2	2.4	0.60	4	BA091041	15/10/09	0.62	12/11 – 30/11/09
Cu2500_0902	2.5	0.8	0.60	12	BA091036	15/10/09	0.58	27/10 – 18/11/09

interface selected for decohesion is not controlled (see Section 4.3). The propagation is mainly occurring at the interface between the substrate and the coating, which is the weakest interface, but sometimes, the crack can jump to another interface. It is only after the entire decohesion of the specimen and the analysis of the interface that the measurements can be validated. A typical photograph of a specimen in Fig. 6.19 clearly shows that the interface has to be analysed to validate the measurement. The second set of measurements made on this specimen has produced a value of the energy release rate higher than the two others but the anal-

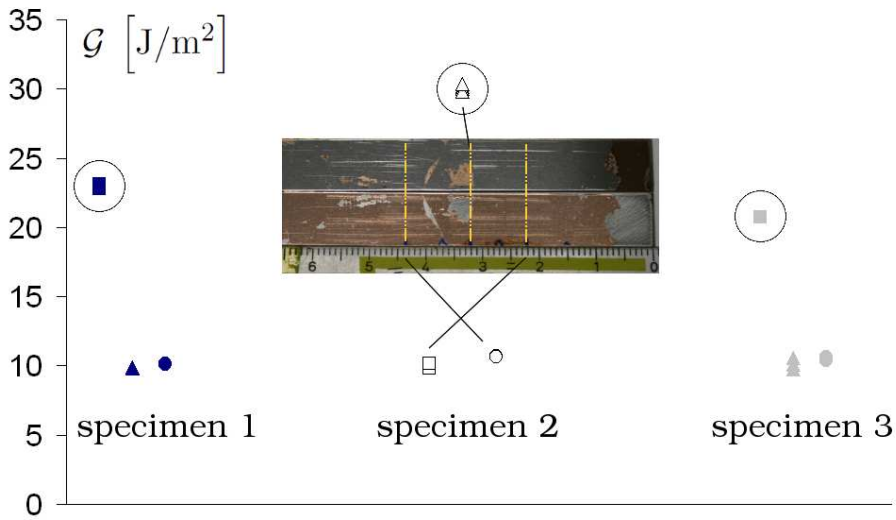

Figure 6.19: Set of measurements taken on three different specimens and at different locations in each specimens with several repetitions at fixed wedge. A picture of specimen 2 is inserted with the location of the crack tip corresponding to each set of measurement indicated by the vertical dash-dot lines (the wedge is inserted in the specimen from the right of the image). The second measurement set has been taken with the crack tip located at another interface than the interface of interest, explaining the difference in the energy with respect the other two locations on this specimen (see encircled data). Similar phenomena occur on the other two specimens. The horizontal scratches on the specimen are caused by the progression of the wedge through the specimen.

ysis of the surface reveals that the decohesion did not occur in the right interface for these measurements. These points are then not taken into account. Figure 6.19 shows also that similar phenomena take place for specimens 1 and 3. The excluded points are encircled. Figure 6.19 shows also that the variability between measurements at the different locations on one specimen and the variability among the different specimens, are small.

6.4.5 Empirical tests

Some measurements using the empirical methods (tape test, cross cut and bending) have been also performed on the same coatings. The results are shown in Table 6.4. Different coatings have been tested for some of the thicknesses. The lines in the table separate the different specimen.

The different tests performed are: (i) the tape test, a piece of tape is pressed on the surface and then removed; (ii) the cross cut test, cuts in two different directions are made with a cutter on the coating, a piece of tape is pressed on it and then removed and (iii) the bending test, the substrate is bended around a cylinder of radius 3 mm, a tape is then pressed on the curved surface and then removed.
After performing each test, a visual analysis of the surface is made to determine if the coating has been removed or not. During the bending test performed on the 1.5 µm thick coating, the coating delaminates spontaneously after the bending of the substrate but remain continuous. For the thicknesses of 2 and 2.5 µm, the coating was completely ruined by the bending of the substrate.

The numerical values of the energy release rate measured with the wedge opening test and corresponding to each layer thickness in Table 6.4 is

t [µm]	0.5	1	1.5	2	2.5
$\mathcal{G}$ $\left[\mathrm{J/m^2}\right]$	10.24	5.14	3.55	2.39	0.80

Different observations can be made regarding these results.

Table 6.4: Results of the qualitative adhesion tests performed on copper coatings.

thickness [µm]	deposition date	p [Pa]	tape test	cross cut $r = 3\,\mathrm{mm}$	bending test
0.25	march 09	0.46	OK [a]	OK [a]	OK [a]
	march 09	0.48	OK [a]	OK [a]	OK [a]
	march 09	0.48			OK [a]
	july 09	0.47	OK [a]	OK [a]	KO [b]
0.5	march 09	0.46	OK [a]	OK [a]	KO [b]
	march 09	0.47	OK [a]	OK [a]	KO [b]
	july 09	0.46	OK [a]	KO [a,b]	KO [b]
	oct. 09	0.62	KO [a]	KO [b]	KO [b]
1	dec. 08	0.62	OK [a,b]		
	jan. 09	0.47	KO [a,b]		
	march 09	0.51	KO [b]		
	march 09	0.48	KO [b]		
	oct. 09	0.48	KO [a]	KO [b]	KO [b]
1.5	oct. 09	0.58	OK [b] KO [a]	KO [b]	KO directly
2	oct. 09	0.62	OK [a]	KO [a]	cracks directly
2.5	aug. 09	0.48	OK [a]	KO [a]	cracks directly
	oct. 09	0.58	KO [b]		

a) using a tape with a peel force of 7.5 Nm on stainless steel
b) using a tape with a peel force of 2.3 Nm on stainless steel

1. The first observation is that the tests are consistent. If the coating does not delaminate with the bending test, it does not delaminate with the simple tape test, and reversely. There are some exceptions perhaps due to differences in the way the tape has been pressed on the substrate or removed.

2. The evolution of the adhesion with the coating thickness is similar to the quantitative values. The adhesion decreases while the coating thickness increases.

3. Most of the coatings have been deposited at a pressure around 0.47 Pa. The objective was to produce all the coatings in the same conditions but for some of them, the pressure was a bit higher. These coatings tend to be less adherent with respect to the qualitative tests. No further investigations has been performed to study this influence.

6.5 Numerical modelling – separation of the different energy contributions

This section describes the numerical model used to simulate the wedge opening test and separate the contribution of each term of Eq. (6.2) on page 97. It is a steady-state two-dimensional finite-element model based on the formulation by Dean and Hutchinson [15] (see for example [17, 39, 56] for full description).

6.5.1 Model

The generic model for the wedge opening test is shown in Fig. 6.20. It is loaded through a displacement applied such as to mimic the effect of a wedge. It involves several layers of materials with an elastic or elastoplastic behaviour. The crack propagates along one interface which is described by a traction separation law, see further.

The model is implemented via a 2D plane-strain, steady-state, finite element formulation. Plane strain conditions are assumed as the width of

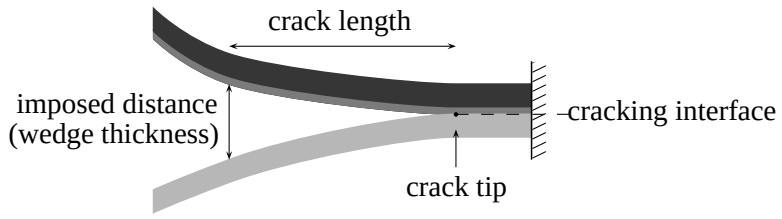

Figure 6.20: Generic model of the wedge opening test used in the numerical simulation (with three different layers).

the specimen is much larger than its thickness t. Any three-dimensional effects such as anticlastic bending are neglected[4]. The crack is assumed to have propagated for a sufficient distance such that steady state conditions prevail for the entire structure.

Steady-state formulation

The model assumes a semi-infinite crack propagating at constant velocity $\dot{a}$ [5]. Far from the crack tip, Mode I stress and displacement fields are applied. Assuming that the crack is growing in the x direction (see Fig. 6.1 on page 97), any rate quantity can be related to the x spatial derivative through the crack velocity. For example, the plastic strain rates are given by

$$\dot{\varepsilon}^{\mathrm{p}}_{ij} = -\dot{a}\frac{\partial \varepsilon^{\mathrm{p}}_{ij}}{\partial x} \ , \tag{6.17}$$

and any other quantity can be substituted for $\varepsilon^{\mathrm{p}}_{ij}$ with equal validity. The iterative finite element solution procedure used to solve the steady-state problem is the same as originally proposed by Dean and Hutchinson [15]. The virtual work statement for the quasi-static steady-state problem is

$$\int_V \delta_{ij} C_{ijkl} \varepsilon_{kl} \, \mathrm{d}V = \int_S \delta u_i T_i \, \mathrm{d}S + \int_V \delta_{ij} C_{ijkl} \varepsilon^{\mathrm{p}}_{kl} \, \mathrm{d}V \ , \tag{6.18}$$

[4] This hypothesis has been validated experimentally on some specimens.

[5] In this work, the specimen material response has been considered rate independent. The value of the velocity does not influence the result and the parameter has been set to 1.

where S is the boundary of the volume V, u_i are the displacements, ε_{ij} is the infinitesimal strain tensor, C_{ijkl} is the matrix of isotropic elastic stiffness, T_i is the traction acting on the boundary and $\varepsilon^{\mathrm{p}}_{kl}$ are the plastic strains. Given a solution for the displacement field, the plastic strains can be obtained by integrating the plasticity law along streamlines. The new distribution of plastic strains is then integrated as a body force in the second term of the right-hand side of Eq. (6.18) and a new solution for the displacement field is computed.

The FE method is based on finding an equilibrium solution for the displacement based on a previous approximate distribution of plastic strains and then integrating the plasticity law along streamlines to determine new approximations for stresses and plastic strains. This procedure is then repeated until convergence is achieved. The convergence criterion is that the squared norm of the difference vector between the degrees of freedom of the current and the previous iterations must be lower than a given tolerance. More details about the numerical procedure and the code can be found in [44].

Constitutive models

The local fracture process at the interface is represented by a traction separation condition across the crack plane. This condition is modelled by a layer of cohesive elements with zero thicknesses. The parameters of the cohesive zone are the interface strength $\hat{\sigma}$, the interface toughness Γ_0 and the interface critical opening[6] δ_c at complete separation, see Fig. 6.21. The normal and tangential components of the traction vector at the interface are noted T^{n} and T^{t}, respectively and the displacement are u^{n} and u^{t}. The form adopted for the cohesive zone was initially used by Needleman [49] and generalized by Tvergaard [69]. The cohesive response is gradually degraded using a decohesion indicator d as damage parameter. The value of this indicator is initially $d = 0$ for the interface in perfect adhesion and evolves to $d = 1$ for the completely de-bonded state. In the Tvergaard model, the decohesion parameter is given as the

[6] The critical opening in the normal and tangential directions are noted δ_c^{n} and δ_c^{t}, respectively.

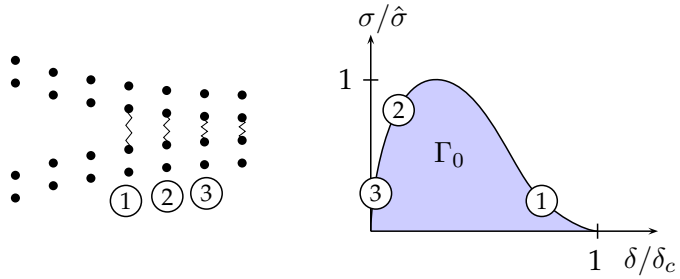

Figure 6.21: Traction separation law of the cohesive zone model.

maximum value of the displacement norm, so that

$$d = \max_{\tau<t} \sqrt{\langle v^{\mathrm{n}} \rangle^2 + v^{\mathrm{t}\,2}} \ , \tag{6.19}$$

where $v^{\mathrm{n}} = u^{\mathrm{n}}/\delta_c^{\mathrm{n}}$ and $v^{\mathrm{t}} = u^{\mathrm{t}}/\delta_c^{\mathrm{t}}$ are the normalized displacement. The brackets $\langle\,\rangle$ indicate specifically that a negative normal displacement does not play a role in the decohesion. The interface damage models considers the relations between tractions and displacements to be

$$T^{\mathrm{n}} = Ef(d)v^{\mathrm{n}} \ , \tag{6.20a}$$

$$T^{\mathrm{t}} = Gf(d)v^{\mathrm{t}} \ , \tag{6.20b}$$

where $f(d)$ is a monotonically decreasing function of d, E and G are the initial stiffness of the interface. A function $f(d)$ has been proposed by Tvergaard [69] which is

$$f(d) = (1-d)^2 \ . \tag{6.21}$$

The expression of the initial stiffnesses are

$$\begin{cases} E = 27\hat{\sigma}/4 \\ G = 27\hat{\tau}/4 \ . \end{cases} \tag{6.22}$$

The strength of the interface in tension is noted $\hat{\sigma}$ (see Fig. 6.21) and $\hat{\tau}$ is the strength of the interface in shear. These two parameters are part of the input data in the simulation.

The different layers of the system are modelled using isotropic elastic-plastic, rate independent J_2 flow theory with uniaxial tension behaviour given by

$$\sigma = \begin{cases} E\varepsilon & \text{for } \sigma \leqslant \sigma_y \\ \dfrac{\sigma_y}{(\sigma_y/E)^n}\,\varepsilon^n & \text{for } \sigma > \sigma_y \end{cases} , \tag{6.23}$$

where n is the strain hardening exponent.

The total fracture energy of the interface is evaluated in the model as the sum of the energy Γ_0 required to break the cohesive elements and the energy expended in the other layers, using Eq. (6.2). The way to extract the different energy values from the computation results is explained later in the section.

Two different models systems were addressed. The first system is the real specimen with the different layers as shown in Fig. 6.2. This system is used to extract the contributions of each layer of the specimen to the measured energy release rate. The details about the formulation and the study of some parameters are shown in Section 6.7 while the comparison with the experimental data is shown in Section 6.8. The second is a symmetric system with a substrate and the coating. This idealized system has been used to study the influence of different parameters: the internal stress of the film, the elastic limit of the film and the thickness of the film. These simulations have been computed with and without the existence of an adhesive layer between the coating and the substrate. The results of this study are shown in Section 6.6.

6.6 Idealized system

An idealized symmetric model has been first addressed in order to investigate from a general perspective the influence of the internal stress on the crack propagation induced by the wedge opening test.

6.6.1 Description of the model

The geometry of the domain is shown in Fig. 6.22. Symmetry conditions are applied along the mid plane and only one half of the domain has

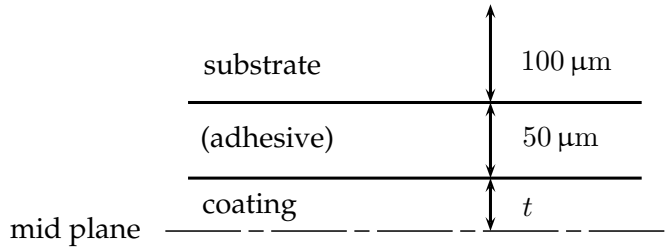

Figure 6.22: Schematic drawing of the idealised geometry used to study the influence of the internal stress on the interface crack resistance. The domain is symmetric and only one half of the system has been modelled.

been used in the simulation. The FE mesh of this domain is shown in Fig. 6.23.

The variables used in the model are detailed in Table 6.5. The variables are separated in different categories: fracture parameters describing the cohesive zone response; elastic parameters; parameters for the plastic response and the dimensions.

Table 6.5: Variables of the model.

CZM	$\hat{\sigma}, \Gamma_0$
Elasticity	σ_i^{f} $E^{\mathrm{s}}, E^{\mathrm{f}}, E^{\mathrm{adh}}$ $\nu^{\mathrm{s}}, \nu^{\mathrm{f}}, \nu^{\mathrm{adh}}$
Plasticity	$\sigma_0^{\mathrm{s}}, \sigma_0^{\mathrm{f}}, \sigma_0^{\mathrm{adh}}$ $n^{\mathrm{s}}, n^{\mathrm{f}}, n^{\mathrm{adh}}$
Dimensions	$D, t^{\mathrm{s}}, t^{\mathrm{f}}, t^{\mathrm{adh}}$

Dimensional analysis shows that the interface toughness is function of

the following parameters

$$\frac{\mathcal{G}_c}{\Gamma_0} = F\left(\frac{\Gamma_0}{\sigma_0^{\mathrm{f}} t^{\mathrm{f}}}, \frac{\hat{\sigma}}{\sigma_0^{\mathrm{f}}}, \frac{\sigma_0^{\mathrm{s}}}{E^{\mathrm{s}}}, \frac{\sigma_0^{\mathrm{f}}}{E^{\mathrm{f}}}, \frac{\sigma_0^{\mathrm{adh}}}{E^{\mathrm{adh}}}, \frac{\sigma_0^{\mathrm{f}}}{\sigma_0^{\mathrm{adh}}}, \frac{\sigma_0^{\mathrm{f}}}{\sigma_0^{\mathrm{s}}}, \frac{\sigma_i^{\mathrm{f}}}{\sigma_0^{\mathrm{f}}}, \right.$$
$$\left. n^{\mathrm{s}}, n^{\mathrm{f}}, n^{\mathrm{adh}}, \nu^{\mathrm{s}}, \nu^{\mathrm{f}}, \nu^{\mathrm{adh}}, \frac{D}{t^{\mathrm{s}}}, \frac{t^{\mathrm{f}}}{t^{\mathrm{s}}}, \frac{t^{\mathrm{f}}}{t^{\mathrm{adh}}}\right) . \quad (6.24)$$

The range of properties chosen for the parametric analysis has been selected such as to bound the problem of interest in this study. The parameters of the cohesive zone characterising the interface (see Fig. 6.21) are $\hat{\sigma} = 2\,\mathrm{GPa}$ and $\Gamma_0 = 1.34\,\mathrm{J/m^2}$. The values of the parameter describing each layer are listed in Table 6.6. The values of the strain hardening exponent n and of the Poisson ratio ν have been kept constant.

Table 6.6: Mechanical properties of the layers modeled in the idealised system.

	coating	adhesive	substrate
Young's Modulus [GPa]	100	3	200
Yield strength[7] [MPa]	$500/\infty$	30	200
Thickness [μm]	0.5/1/10	50	100
Internal stress [MPa]	$0 \rightarrow 550$	0	0
Strain hardening exponent [-]	0.1	0.05	0.1
Poisson ratio [-]	0.3	0.45	0.3

The non dimensional values of the parameters of Table 6.6 are:

- $\frac{\sigma_0^{\mathrm{f}}}{E^{\mathrm{f}}} = 2.5\,10^{-3}$ to ∞;
- $\frac{t^{\mathrm{f}}}{t^{\mathrm{s}}} = 2.5\,10^{-3}$ to $5\,10^{-2}$;
- $\frac{\sigma_i^{\mathrm{f}}}{\sigma_0^{\mathrm{f}}} = 0$ to 1.1.

[7] In thin films, the yield strength varies with the thickness. Nevertheless, in order to compare more easily the different results, the yield strength has been kept independent of the thickness.

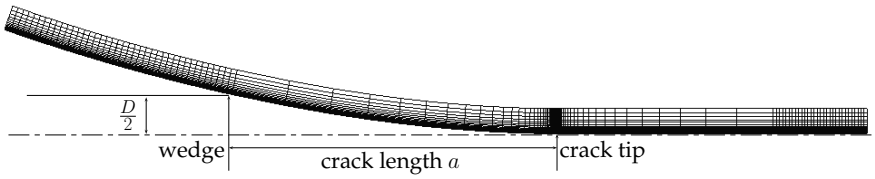

Figure 6.23: Mesh of the domain used in the simulation of the idealised model. The drawing is not to scale.

FE mesh

The domain of computation has been meshed using rectangular elements, see Fig. 6.23. The mesh is highly refined close to the crack tip in order to properly capture the fracture process. The two elements on both sides of the crack tip are squares of a few nm size. The size of elements is then regularly expanding as the distance from the crack tip increases. The expansion factor is the same in both directions, horizontally and vertically.

A special attention has been put on the convergence of the results in terms of mesh refinement. Different computations have been performed using the same input parameters with the mesh size being increasingly refined near the crack tip. When no significant change is observed anymore, the mesh is considered to be refined enough. The value of the smallest element, at the crack tip, is typically equal to 1 nm. This value has then been held constant for all the simulations. The size of the elements increases then regularly when moving away from the crack tip, the limit being a maximum aspect ratio of 1000. The code is allowing such aspect ratio without difficulty.

6.6.2 Layer by layer computation of the energy contributions

Simulations have been run for the different coating thicknesses and compared to the experimental results. Even though the system is quite different, it is performed in order to examine the variation of the parameters.

The terms appearing at the right hand of expression (6.2) on page 97 are not directly provided by the code which delivers the total work of each layer and the stress state only. We explain here how each term is determined and the underlying assumptions. The superscript on the parameters indicates the layer to which the parameter refers. As the procedure to extract the different energies is the same for each layer, only one general superscript L will be used in the following explanation.

The subscripts mean the following:

TOT: total work expended in a layer;

p: plastic dissipation in a layer;

el: elastic energy stored in a layer (which is not relaxed).

The subscripts *up* and *down* represent respectively an upstream section and a downstream section of the specimen. The upstream section is taken on an undeformed section far in front of the crack tip and the downstream section is taken after the wedge where the specimen is fully unloaded and no more energy is spent.

The extraction of each term appearing at the right hand of Eq. (6.2) is explained now:

The term Γ_0 is the thermodynamic work of adhesion of the interface. It is related to the parameters $\hat{\sigma}$ and δ_c given as input in the model. A simplified model of the cohesive zone (trilinear model [39]) gives

$$\Gamma_0 = 0.675\hat{\sigma}\delta_c \ . \tag{6.25}$$

The term Γ_{el}^L is the elastic energy stored in the layer. It is computed from the stress in the layer σ_L, either upstream or downstream, by

$$\Gamma_{el}^L = \int_0^t \frac{\sigma_L^2}{2\bar{E}} \, \mathrm{d}t \ . \tag{6.26}$$

The term Γ_p^L is the plastic dissipation in the layer. It is computed by subtracting the elastic energy to the total energy as

$$\Gamma_p^L = \Gamma_{TOT}^L - \Gamma_{el}^L \ . \tag{6.27}$$

The term $\mathcal{G}(\zeta\sigma_i)$ is the contribution of the internal stress of the coating to the delamination. It is computed by taking the difference between the stress in the coating before (upstream) and after crack propagation (downstream). The locked in elastic energy induced by the crack propagation itself is considered independent of the initial stress in the film and is taken as equal to the stress in the film while $\sigma_i = 0$. The term $\mathcal{G}(\zeta\sigma_i)$ is calculated as

$$\mathcal{G}(\zeta\sigma_i) = \int_0^t \frac{\left(\sigma|_{up} - \left(\sigma|_{down} - \sigma|_{\sigma_i=0}\right)\right)^2}{2\bar{E}} \,\mathrm{d}t \ . \tag{6.28}$$

6.6.3 Parametric study on the idealised system

The results of the FE simulations on the idealised model are shown in this section, starting with the dissipation in the adhesive layer for different layer thicknesses, see Table 6.6. Then, the relaxation of the internal stress during the propagation of the crack is addressed in the presence or not of the adhesive layer and for different yield strengths. The complete results are gathered in Tables D.2 and D.1 of Appendix D on page 197.

The base system used for this study, shown in Fig. 6.22, includes the adhesive layer with properties given in Table 6.6 on top of a film with a yield strength equal to 500 MPa. The film thicknesses and internal stresses are given in Table 6.6. The results of the simulations are represented with the continuous lines with different symbols to identify the three film thicknesses (0.5, 1 and 10 µm). Two variations from this base system have been considered independently: no adhesive layer (represented with the dashed lines in the figures) or a film with an infinite yield strength (represented with the dash-dot lines in the figures), i.e. an elastic film. Furthermore, the x-axis of all the figures represents the evolution of the internal stress of the film normalized by the yield strength. The value given in the figures is designated by σ_0 because it is not the effective yield strength of the film but the input yield stress value of the simulation which can be increased when the internal stress are introduced

through a mismatch strain (see Section 6.4.3) as

$$\sigma_y = \begin{cases} \sigma_0 & \text{if } \sigma_i \leq \sigma_0 \ , \\ \sigma_i & \text{if } \sigma_i > \sigma_0 \ . \end{cases} \tag{6.29}$$

Later, the internal stress will be normalized by σ_0.

Remember that the domain shown in Fig. 6.22 is symmetric. The system is designed in such a way that the crack is propagating *along the centreline of the film* and not at an interface. The film remains thus always attached to either the adhesive layer or to the substrate. Now, the parameters of the crack path are taken similar to the one expected for a real interface.

Energetic dissipation in the adhesive layer

The influence of the adhesive layer on the dissipation in the film and on the relaxation of the internal stress is addressed first. The ratio between the amount of energy dissipated and elastically locked in the adhesive layer ($\Gamma^{\text{adh}}_{TOT}$) and the energy dissipated and elastically locked in all the layers of the system ($\Gamma^{\text{all}}_{TOT} = \Gamma^{\text{f}}_{TOT} + \Gamma^{\text{s}}_{TOT} + \Gamma^{\text{adh}}_{TOT}$) is represented in Fig. 6.24. For a film of 0.5 µm thickness, the energy dissipated in the adhesive layer amounts to about 30% of the total work. Above a thickness of 1 µm, the dissipation in the adhesive layer is negligible. The reason is that the adhesive layer is located far enough from the cracking interface. The size of the zone with stress values larger than the yield strength of the adhesive gets smaller than the film thickness when it increase. For film thicknesses below 1 µm, the adhesive layer involves significant amount of plastic dissipation and will thus affect the measurement results. The dissipation in the adhesive layer must then be taken into account.

The energetic dissipation in the adhesive layer is negligible for film thicknesses above 1 µm. *Below this value, the amount of dissipation in the adhesive layer is significant and it increases when the thickness decreases.*

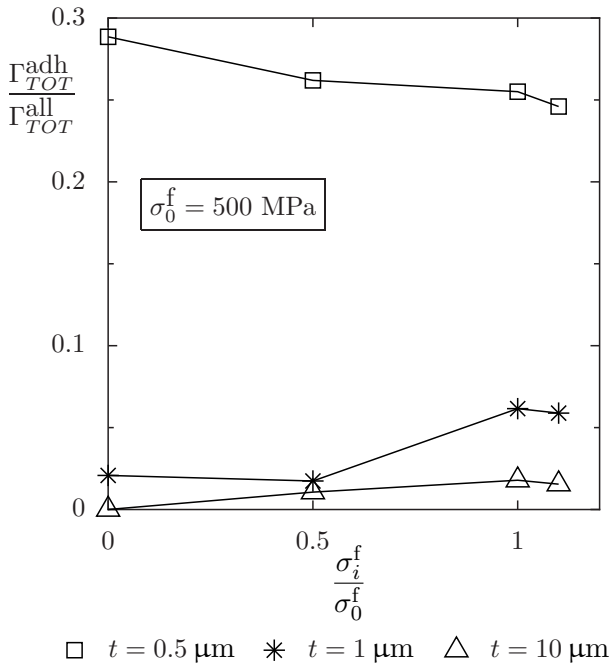

Figure 6.24: Ratio between the amount of energy dissipated in the adhesive layer and the total energy dissipated in all the layers of the system (coating, adhesive and substrate). The different symbols identify the three film thicknesses: 0.5, 1 and 10 µm.

Influence of the adhesive layer on the internal stress relaxation

In Figure 6.25, the ratio between the energy associated to the relaxation of the internal stress, $\mathcal{G}(\zeta\sigma_i)$, and the total elastic energy available in the film, $\Gamma^{\text{f}}_{el}|_{up}$, is plotted as a function of the film internal stress, $\sigma_i^{\text{f}}/\sigma_0^{\text{f}}$ in the presence or not of an adhesive layer. The results of two sets of computations are presented. The first set of results belongs the complete system shown in Fig. 6.22, and is represented by continuous lines. The second set of results belongs to the system without the adhesive layer, represented by the dashed lines.

The difference in the relaxation of the internal stress varies with the thickness of the film. This is related to the size of the plastic zone with respect to the film thickness. For the thinner film ($t = 0.5\,\mu$m), the cop-

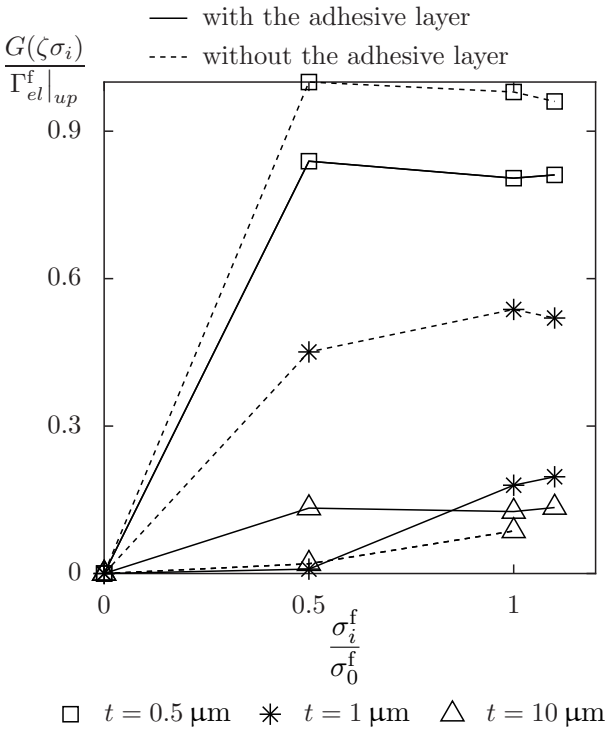

Figure 6.25: Variation of the ratio of the amount of energy effectively relaxed from the internal stress and entering the driving force for the delamination compared to the total available elastic energy as a function of the internal stress for different adhesive layer thicknesses. The different symbols identify the three film thicknesses: 0.5, 1 and 10 µm. The continuous lines represent the system with the adhesive layer and the dashed lines are for the system without the adhesive.

per film deforms plastically over the entire thickness and the internal stress almost fully relaxes. For the intermediate thickness ($t = 1\,\mu\mathrm{m}$), the copper film deforms plastically over the entire thickness in the absence of adhesive layer (dashed line) but not in the presence of adhesive layer (continuous line). For the thicker film, the zone of plastic deformation in the film is, in both cases, much thinner than the film thickness.

The relaxation of the internal stress is higher without the adhesive layer for the 0.5 and 1 µm film. The reason is that the plastic zone at the

crack tip is larger in the absence of the adhesive layer. This means that the film and the layer directly on top of it deform more in the plastic regime. The direct presence of the substrate on top of the film leads to a better relaxation and the remaining internal stress in the coating is lower after the propagation of the crack. In other words, the stress remaining in the film after the crack propagation is higher when there is an adhesive layer. For the thicker film, the adhesive layer does not influence crack propagation. The small difference between the two lines comes from the size of the plastic zone which is larger in the presence of an adhesive layer. But, in both cases, the size of the plastic zone is much smaller than the thickness of the coating.

The extent of plasticity in the film matters regarding the relaxation of the internal stress during cracking: the more the film yields plastically, the higher is the internal stress contribution to the crack propagation. If the film remains elastic, the fact that it is attached to the substrate after delamination prevents any relaxation.

Influence of the yield strength on the internal stress relaxation

Figure 6.26 shows the variation of the ratio between the energy coming from the relaxation of the internal stress, $\mathcal{G}(\zeta\sigma_i))$, and the total elastic energy available in the film, $\Gamma^{\mathrm{f}}_{el}|_{up}$, as a function of the film internal stress, $\sigma^{\mathrm{f}}_i/\sigma^{\mathrm{f}}_0$, for $\sigma_0 = 500\,\mathrm{MPa}$ and $\sigma_0 \to \infty$. The influence of the yield strength is very significant for the $0.5\,\mu\mathrm{m}$ film. The relaxation of the initial stress drops to zero when the yield strength of the film is infinite, in agreement with the conclusions in the previous paragraph.

For thicker films, the yield strength has almost no influence on the stress relaxation. The total value of dissipated energy is constant whatever the value of the yield strength but the location of the dissipation changes. The reason is that whatever the value of the yield strength, the plastic zone is so small with respect to the film thickness that it does not influence much the result. For the system with a low yield strength, the larger part of the dissipation takes part in the film layer. For the system with an infinite yield strength, the dissipation occurs in the substrate

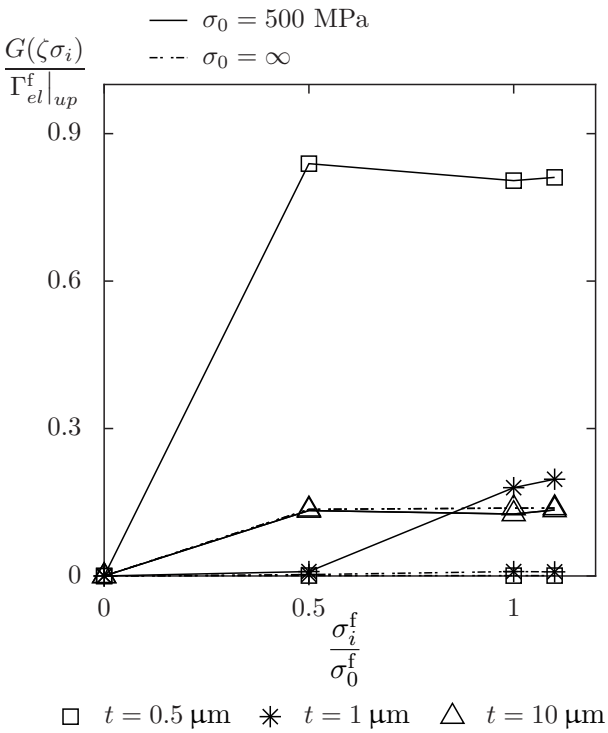

Figure 6.26: Variation of the ratio of the amount of energy coming from the internal stress used for the delamination as a function of the initial stress in the coating for different yield strengths. The different symbols identify the three film thicknesses: 0.5, 1 and 10 µm. The continuous line represents the system with $\sigma_0 = 500$ MPa and the dash-dot line belongs to the system with $\sigma_0 \to \infty$.

layer. In both cases, the dissipation in the adhesive layer is negligible compared with the main source of dissipation of the system.

For the two lower film thicknesses, the dissipation in the substrate layer is close to zero when the yield strength of the film is infinite. The film is too thin and does not bring enough energy to lead to plastic deformation of the substrate. The result is that almost no stress is relaxed by the propagation of the crack.

The yield strength has a large influence on the relaxation of the internal stress when the size of the plastic zone is close to the film thickness.

Contribution of the internal stress to the delamination

The contribution of the internal stress to the energy required for delamination is shown for each coating thickness in Fig. 6.27 as a function of the film internal stress, $\sigma_i^{\mathrm{f}}/\sigma_0^{\mathrm{f}}$. It is represented by the ratio between the energy coming from the internal stress $\mathcal{G}(\zeta\sigma_i)$ and the interface toughness $\mathcal{G}_c$. This contribution of the internal stress is always a small portion of the interface toughness.

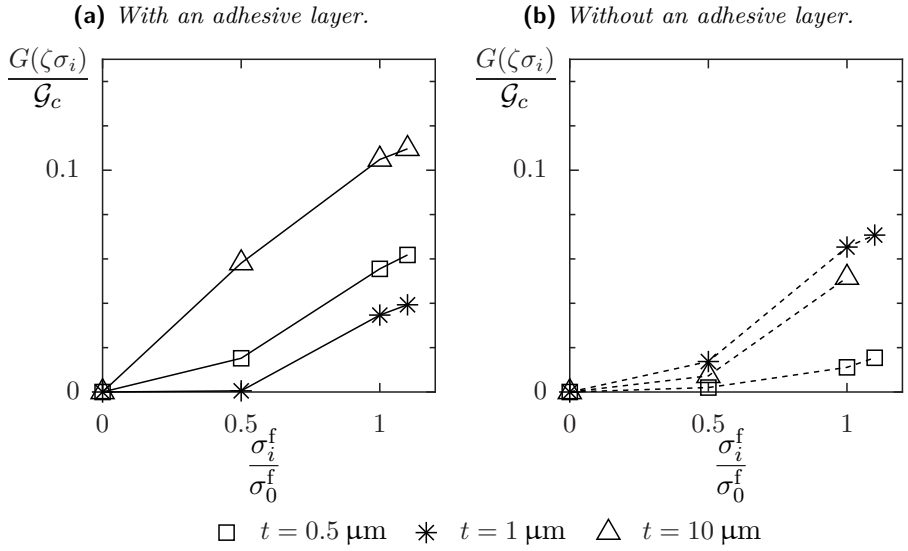

Figure 6.27: Variation of the ratio of the amount of energy coming from the internal stress used for the delamination with respect to the interface toughness as a function of the internal stress in the coating. The comparison is made between the system with an adhesive layer (a) and without adhesive layer (b).

6.7 Separation of the energy contributions in a wedge opening test on Cu coatings

Simulation of the real specimen have to be made with a much larger domain than for the idealized system. The crack length considered are between 5 and 15 mm. Moreover, as for the ideal model, the model must extend over a few millimeters in front of the crack tip and behind the wedge in order to impose the boundary conditions.

6.7.1 Description of the model

The geometry of the domain is shown in Fig. 6.28. The specimen is not symmetric as in the idealized system. The entire specimen has then to be modelled.

The variables describing the system are the same as for the idealized system. The dimensional analysis is then the same and is not repeated. The only difference in the layers is that there are two substrates. The properties of both substrates are identical and will be noted similarly with the superscript 's'.

The parameters of the adhesive and of both substrates are listed in Table 6.7. The value of the parameters characterizing the coating varies, as detailed in Table 6.8. As said earlier in Section 6.4.3, the values of

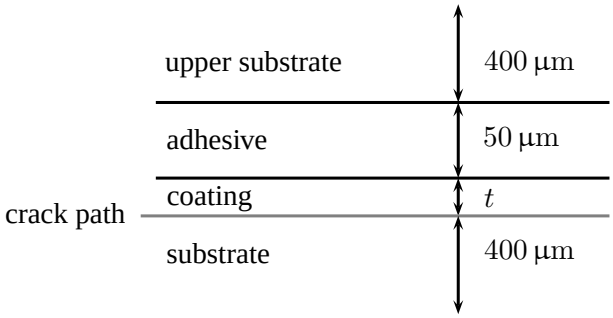

Figure 6.28: Schematic view of the geometry used to simulate the wedge opening test specimen.

the yield strength are taken from literature. Two cases are considered: a passivated film on one side or an unpassivated film. Moreover, two evolutions of the internal stress are also considered: a small change of internal stress with thickness as considering batch 3 in Fig. 6.12 and a large change of internal stress with thickness as considering batches 1 and 2 in Fig. 6.12. The mechanical properties (yield strength and internal stress) corresponding to these four cases, graphically shown in Fig. 6.17, are detailed in Table 6.8.

Table 6.7: Mechanical properties of the layers modeled for the real system. The parameters of the coating are given in Table 6.8.

	adhesive	substrates
Young's Modulus [GPa]	3	200
Yield strength [MPa]	20	215
Thickness [µm]	50	400
Internal stress [MPa]	0	0
Strain hardening exponent n [-]	0.1	0.3
Poisson ratio ν [-]	0.45	0.3

Table 6.8: Mechanical properties of the coating. Different properties are considered in the simulations (see Section 6.4.3). The thicknesses are given in µm and the stresses in MPa. The Young's modulus has been set equal to 110 GPa, n and ν are equal to 0.1 and 0.25, respectively.

	small variation of σ_i			large variation of σ_i		
	t	σ_0	σ_i	t	σ_0	σ_i
Unpassivated	0.5	270	92	0.5	270	342
	1	232	193	1	232	450
	1.5	207	197	1.5	207	410
	2	194	181	2	194	457
	t	σ_0	σ_i	t	σ_0	σ_i
Passivated	0.5	513	92	0.5	513	342
	1	299	193	1	299	450
	1.5	227	197	1.5	227	410
	2	192	181	2	192	457

6.7.2 Parametric study

The figures of this section show the influence of Γ_0 and other parameters on the energy release rate $\mathcal{G}$. For each of these figures, four different cases have been considered based on the evolution of the yield strength in Figure 6.17b and 6.17c. The different cases are explained in the previous section, with the following numbering:

1. Unpassivated film with the small variation of the internal stress (batch 3);
2. Unpassivated film with the large evolution of the internal stress (batch 1 & 2);
3. Passivated film with the small variation of the internal stress;
4. Passivated film with the large evolution of the internal stress.

evolution of the energy release rate with Γ_0

Figures 6.29 to 6.32 show the evolution of the value of $\mathcal{G}$ as a function of the work of adhesion Γ_0 for different coating thicknesses: $0.5, 1, 1.5$ and $2\,\mu$m.

The interface toughness raises with Γ_0. The first reason is that Γ_0 enters the expression of $\mathcal{G}$ and, secondly, the more energy is needed to break the interface, the more energy has to be brought in the layers near the crack tip and more energy is dissipated.

Regarding each coating thickness independently, the shape of the curves is the same for the different cases. The only exceptions are for cases 3 and 4 for a $0.5\,\mu$m coating. The reason is that for these cases, the yield strength of the coating is high and the internal stress is much lower, see Table 6.8. More energy has to be brought to the film to deform it plastically. The yield strength of the coating also influences the dissipation in the adhesive layer. For higher yield strength, less energy is needed to induce plasticity in the adhesive layer.

The difference between the curves on one graph (evolution with $\hat{\sigma}$) comes from that the peak stress affects very significantly the plastic dissipation

in the layers by controlling the magnitude of the stress reached locally. The ratio between the other parameters remains constant —regarding $\mathcal{G}$ approximately constant.

Considering a constant value of Γ_0, if $\hat{\sigma}$ raises, the dissipation in the coating and in the adhesive raises also. For coating thicknesses equal to 0.5 and 1 µm, the dissipation in the adhesive raises more sharply than for the thicker coatings. For coating thicknesses of 1.5 and 2 µm, the dissipation in the coating in larger than the dissipation in the adhesive. It is then the most important parameter.

The raise of the interface toughness with Γ_0 *is mainly due to "extrinsic" plastic dissipation raising in the adhesive layer for coating thicknesses equal to* 0.5 *and* 1 µm *and to the plastic dissipation in the coating itself for the coating thicknesses equal* 1.5 *and* 2 µm.

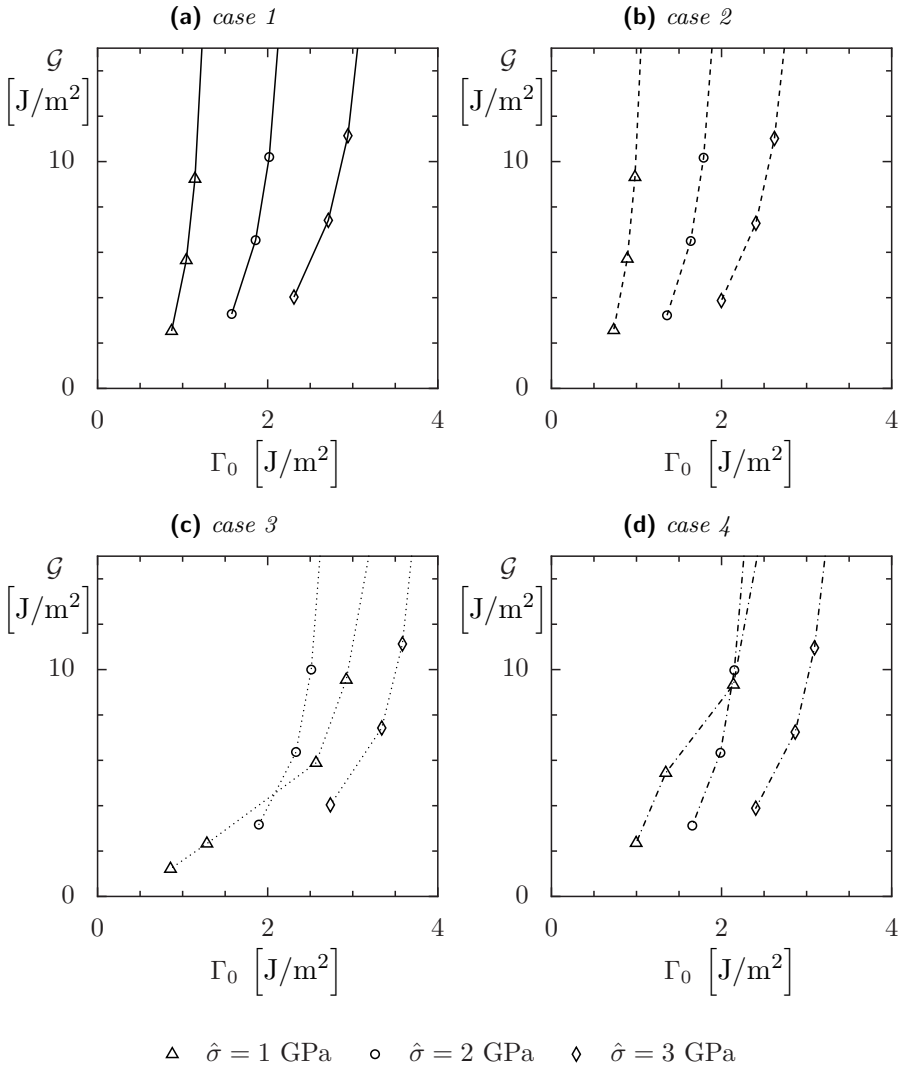

Figure 6.29: Variation of the energy release rate $\mathcal{G}$ as a function of Γ_0 for a $0.5\,\mu\mathrm{m}$ thick film with different properties. The different evolutions within each graph are obtained for three distinct interface peak stresses equal to $1, 2$ and $3\,\mathrm{GPa}$.

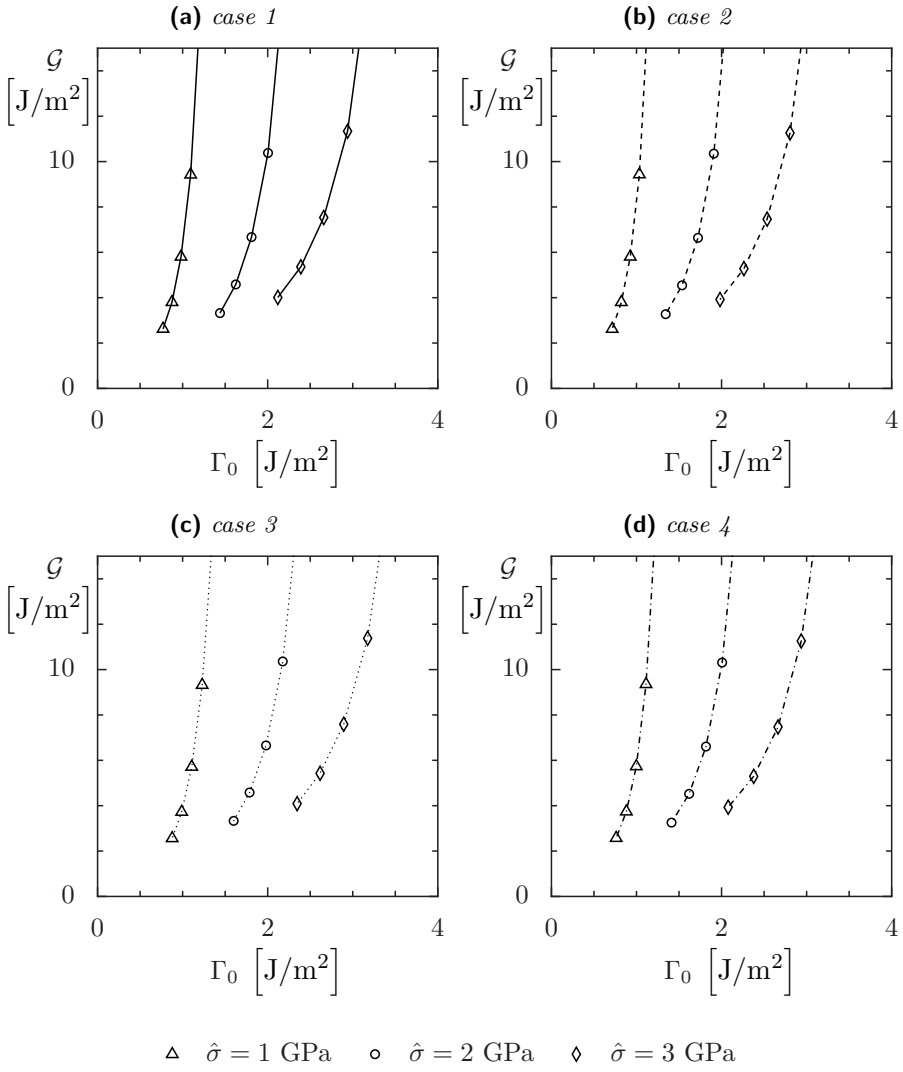

Figure 6.30: Variation of the energy release rate $\mathcal{G}$ as a function of Γ_0 for a 1 µm thick film with different properties. The different evolutions within each graph are obtained for three distinct interface peak stresses equal to $1, 2$ and $3\,\mathrm{GPa}$.

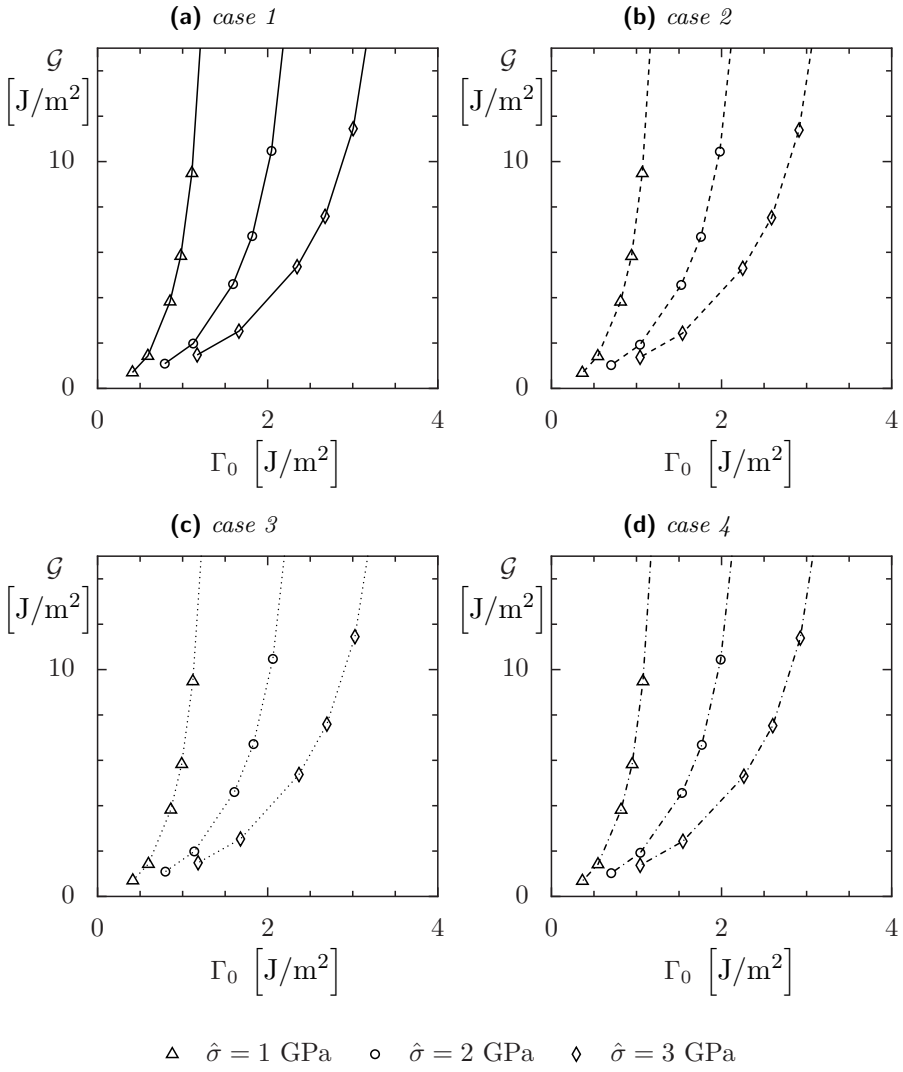

Figure 6.31: Variation of the energy release rate $\mathcal{G}$ as a function of Γ_0 for a 1.5 µm thick film with different properties. The different evolutions within each graph are obtained for three distinct interface peak stresses equal to $1, 2$ and 3 GPa.

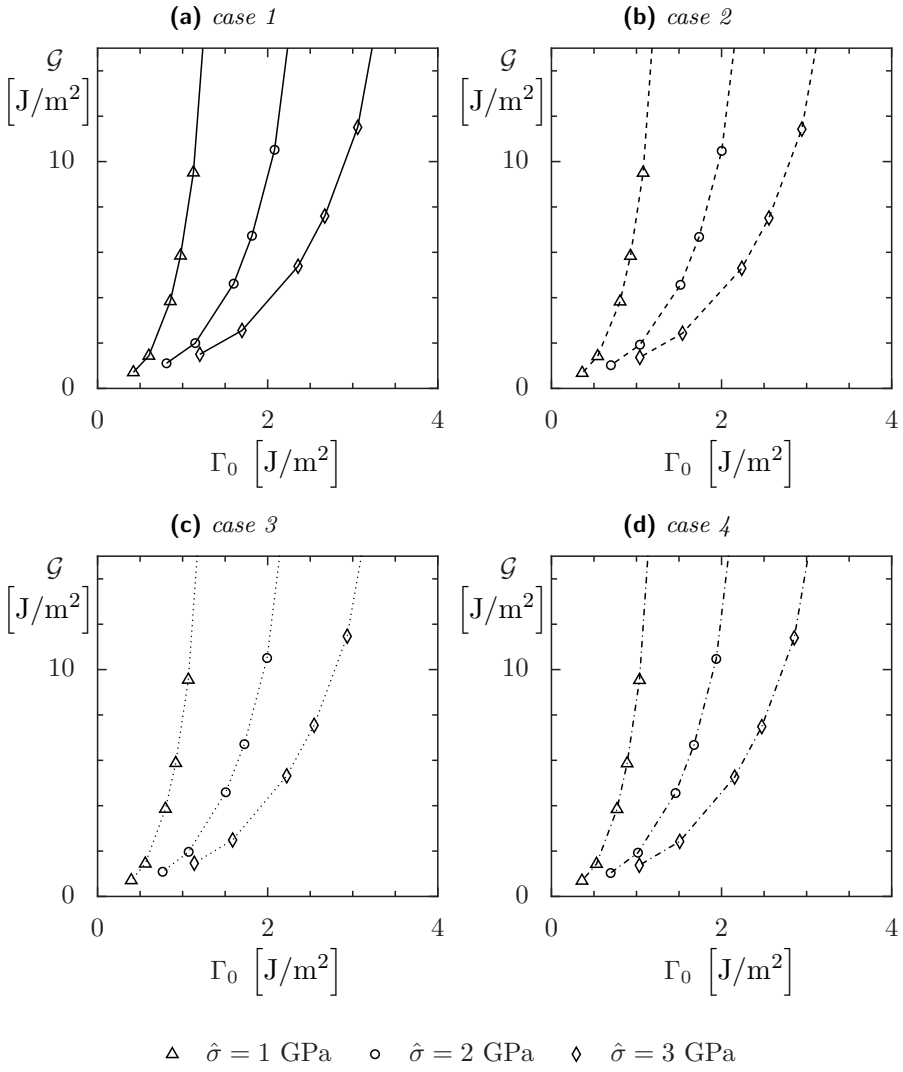

Figure 6.32: Variation of the energy release rate $\mathcal{G}$ as a function of Γ_0 for a 2 µm thick film with different properties. The different evolutions within each graph are obtained for three distinct interface peak stresses equal to $1, 2$ and 3 GPa.

Validity of the analytical expression

Figures 6.33 to 6.36 shows the difference between the interface toughness computed from the sum of the energy dissipation of each layer given by FE simulation (as in Eq. (6.2)), which will be designed by $\mathcal{G}^{\text{num}}$, and the "elastic" solution $\mathcal{G}$ computed from Eq. (6.1), using the crack length of the corresponding simulation. The value of $\mathcal{G}$ will be used in the next section to make the link with the experimental results. The validity of this elastic solution is checked now.

When the film is thick, i.e. larger than 1.5 µm, the elastic solution is realistic over a wider range of Γ_0. Plastic dissipation in the adhesive layer is small. Cases 3 and 4 for 0.5 µm (Fig. 6.33c and 6.33d) are again different. When $\hat{\sigma} = 1\,\text{GPa}$, the error is very small over a wider range of Γ_0. This is because the system remains elastic for small values of $\hat{\sigma}$. Except for these two curves, there is no striking difference between the different cases while regarding each thickness independently.

Comparing with the curves of the previous section, the relative difference $(\mathcal{G}^{\text{num}} - \mathcal{G})/\mathcal{G}^{\text{num}}$ follows the evolution of $\mathcal{G}$. The higher the $\mathcal{G}$, see Figs. 6.29 to 6.32, the higher the difference in the corresponding Figs. 6.33 to 6.36.

The analytical expression is physically correct for small values of Γ_0 *and* $\hat{\sigma}$ *or for film thickness larger than* 1 µm*, i.e. as plastic dissipation in the adhesive layer is small.*

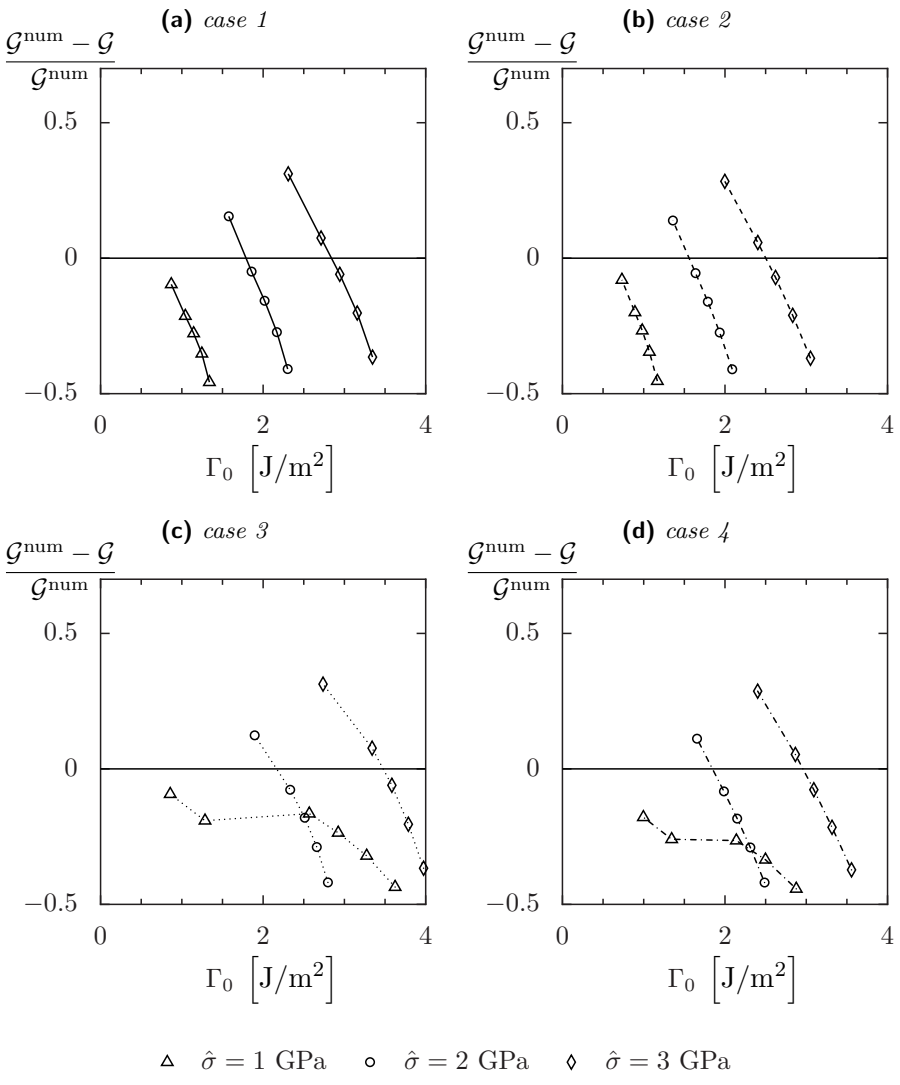

Figure 6.33: Evolution of the relative difference between the energy release rate $\mathcal{G}^{\text{num}}$ and the analytical $\mathcal{G}$ using Eq. (6.1) with Γ_0 for a $0.5\,\mu\text{m}$ thick film with different properties. The different evolutions within each graph are for three distinct interface peak stresses equal to $1, 2$ and $3\,\text{GPa}$.

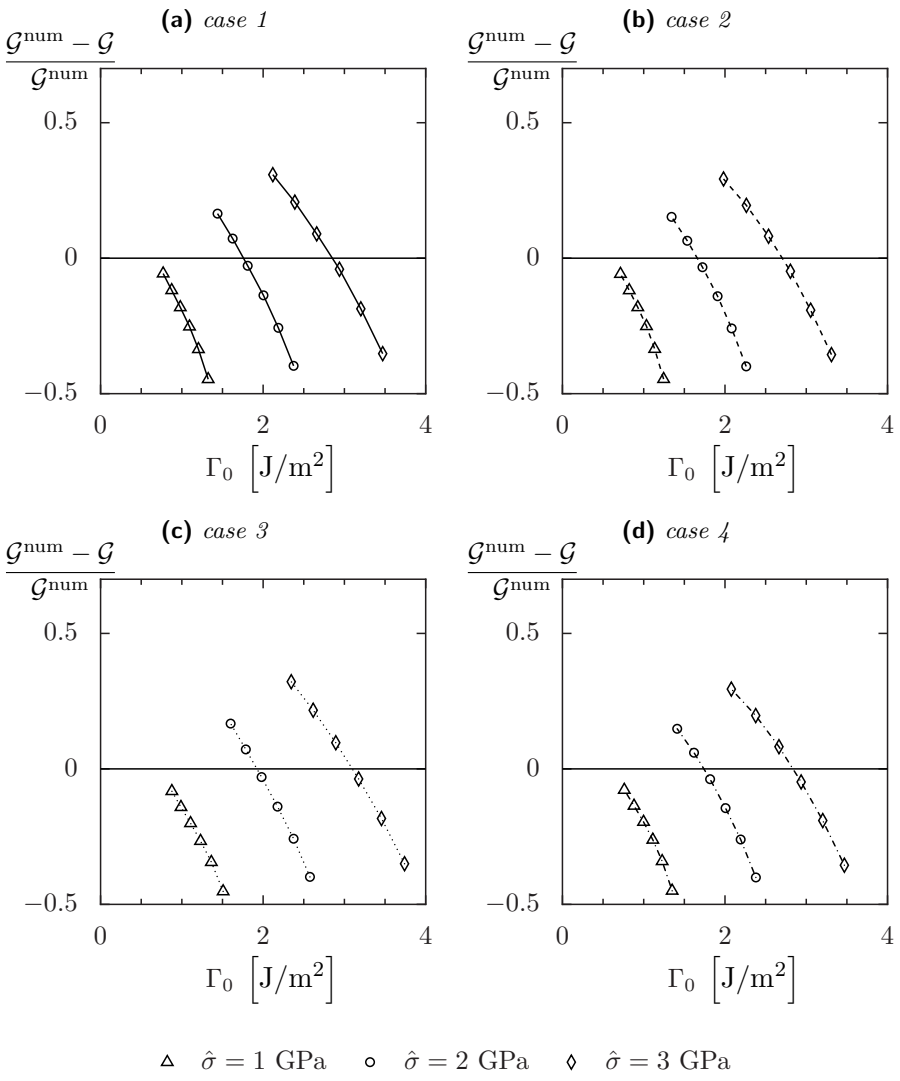

Figure 6.34: Evolution of the relative difference between the energy release rate $\mathcal{G}^{\text{num}}$ and the analytical $\mathcal{G}$ using Eq. (6.1) with Γ_0 for a 1 µm thick film with different properties. The different evolutions within each graph are for three distinct interface peak stresses equal to 1, 2 and 3 GPa.

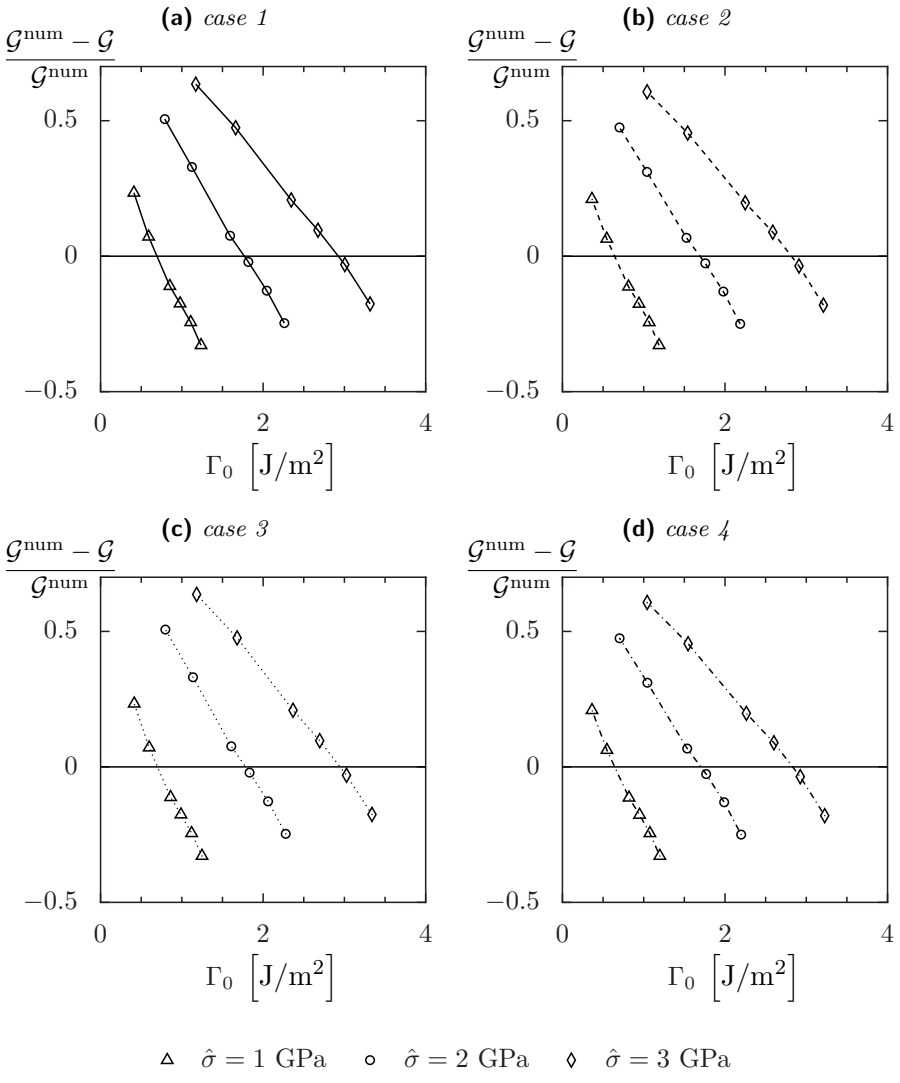

Figure 6.35: Evolution of the relative difference between the energy release rate $\mathcal{G}^{\text{num}}$ and the analytical $\mathcal{G}$ using Eq. (6.1) with Γ_0 for a 1.5 µm thick film with different properties. The different evolutions within each graph are for three distinct interface peak stresses equal to $1, 2$ and 3 GPa.

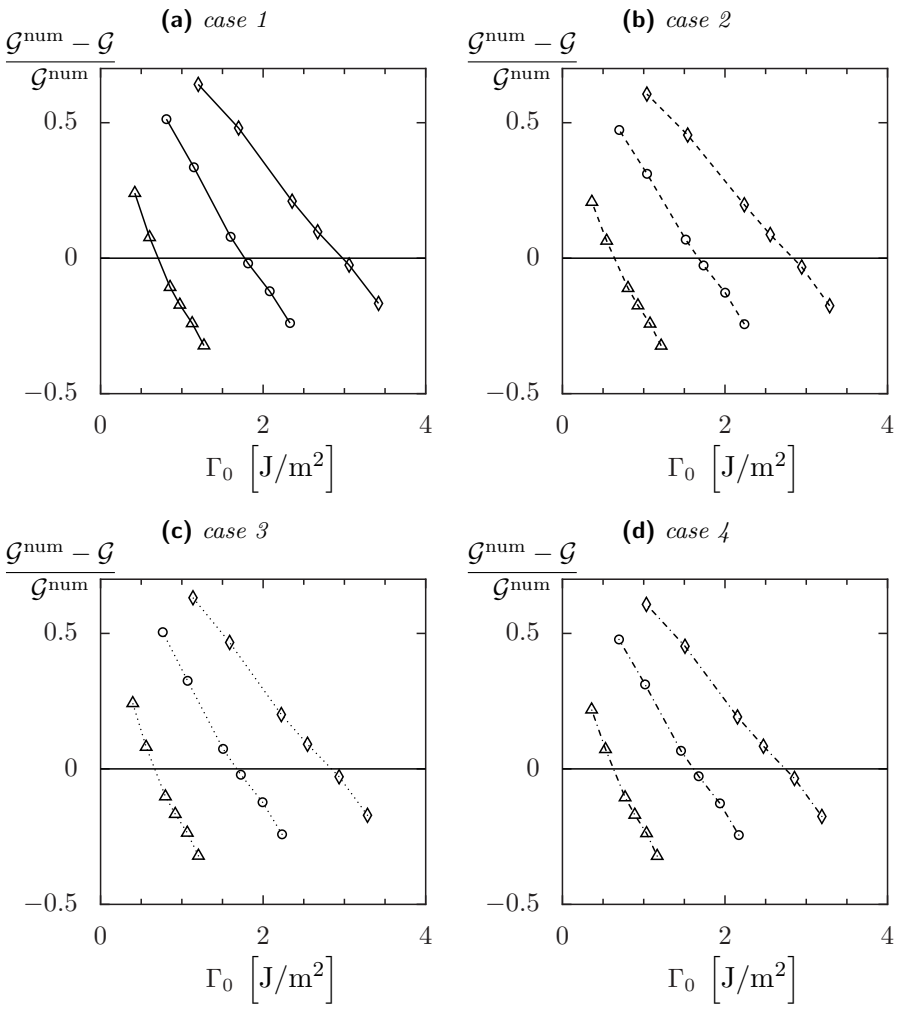

Figure 6.36: Evolution of the relative difference between the energy release rate $\mathcal{G}^{\text{num}}$ and the analytical $\mathcal{G}$ using Eq. (6.1) with Γ_0 for a 2 µm thick film with different properties. The different evolutions within each graph are for three distinct interface peak stresses equal to 1, 2 and 3 GPa.

6.8 Application to the copper coating system and discussion

Note: This section compares experimental and numerical values of the energy release rate associated to the external loading $\mathcal{G}$. Experimentally, $\mathcal{G}$ is computed from the measured crack length by using the analytical equation (6.1) on page 96. Numerically, $\mathcal{G}$ can be either computed by using same Eq. (6.1) and the crack length given by the FE simulation or by using Eq. (6.2) with the FE results. The only difference between these two expressions comes from contribution of the adhesive layer neglected in the analytical equation (6.1) as well as from the cohesive zone response with a strength limited by the peak stress. It is discussed at the end of this section.

Pursuing with the convention used in the previous section, the experimental or numerical value obtained from Eq. (6.1) is noted $\mathcal{G}$ and also designated by *analytical energy release rate.* $\mathcal{G}^{\text{num}}$ represents the value obtained from Eq. (6.2) only from numerical results. The distinction between the experimental and numerical value of $\mathcal{G}$ will be clearly made when both are used within the same graph.

Figures 6.37 to 6.39 shows the evolution of $\mathcal{G}$ computed using Eq. (6.1) with the crack length given by the FE simulation. The reason for using the analytical expression of $\mathcal{G}$ is to allow the comparison with the experimental data which have been obtained with the same expression. The four different cases are again shown but in this section, the comparison within each graph is made between the different coating thicknesses, considering the three different values of $\hat{\sigma}$ within different figures.

For each value of $\hat{\sigma}$, the four cases are clearly different from each other. These three pictures will be used to determine which case will be compared to the experimental data. Small difference can be observed while varying the value of $\hat{\sigma}$ but the general trends are the same.

Cases 3 and 4 do not follow the evolution of the experimental data. Considering a constant value of Γ_0 —it is assumed that the interface properties do not change with the layer thickness— the adherence increases with the film thickness. This is in contradiction with the experimental data of Fig. 6.18.

Considering case 1, the different curves are too close to each other to be able to distinguish them. This means no variation of the adherence with the thickness. It again does not agree with experimental data.

Case 2 seems to follow the right evolution and it is the results of these simulations that will be compared with the experimental data at the end of this section.

The difference between each case while comparing the different film thicknesses are clearly visible. Case 2 is qualitatively in agreement with experimental data.

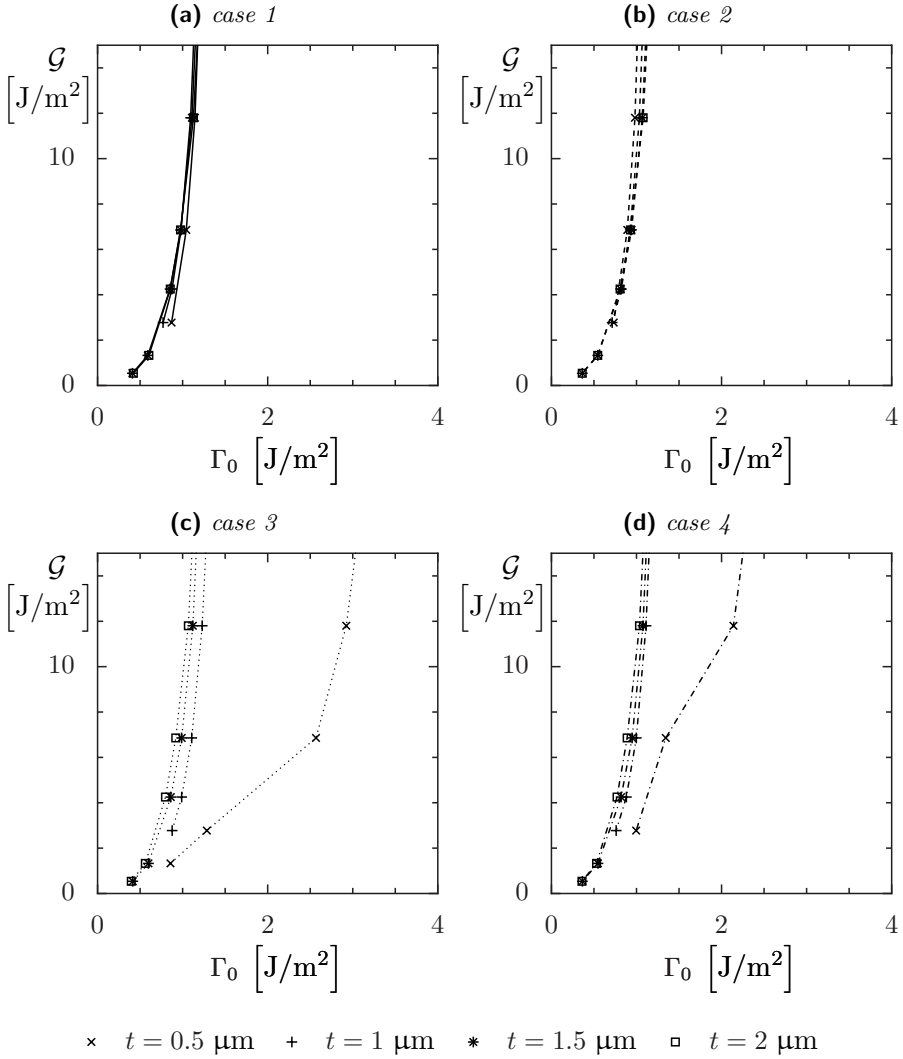

Figure 6.37: Variation of $\mathcal{G}$ evaluated using Eq. (6.1) as a function of Γ_0 for the different cases of Table 6.8, with $\hat{\sigma} = 1$ GPa. The different evolution within each graph are for different film thicknesses: $0.5, 1, 1.5$ and $2\,\mu$m.

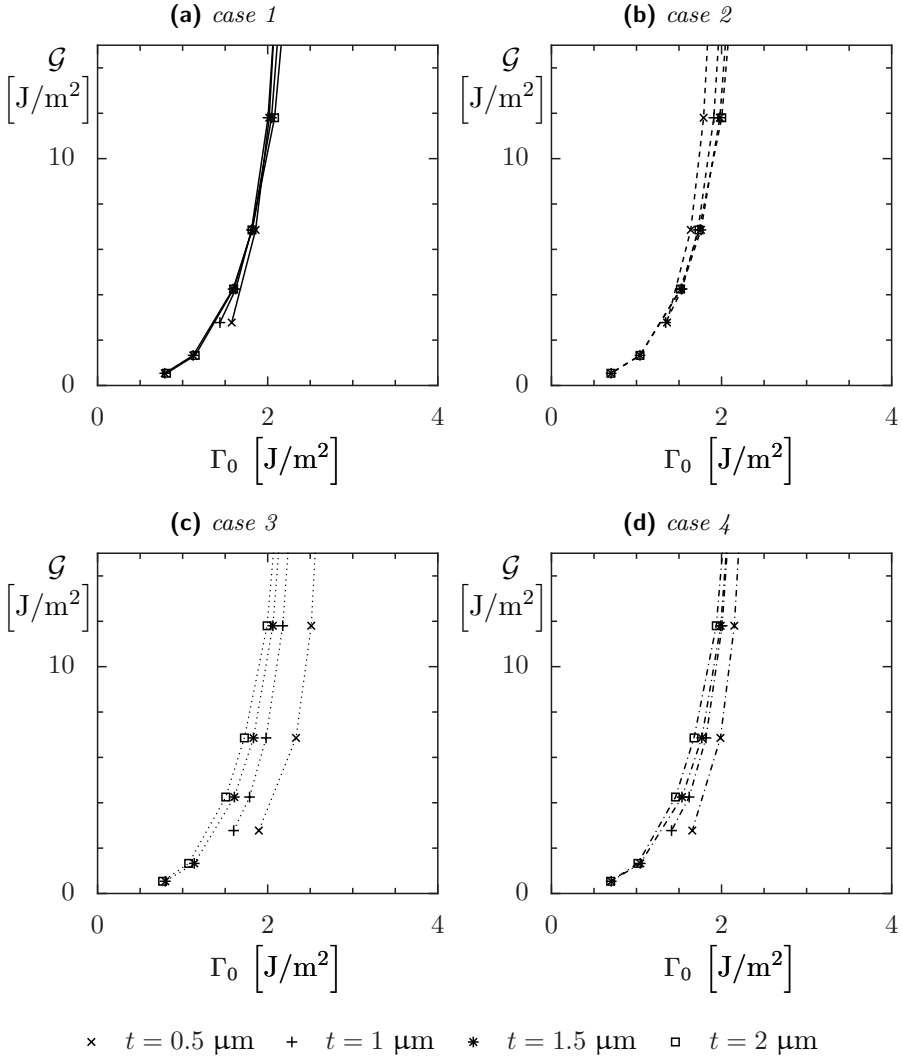

Figure 6.38: Variation of $\mathcal{G}$ evaluated using Eq. (6.1) as a function of Γ_0 for the different cases of Table 6.8, with $\hat{\sigma} = 2\,\mathrm{GPa}$. The different evolution within each graph are for different film thicknesses: $0.5, 1, 1.5$ and $2\,\mu\mathrm{m}$.

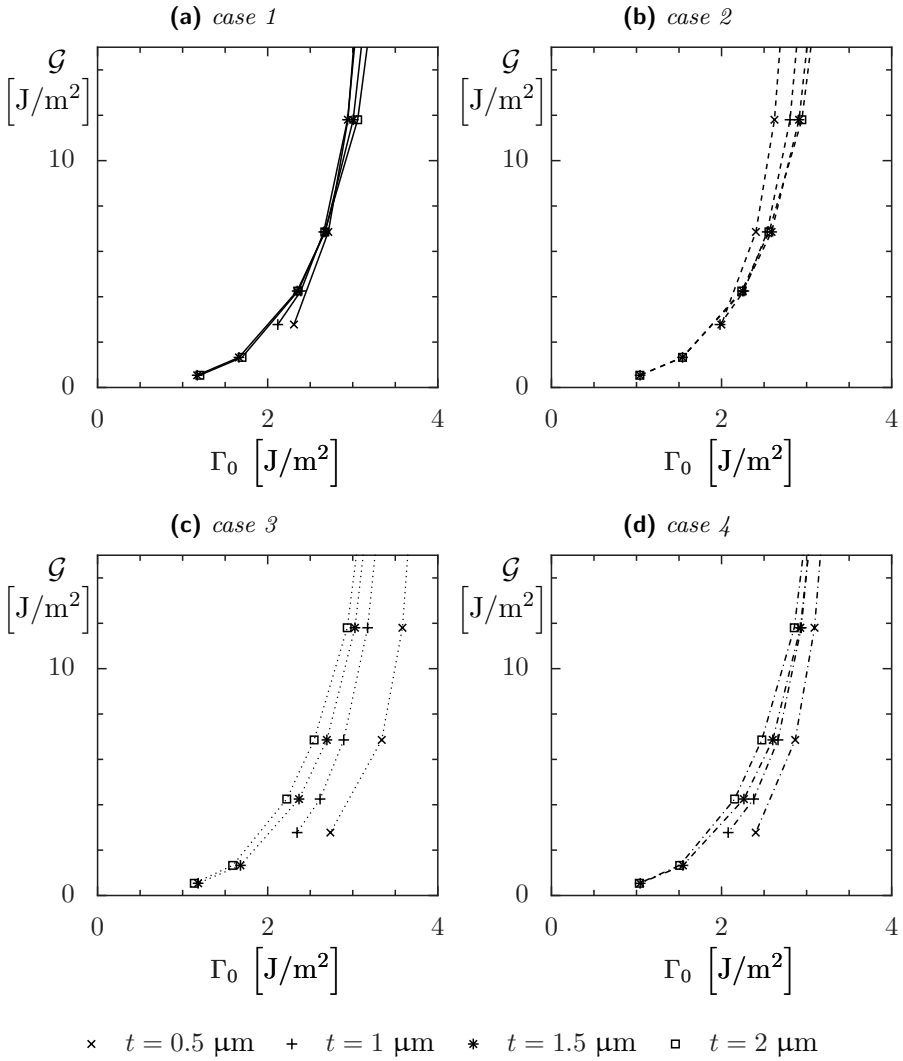

Figure 6.39: Variation of $\mathcal{G}$ evaluated using Eq. (6.1) as a function of Γ_0 for the different cases of Table 6.8, with $\hat{\sigma} = 3\,\mathrm{GPa}$. The different evolution within each graph are for different film thicknesses: $0.5, 1, 1.5$ and $2\,\mu\mathrm{m}$.

6.8.1 Variation of the energy release rate with coating thickness

The variation of the energy release rate as calculated with the analytical formula is shown on Figs. 6.40, 6.41 and 6.42, together with the experimental results. The three figures correspond to an interface strength $\hat{\sigma}$ equal to 1, 2 and 3 GPa, respectively. The properties of the coating layer are those of case 2, meaning:

t [μm]	σ_0 [MPa]	σ_i [MPa]
0.5	313	342
1	246	450
1.5	223	410
2	212	457

Remark: the values of the yield strength given in the table are the input values of the numerical simulations. We have shown in Section 6.4.3 that if the internal stress in the layer is higher than the yield strength, then $\sigma_y = \sigma_i$.

Three different evolutions of $\mathcal{G}$ with the film thickness have been determined for each value of the interface strength $\hat{\sigma}$. Each of them corresponds to a unique value of Γ_0. This value has been determined from the corresponding figure 6.37(b) or 6.38(b) or 6.39(b) by taking the value of

1. Γ_0 corresponding to $\mathcal{G} = 10.24\,\mathrm{J/m^2}$ on the curve for a film thickness $t = 0.5\,\mu\mathrm{m}$. This curve is represented by the crosses ($\times$) in the figures.

2. Γ_0 corresponding to $\mathcal{G} = 5.14\,\mathrm{J/m^2}$ on the curve for a film thickness $t = 1\,\mu\mathrm{m}$. This curve is represented by the plus symbols ($+$) in the figures.

3. Γ_0 corresponding to $\mathcal{G} = \mathcal{G}^{\mathrm{num}}$ for a film thickness $t = 2\,\mu\mathrm{m}$. This curve is represented with asterisks ($\ast$) in the figures.

The results are not as close to the experimental data as expected. The value of $\mathcal{G}$ generally decreases between film thicknesses equal to 0.5 μm

and 1 µm. For thicker films, FE simulations predict a constant value of the adherence with the thickness.

The goal of the simulations was to study the influence of the coating thickness, including the variation of the yield strength and the variation of the internal stress. These two parameters are not sufficient to fully explain the evolution of the adherence of a copper coating on stainless steel with its thickness. Note first that the yield strength of the film has been taken from the literature and some properties of the films deposited during this thesis are different (i.e. the grain size). The other parameter studied in this thesis, the internal stress, seems to have an influence smaller than expected. Internal stress affect the plastic deformation in the coating with an impact also on the relaxation but the global impact remains weak. This has been shown on the ideal system in the previous section. Two effects play an opposite role. The larger is the internal stress, the larger is the plastic dissipation which increases the resistive force. But, larger is also the elastic relaxation which increases the driving force.

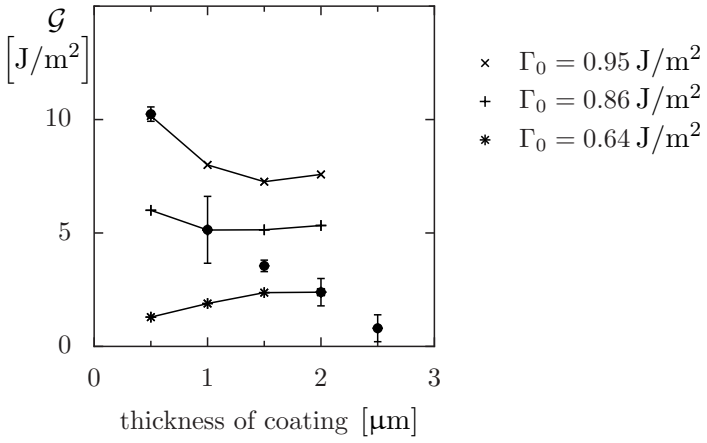

Figure 6.40: Variation of the analytical energy release rate computed from experimental data (filled circles) or from numerical simulations. The computation have been made using the parameters of case 2 and $\hat{\sigma} = 1\,\mathrm{GPa}$.

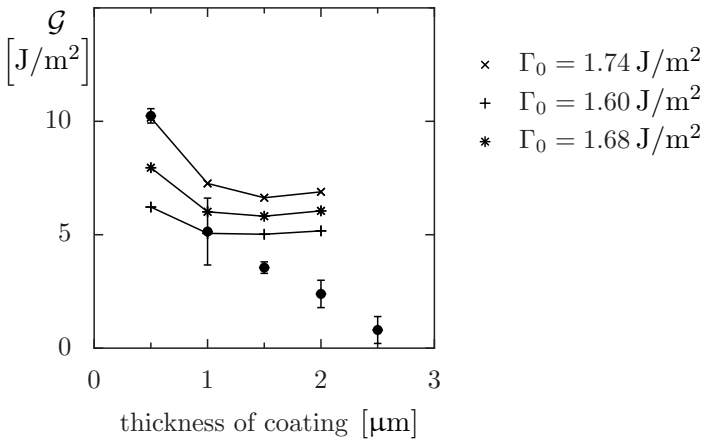

Figure 6.41: Variation of the analytical energy release rate computed from experimental data (filled circles) or from numerical simulations. The computation have been made using the parameters of case 2 and $\hat{\sigma} = 2\,\mathrm{GPa}$.

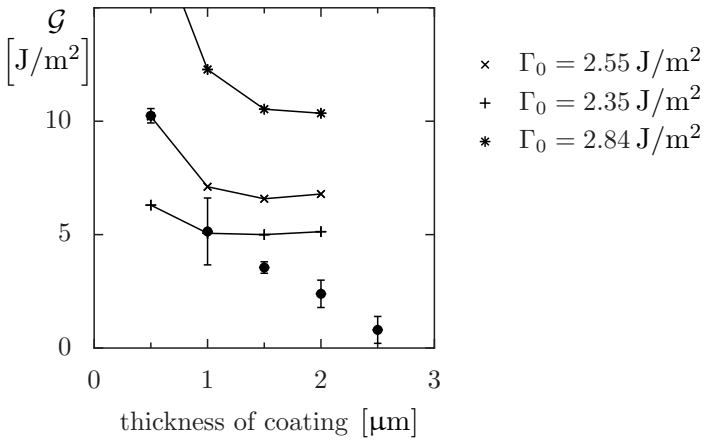

Figure 6.42: Variation of the analytical energy release rate computed from experimental data (filled circles) or from numerical simulations. The computation have been made using the parameters of case 2 and $\hat{\sigma} = 3\,\mathrm{GPa}$.

Using the methodology described in the previous section, the set of parameters providing the closest agreement with the experimental data is $\Gamma_0 = 1.68\,\mathrm{J/m^2}$ and $\hat{\sigma} = 2\,\mathrm{GPa}$, see $(*)$ in Fig. 6.41. But it does not catch the entire variation of $\mathcal{G}$, especially for thick films. Further improvement has to be made. Another strategy has been followed to identify the parameters, starting from the optimum case found here above. Simulation have been performed over a wide range of interface parameters $\hat{\sigma}$ for film thicknesses equal to 0.5 and 2 µm. The value of the corresponding work of fracture Γ_0 were compared for the two film thicknesses. The closest value of Γ_0 between the two configurations was obtained for an interface strength of 1.2 GPa with a corresponding value of Γ_0 equal to $0.81\,\mathrm{J/m^2}$.

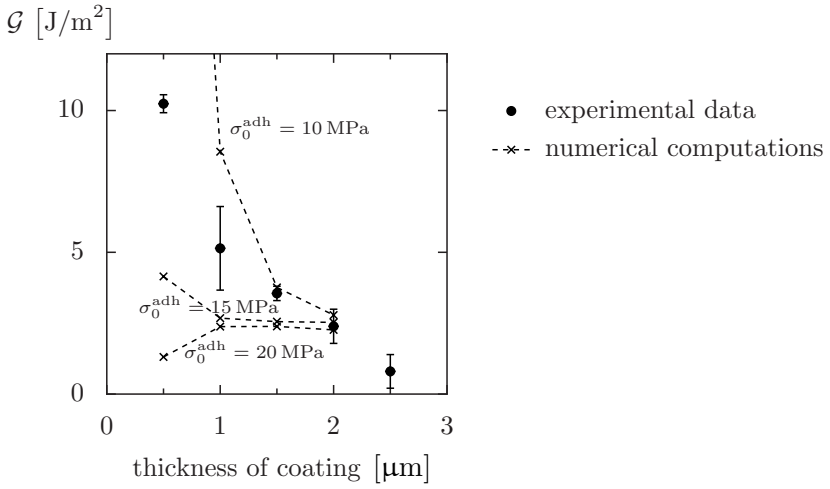

Figure 6.43: Variation of the analytical energy release rate computed from experimental data (filled circles) or from numerical simulations. Two different set of simulations are shown with the yield strength of the adhesive layer equal to 10 MPa (upper line) and 15 MPa (lower line). The parameters of the interface are $\Gamma_0 = 0.81\,\mathrm{MPa}$ and $\hat{\sigma} = 1.2\,\mathrm{GPa}$.

Figure 6.43 shows that the system is very sensitive to the yield strength of the adhesive layer, which is not precisely known. The yield strength of the adhesive layer has been set to 12 MPa, which gives the best agreement with the experimental values. These values are given in Table 6.9

together with the properties of the coating. The comparison between the experimental values and the numerical simulations is shown in Fig. 6.44.

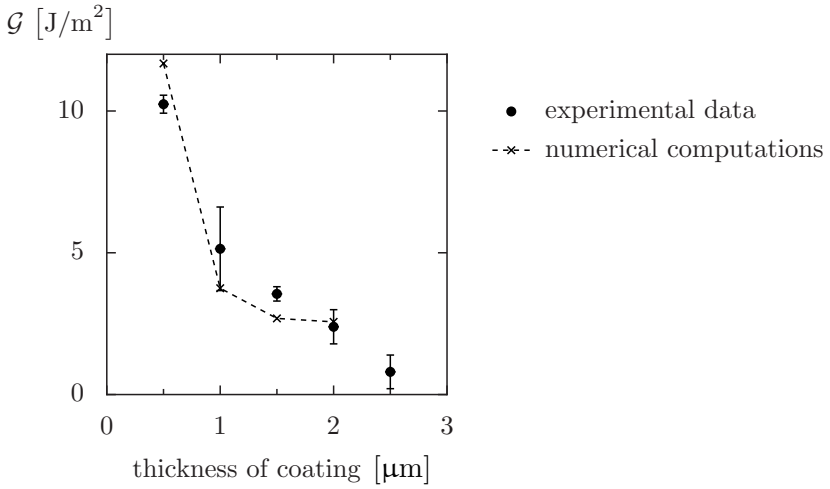

Figure 6.44: Variation of the analytical energy release rate, comparison between experimental data (filled circles) and numerical simulations. The simulation has been performed using the properties given in Table 6.9.

Table 6.9: Specimen properties used for the FE simulations.

specimen properties		coatings properties		
		t	σ_0	σ_i
$\hat{\sigma}$	1.2 GPa	0.5	270	342
Γ_0	0.81 J/m^2	1	232	450
σ_0^{adh}	12 MPa	1.5	207	410
		2	194	457

The comparison between the deformation profile measured on real specimen and the deformation profile extracted from the FE simulation is given for each coating thickness in Fig. 6.45. The simulations catch the deformation at the crack tip but curvature of the profile is a slightly smaller than the real profile measured by the profilometer.

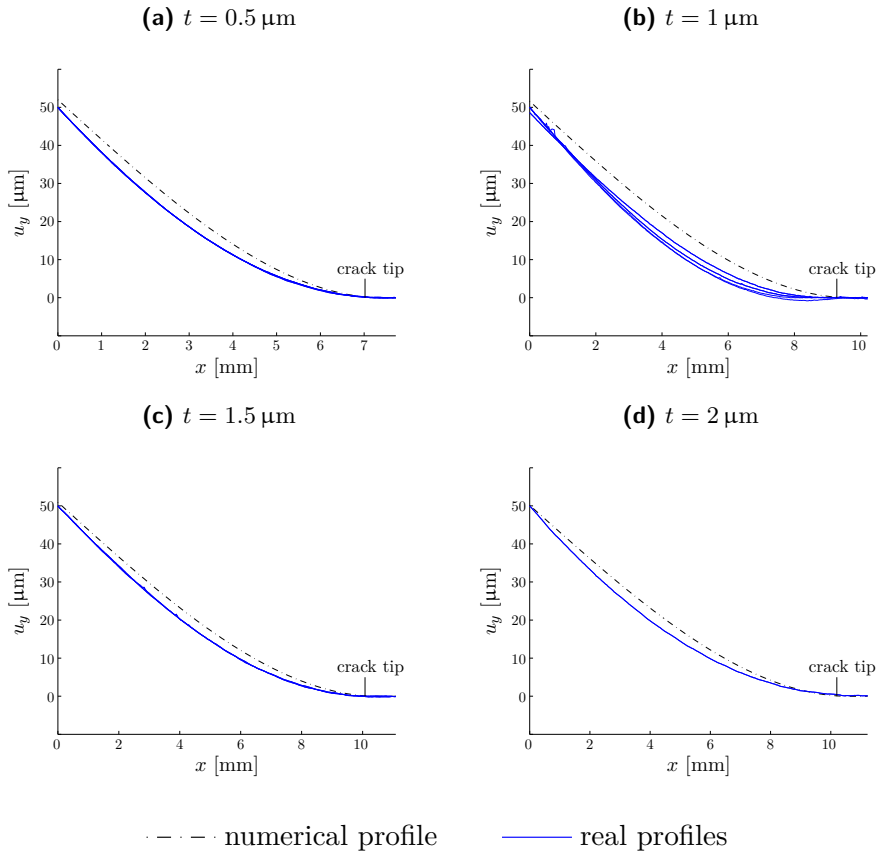

Figure 6.45: Comparison between the deformation profile measured on real specimens and the deformation profile extracted from the FE simulation for the different coating thicknesses.

Table 6.10 shows the contribution of the different layers to the energy release rate associated to the external loading $\mathcal{G}^{\text{num}}$ (the analytic value $\mathcal{G}$ has been put for comparison) for this configuration, depending on the coating thickness. The total dissipation in the film decreases while increasing the film thickness. This observation is not what was intuitively expected. More energy dissipation was expected in a thicker film as it has more volume into which plastic work can be dissipated. On the other hand, it is the variation of the yield strength (due to the variation of internal stress) that dictates the dissipation. Due to the lower yield strength for the thinner film, as caused by the internal stress effect, plastic dissipation will happen at a lower stress state, leading to a larger amount of dissipation. For the coating thicknesses of 1, 1.5 and 2 µm, the internal stress in the coatings are similar. This is explained by the fact that the plastic zone is smaller than the coating thickness so the dissipation becomes independent of the coating thickness. The values of the dissipation are then close for these three coating thicknesses. Looking at the adhesive layer, the total dissipation drops between the coating thicknesses of 0.5 µm and 1 µm, as expected from the study on the ideal system. For higher thicknesses, it still decreases but more slowly. The amount of internal stress contributing to the delamination $\mathcal{G}(\zeta\sigma_i)$ is given in the table for information. The effect of the internal stress is already taken into account in the energy dissipated in the different layers and is not to be subtracted from of the total value of $\mathcal{G}^{\text{num}}$. The last line of Table 6.10 gives the value of the interface toughness for each coating thicknesses. These values are close to one another, meaning that the interface properties do not significantly vary with the coating thickness.

The variation of the adhesion measured between the different coatings thicknesses is mainly due to the dissipation in the adhesive layer. The dissipation in the adhesive layer is high for thinner coatings and drops as the thickness of the coating increase. Another contribution, which explains also the variation of the interface toughness, is the decrease of the dissipation in the coating.

Table 6.10: Energy contribution of each layer to the energy release rate for the different coating thicknesses and $\Gamma_0 = 0.81\,\mathrm{J/m^2}$. The value of the interface toughness can be determined by addition of the energy contribution of the substrate and coating and Γ_0. The last line of the table shows the interface toughness for each layer.

t [µm]	0.5	1	1.5	2
$\mathcal{G}(\zeta\sigma_i)\ \left[\mathrm{J/m^2}\right]$	0.002	0.087	0.153	0.22
$\Gamma^{\mathrm{adh}}\ \left[\mathrm{J/m^2}\right]$	6.30	0.93	0.27	0.15
$\Gamma^{\mathrm{f}}\ \left[\mathrm{J/m^2}\right]$	2.12	1.65	1.47	1.45
$\Gamma^{\mathrm{s}}\ \left[\mathrm{J/m^2}\right]$	0.07	0.13	0.14	0.17
$\Gamma_0\ \left[\mathrm{J/m^2}\right]$	0.808	0.805	0.804	0.804
$\mathcal{G}^{\mathrm{num}}\ \left[\mathrm{J/m^2}\right]$	9.31	3.52	2.69	2.58
$\mathcal{G}\ \left[\mathrm{J/m^2}\right]$	11.68	3.75	2.68	2.56
$\mathcal{G}_c\ \left[\mathrm{J/m^2}\right]$	3.00	2.58	2.41	2.43

6.8.2 Error on the analytic energy release rate

The comparison of the previous section is based on values computed from the analytical equation (6.1). We are aware that this expression is not exact. Equation (6.1) neglects the adhesive layer. This hypothesis is restrictive and we have seen that a large amount of dissipation can occur in this layer. Figure 6.46 shows the error made using the analytical expression. The data are taken from the simulation with the closest agreement with the experimental data ($\hat{\sigma} = 1.2\,\mathrm{GPa}$ and $\Gamma_0 = 0.81\,\mathrm{J/m^2}$).

As expected, the error is the largest (more than 25%) for a coating thickness equal to 0.5 µm. The error drops down to about 6% for a coating thickness of 1 µm and, for bigger film thicknesses, the error is lower than 1%.

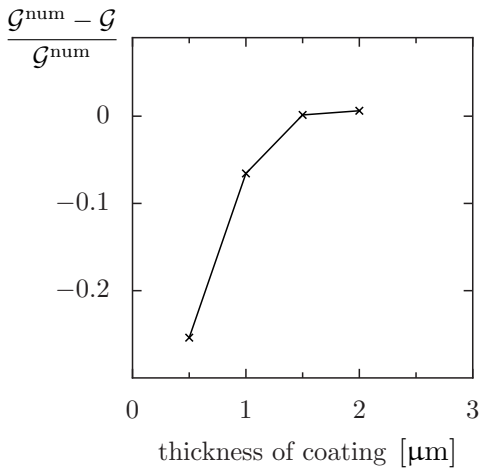

Figure 6.46: Error made using the analytical expression (6.1). The parameters considered are the same as for Table 6.10.

Chapter 7

Conclusions and perspectives

Adhesion is a complex and fascinating multiscale scientific phenomenon but is also a burden for all industries working with thin films and coatings. Even if this thesis is not providing the miraculous recipe for solving all adhesion problems, it has contributed in setting up a scientific methodology to address the problem.

An original methodology for the wedge opening test has been developed in order to measure the adhesion of thin films. The crack length measurement for non transparent substrates which is needed to evaluate the energy release rate is one of the main contribution of this thesis.

The **wedge opening test** method has been assessed and widely used during this thesis. The different steps of the testing procedure are well defined. The test is easy to perform and could be used, if needed, under different temperature and environmental conditions. The most important aspect of the test is an accurate measurement of the crack length. Indeed, the expression to compute the interface toughness, i.e.

$$\mathcal{G} = \frac{3\bar{E}h^3D^2}{16a^4}\left(1 + 0.674\frac{h}{a}\right)^2 \quad . \tag{7.1}$$

Shows that the accuracy on the crack length value a is of prime importance as it enters the energy release rate equation with a fourth power.

The substrate being non transparent, the crack length is also the most difficult parameter to measure. The original solution proposed in this work and validated on an ideal Si/Si bonding is to estimate the crack length from the out of plane displacement profile of the specimen. This measurement is made by a profilometer. The accuracy in the crack length is directly related to the quality of the profilometer, see Chapter 5. The fact that the value of the crack length is determined with a field measurement along the specimen arm and not from a single point value is an important contribution of this thesis, improving the reliability of the technique.

The **four-point bending and blister tests** have also been used to measure the adhesion of thin films. Even though the faisability of these techniques has been demonstrated on other systems [14,28,47], technical issues remain to be solved to be applied to the two systems investigated in this thesis, i.e. TiN on stainless steel and Cu on stainless steel. The main problem with these two techniques is that the initiation requires a high amount of energy —to be first stored elastically in the specimen— which is released immediately at the onset of crack propagation. The propagation is unstable and can not be controlled. Thus, no information about crack propagation can be collected. The solutions are: for the bending test, initiation can be obtained under three-point bending; for the blister test, a weakening of the interface toughness should be performed over a circular annulus prior to the coating deposition.

The measurement methods have been adapted to measure the adhesion of thin coatings: first on the interface TiN/steel to set up the methodology; afterwards on the interface Cu/steel.

The wedge opening test has been adapted to measure the interface toughness of thin films. The methodology has been set up by looking at titanium nitride films which is a system important for surface hardening on machine tools. The importance of the etching has been illustrated not only to promote adhesion but also to obtain a better uniformity of the adhesion all over the substrate. The mean value of the measured interface toughness is equal to $6\,\mathrm{J/m^2}$ but with large variations between 0.5 and $20\,\mathrm{J/m^2}$. Testing thin film adhesion requires to bond

an additional plate on top of the coating to store the energy needed to propagate the crack. An adhesive layer is thus needed to bond this extra layer which brings extrinsic phenomenons. Relaxation taking place in the adhesive layer has been quantified by measuring the crack length at different times after the wedge insertion. Now, more quantitative analysis was prevented due to the large scatter in the data —due to the absence of etching during the deposition process— making impossible further analysis of the origin and mechanisms of adhesion.

The wedge opening test has been applied on copper coatings to measure the evolution of the interface toughness with the coating thickness. The adhesion varies from $10\,\mathrm{J/m^2}$ for a $0.5\,\mu\mathrm{m}$ thick coating to less than $1\,\mathrm{J/m^2}$ for a $2.5\,\mu\mathrm{m}$ thick coating. These results match with the empirical tests performed routinely in the industry. Moreover, the low values at $2.5\,\mu\mathrm{m}$ explains the spontaneous decohesion observed during deposition when the deposition is not made within optimal conditions.

The mechanical properties of the layer close to the cracking interface influences the value of the interface toughness. They have been determined and used within a numerical model of the wedge opening test.

In addition to the work of adhesion and strength of the interface, other features control the level of interface toughness. The main characteristics are the internal stress and yield strength of the coating. The coating properties have been determined for each thickness. The internal stress of the coating increases with the thickness up to a coating thickness of about $1\,\mu\mathrm{m}$ and remains constant for thicker coatings. The value of the yield strength has not been measured during this work. The evolution of the yield strength with the thickness of the coating has been extracted from literature data. As expected when dealing with thin films, the strength increases with decreasing film thickness. Now, the adhesive layer —required to perform the wedge opening test— also plays a role and introduces an extrinsic contribution. The mechanical properties of the adhesive have also been determined, especially the yield strength.

The characteristics of the coating and of the other layers of the specimen have been used to simulate the wedge opening test using a FE simulation model. This model relies 2D plane-strain, steady-state, finite element

formulation. It assumes plane strain conditions and three-dimensional effects are neglected.

The contribution of the internal stress in the coating and the influence of the adhesive layer (required to perform the test) have been addressed using FE simulations.

An idealised model of the wedge opening test has been studied using the FE methods. It is a symmetric model smaller than the real specimen used for the experimental tests. This ideal model has been used to determine the influence of the internal stress and of the adhesive layer on the interface toughness measurement. Both effects are related, affecting mainly the plastic response of the specimen. Internal stress in the coating makes plastic deformation easier, increasing the plastic dissipation , hence the interface toughness. But, plastic deformation allows relaxing a larger part of the internal stress of the layer during cracking even though the layer still sticks on the other substrate and cannot freely contract or elongate. This effect has a negative impact on the resistance to cracking. The yield strength determines the plastic behaviour of the coating. A high value of the yield strength means less plastic deformation, allowing less internal stress relaxation.

The experimental data has been compared with numerical results to extract the contribution of each layer of the specimen to the total energy release rate. The intrinsic value, which is the interface toughness, has been determined from these different contributions.

Finally, comparisons have been made between the experimental measurements and numerical results on a more realistic model of the wedge opening test. The study has been performed on different values for the coating and the interface parameters. The values giving the best agreement with experimental results are $\Gamma_0 = 0.81\,\mathrm{J/m^2}$; $\hat{\sigma} = 1.2\,\mathrm{GPa}$ and the higher variation of the internal stress (see Fig. 6.12 on page 113).

The evolution of the simulation results follows the evolution of the experimental data though significantly underestimating the drop of interface toughness when the coating thickness increases. Another influence

comes from the mechanical characteristics of the copper layer. They have been taken from the literature but the coatings deposited during this study do not have the same microstructure. The mechanical parameters of the copper coatings deposited and of the adhesive layer used during this thesis should be measured in order to verify if they constitute the reason for the limited accuracy of the model predictions.

As a general conclusion, this study shows that a low interface toughness is always more easy to investigate: the tests are more simple to perform and the extrinsic contribution is lower; it gets to an interface adhesion problem. When the interface toughness becomes larger, more complex mechanical phenomenon and plastic deformation should be taken into account, extending the problem to other phenomena associated to the mechanics of thin films.

An important part of this work has also been devoted to the **transfer of the methodology to industry**, which is not straightforward. The wedge opening test does not directly provides the interface toughness and can hardly become a daily test made to certify the coating adhesion. But the wedge opening test could from now being used in for research and development purposes of new coatings deposition parameters. While measuring the adhesion of two same coatings to verify the influence of one deposition parameter, the extrinsic part of the energy measured would be similar for the two coatings. The values can thus be compared to optimise the deposition parameters. It can also be used to verify that the adhesion is conserved from the small scale deposition to the large scale deposition made on the industrial line.

The scientific point of view and the industrial point of view have been brought together. Both have a different final objectives but the ways to achieve them can be similar.

Perspectives

The wedge opening test is useful and easy to perform. Nevertheless, it can not be used as a daily adhesion measurement test in the industry.

Improvement can be made on the wedge opening test to measure a more accurate value of the interface toughness. Most difficulties comes from the adhesive needed to bond the extra substrate. This adhesive can fail if the bonding has not been properly made but the main issue is that it dissipates energy, especially for thin coatings. This dissipation gets important for thicknesses in the range of interest in many applications of ArcelorMittal. A solution could be to use an adhesive with higher strength or to braze the upper substrate. Another way to solve the problem is to deposit an elastic layer before bonding the additional substrate. In this case, we should then take care to not change the properties of the specimen, especially the internal stress of the coating.

The simulations presented here could be run over a larger range of parameters in order to generate abacus from which any user could separate the different energy contributions.

Now, the out of plane displacement measurement of the specimen using a profilometer only allows static testing, i.e. with a fixed wedge. Instantaneous measurement of the specimen out of plane displacement would allow to perform dynamic testing and determine the influence of the delamination speed. Optical methods like interferometry —used for the blister test— could be an interesting perspective in this direction.

Other attempts can be made with the superlayer test. Testing devices holds on a small piece of silicon that can be easily put on the coated substrate. Attention has also to be paid to the dissipation in the superlayer similar to the problem with adhesive layer in the wedge opening test. Now, the superlayer will usually be a much harder material.

The step following the development of an adhesion measurement technique is to investigate ways to improve the interface toughness. We have seen in this thesis that the surface preparation is of course very important. The surface has to be cleaned both mechanically and chemically and all deposition steps have to be made with meticulous care. We also have seen that the interface toughness is dependent on the energy dissipated in the entire system. Another way to improve the interface toughness is to favour plastic dissipation in the coating or substrate or to add on purpose a dissipative layer (see [8]).

Part IV

Appendix

Appendix A

Energy release rate for a double cantilever beam

The interface crack between two layers has been studied using an analytical approach [43, 65]. The problem is a double cantilever beam (DCB) of width w submited to a general loading configuration. The loading considered in the literature references is taken per unit width. In this development, we will explicitly divide the loading by the width of the beam w. The geometry of the problem, first studied by Suo and Hutchinson, is described in the figure A.1.

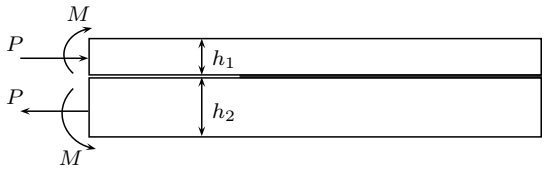

Figure A.1: General geometry of a double contilever problem made of two different layers subjected to axial loads and bending moments.

The energy release rate associated with the bending moment M is given by [43].

$$\bar{E}_1 \mathcal{G}_M = f_M^2(\alpha, H) M^2 w^{-2} h_1^{-3} \ , \tag{A.1}$$

where α is one of the Dundur parameter and $H = h_1/h_2$. $f_M(\alpha, H)$ is a constant given by

$$f_M^2(\alpha, H) = 6\left[1 + \left(\frac{1+\alpha}{1-\alpha}\right) H^3\right] \ . \tag{A.2}$$

The magnitude of the energy release rate associated with the axial loading P is given by

$$\bar{E}_1 \mathcal{G}_P = f_P^2(\alpha, H) P^2 w^{-2} h_1^{-1} \ , \tag{A.3}$$

where

$$f_P^2(\alpha, H) = 0.5 + \left(\frac{1+\alpha}{1-\alpha}\right)\left(1.5H^3 + 3H^2 + 2H\right) \ . \tag{A.4}$$

The energy release rate for an arbitrary combinaison of bending moment and axial loading can be determined by vectorial addition of the corresponding complex intensity factors given by

$$|K_i| = \sqrt{\left(\frac{1-\alpha}{1-\beta^2}\right) \bar{E}_1 \mathcal{G}_i} \ , \tag{A.5}$$

where i refers to the bending moment or to the axial loading and β is the second Dundur parameter.

Knowing the phase angle associated with the bending moment ψ_M and the axial loading ψ_P, the energy release rate for a combinaison of bending moment and axial loading is given by

$$\mathcal{G} = \mathcal{G}_P + \mathcal{G}_M + 2\left(\mathcal{G}_P \mathcal{G}_M\right)^{1/2} \cos \gamma_{PM} \ , \tag{A.6}$$

where

$$\gamma_{PM} = \psi_P - \psi_M = \cos^{-1}\left(\left(\frac{1+\alpha}{1-\alpha}\right) \frac{3H^2}{f_M(\alpha, H) f_P(\alpha, H)}\right) \ . \tag{A.7}$$

The results of Suo and Hutchinson [65] allow the calculation of the energy release rate when only bending moment and axial load act at the crack tip. In general, a transverse shear force V is also present at the

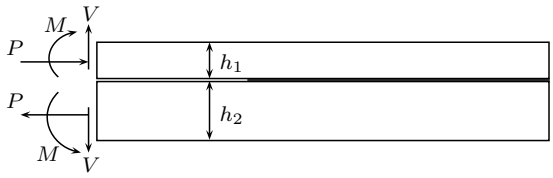

Figure A.2: General geometry of a double contilever problem made by two different layers subjected to axial loads, bending moments and transverse shear loads.

crack tip. The study of Li et al. [43] adds a shear force to the expression of the energy release rate. The geometry of the problem is given in Fig. A.2.

The energy release rate associated to pure shear force acting at the crack tip is given by the relation

$$\bar{E}_1 \mathcal{G}_V = f_V^2(\alpha, \beta, H) V^2 w^{-2} h_1^{-1} \ . \tag{A.8}$$

The expression is very similar to the expression regarding the bending moment (A.1) or the axial load (A.3) but analytical expression of $f_V(\alpha, \beta, H)$ does not exist. Values of $f_V(\alpha, \beta, H)$ for a few values of α and H with $\beta = 0$ can be found in [43].

The expression of the energy release rate regarding a arbitrary combinaison of axial load P, bending moment M and transverse load V is given by

$$\begin{aligned}\bar{E}_1 \mathcal{G} = f_P^2(\alpha, H) \frac{P^2}{w^2 h_1} \Bigg[1 + 2 \left(\frac{f_M(\alpha, H)}{f_P(\alpha, H)} \right) \left(\frac{M}{P h_1} \right) \cos \gamma_{PM} \\ + 2 \left(\frac{f_V(\alpha, H)}{f_P(\alpha, \beta, H)} \right) \left(\frac{V}{P} \right) \cos \gamma_{PV} \Bigg] \\ + f_M^2(\alpha, H) \frac{M^2}{w^2 h_1^3} \Bigg[1 + \left(\frac{f_V(\alpha, \beta, H)}{f_M(\alpha, H)} \right)^2 \left(\frac{V h_1}{M} \right)^2 \\ + 2 \left(\frac{f_V(\alpha, \beta, H)}{f_M(\alpha, H)} \right) \left(\frac{V h_1}{M} \right) \cos \gamma_{MV} \Bigg] \ ,\end{aligned} \tag{A.9}$$

where

$$\gamma_{PM} = \psi_P(\alpha,\beta,H) - \psi_M(\alpha,\beta,H) \ ,$$
$$\gamma_{PV} = \psi_P(\alpha,\beta,H) - \psi_V(\alpha,\beta,H) \ ,$$
$$\gamma_{MV} = \psi_M(\alpha,\beta,H) - \psi_V(\alpha,\beta,H) \ .$$

In the present work, the configuration considered is a DCB with a crack length a with an imposed displacement D between the two arms of the specimen. The crack tip is subjected to transverse shear force V, a bending moment M and no axial load. The expression of the shear force is taken from the loading necessary in the end of a build-in beam to impose a maximum deflexion of D and equal to

$$V = \frac{3D\bar{E}I}{2a^3} \ , \tag{A.10}$$

where I is the inertia moment of the beam.

The bending moment is expressed as

$$M = Va = \frac{3D\bar{E}I}{2a^2} \ . \tag{A.11}$$

The energy release rate, obtained from (A.9), is equal to

$$\bar{E}_1\mathcal{G} = f_M^2(\alpha,M)\frac{9D^2E^2I^2}{4a^4h_1^3w^2}\left[1 + \left(\frac{f_V(\alpha,\beta,H}{f_M(\alpha,H)}\right)^2\left(\frac{h_1}{a}\right)^2 + 2\left(\frac{f_V(\alpha,\beta,H}{f_M(\alpha,H)}\right)\left(\frac{h_1}{a}\right)\cos\gamma_{MV}\right] \ , \tag{A.12}$$

where $f_M(\alpha,M)$ is given by Eq. (A.2) and tables with a few values of $f_V(\alpha,\beta,H)$, $\psi_M(\alpha,\beta,M)$ and $\psi_V(\alpha,\beta,H)$ are given in [43]. The second moment of area I of the beam is given by

$$I = \frac{wh^3}{12} \ . \tag{A.13}$$

In the particular of the present work, the geometry is symetrical and the materials of the two beams are the same, giving $\alpha = \beta = 0$, $H = 1$

and $\psi_M = \psi_V = \gamma_{MV} = 0$. In this particular case, $f_M(0,1) = \sqrt{12}$ and $f_V(0,0,1) = 2.335$. Eq. (A.12) reduces to

$$\mathcal{G} = \frac{3\bar{E}h^3D^2}{16a^2}\left(1 + 0.674\frac{h}{a}\right)^2 \quad , \tag{A.14}$$

which is equal to the expression (4.1) used to determine the adhesion of the coating with the wedge opening test.

Appendix B

Plans of the testing stage

The following pages shows the plans of the testing stage used for the wedge opening test. The different parts are made in aluminium but the screws are in stainless steel.

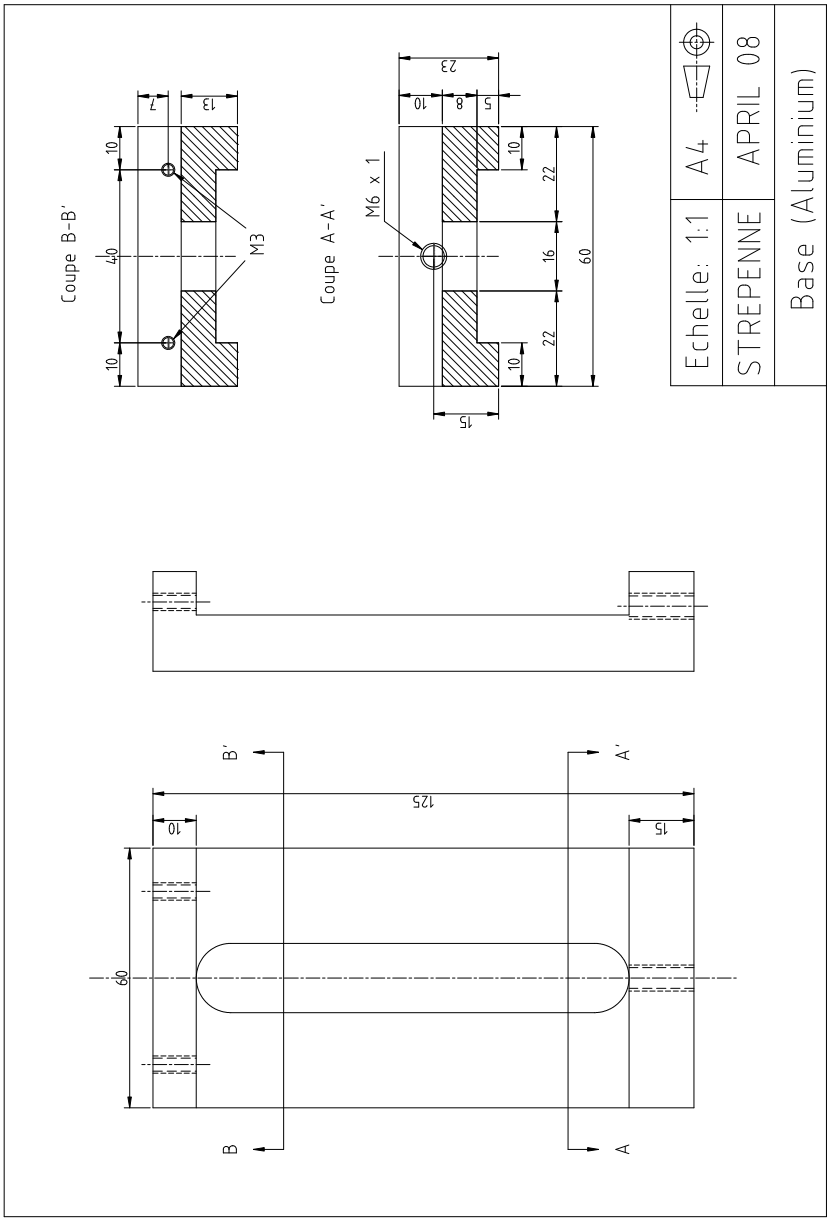
Coupe B-B'
Coupe A-A'
M3
M6 x 1
Echelle: 1:1
A4
STREPENNE
APRIL 08
Base (Aluminium)
125
60
B'
A'
B
A

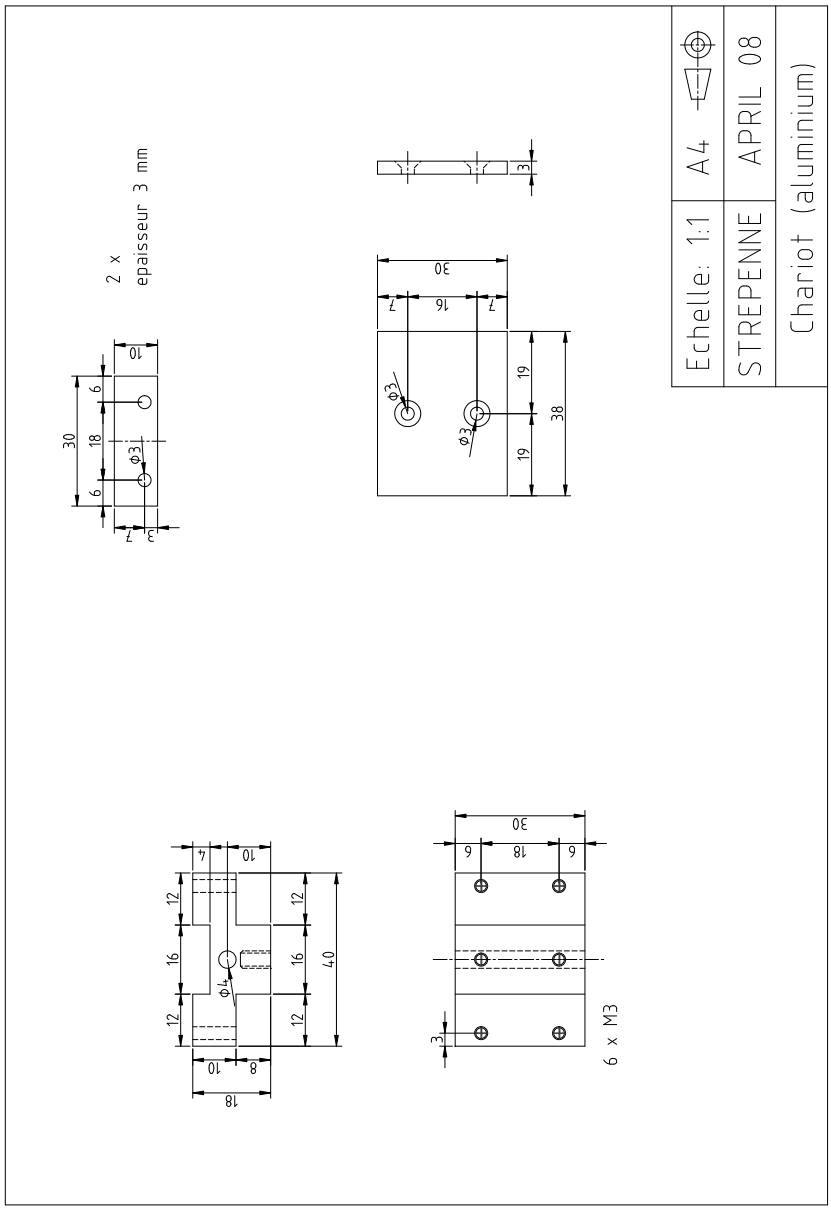
Echelle: 1:1
A4
STREPENNE
APRIL 08
Chariot (aluminium)
2 x
epaisseur 3 mm
30
18
6
6
10
Φ3
7
3
30
16
7
7
3
Φ3
Φ3
19
19
38
12
16
12
12
16
12
4
10
Φ4
40
10
8
18
30
6
18
6
3
6 x M3

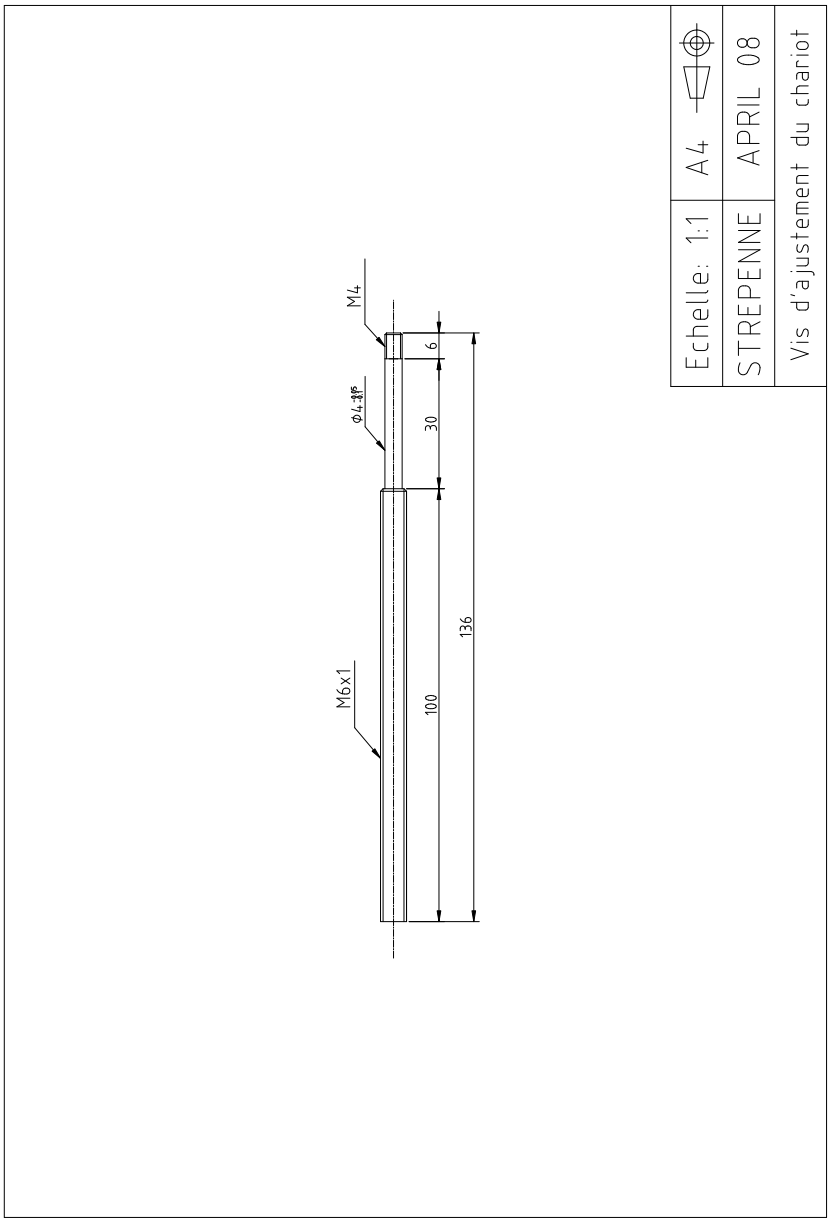
M4
6
30
136
M6x1
100
Echelle: 1:1
A4
STREPENNE
APRIL 08
Vis d'ajustement du chariot

Appendix C

Numerical program used to determine the crack length

The program used to determine the crack length from the experimental specimen profile is shown in detail below. It is a Scilab program which has been last tested with Scilab version 5.1.1.

```
// ************************************************************* //
//                                                               //
// - Program Ramlog                                              //
//                                                               //
// - by Francois Strepenne                                       //
// - version 5                                                   //
//                                                               //
// - Compute the length of a crack from the deformed profile     //
//   of the sample measured using a profilometer                 //
//                                                               //
// ************************************************************* //
//
clear()

// ------------------------------------------------------------- //
// Data fitting function

function [crack,R_square,err] = dektakRamlogDP(xdata,ydata,bh);

  // x and y in mm
  xdek = xdata;
  ydek = ydata - bh;

  // Determination of the points used to fit the analytical function
  i = 1;
  while ( ydek(i) > D/2 ),
    i = i + 1 ;
  end

  j = 1;
```

```
  while ( ydek(j) > D/2 * 0.05 ),
    if j == length(ydek),
      break
    end
    j = j + 1 ;
  end

  xdekfit = xdek(i:j) ;
  ydekfit = ydek(i:j) ;

  // Computation of the parameters to fit the experimental data's
  mprintf('%s\n','- Begin optimisation ...')
  [p,err_o]=datafit(fun,[xdekfit;ydekfit],[6;-1*xdekfit(1)]);
  mprintf('%s\n\n','- ... optimisation terminated')

  a = p(1)
  x0 = p(2)

  // translation of the experimental points
  xtrans = xdekfit + x0;

  ythDP = ((D/2) / (4/3*(1-nu)*(a.^2/h^2) + 1)) .* ( ...
    ((4*(1-nu)*a.^2)/(3*h^2) + 1) + ...
    ((nu/(2*a)) - (2*a*(1-nu))/(h^2)).*(xtrans) + ...
    ((2*(1-nu))/(3*a*h^2)).*(xtrans).^3 ) ;

  Xtrans = [0:0.01:a]';

  YthDP = ((D/2) / (4/3*(1-nu)*(a.^2/h^2) + 1)) .* ( ...
    ((4*(1-nu)*a.^2)/(3*h^2) + 1) + ...
    ((nu/(2*a)) - (2*a*(1-nu))/(h^2)).*(Xtrans) + ...
    ((2*(1-nu))/(3*a*h^2)).*(Xtrans).^3 ) ;

  scf()
  plot2d(xtrans'./a,ydekfit',style=-1);
  plot2d(Xtrans'./a,YthDP',style=2);
  xtitle("Optimisation result","x/a [-]","u_y [microns]")

  // error computation
  SSR = sum((ythDP-mean(ydekfit)).^2);
  SSE = sum((ydekfit-ythDP).^2);

  // outputs
  R_square = SSR/(SSR+SSE);
  crack = p(1);

endfunction

// ------------------------------------------------------------------ //
// Analytical displacement function

function y = fun(p,z) // z = points of the profile
                      // p = parameter vector (crack length + transl)

y = z(2) - ...
    ((D/2) / (4/3*(1-nu)*(p(1).^2./h^2) + 1)) .* ( ...
    ((4*(1-nu)*p(1).^2)/(3*h^2) + 1) + ...
    ((nu/(2*p(1)))) - (2*p(1)*(1-nu))/(h^2)).*(z(1)+p(2)) + ...
    ((2*(1-nu))/(3*p(1)*h^2)).*(z(1)+p(2)).^3 ) ;

endfunction

// ------------------------------------------------------------------ //
// File Reading from Dektak

function [datafile,xdata,ydata,sdatei,heurei,nbPoints,err]...
        = data_read();
```

```
  xdata = [];
100 ydata = [];
  sdatei = [];
  heurei = [];
  nbPoints = [];

  if (ext == 'CSVA'|ext == 'CSV'), // Dekta Veeco 6M
    if nbf < 10,
      datafile = dataPath + '0' + string(nbf) + '.csv';
    else,
      datafile = dataPath + string(nbf) + '.csv';
110   end

    [fid,err] = mopen(datafile,'r');
    if (err ~= 0)
      x_message_modeless(['could not find file';datafile;...
                    'Operation terminated with error '+string(err)]);
      return
    end

    gline=mgetl(fid,1);
120   gline=mgetl(fid,1);

    dh = msscanf(gline,'Date,%s %s');
    sdatei = dh(1);
    heurei = dh(2);

    while (%t)
      gline=mgetl(fid,1);
      if (meof(fid)~=0)
        x_message_modeless(['Wrong file open';...
130                           'eof reached without finding data']);
        return
      end
      line = msscanf(gline,'%c%c%c%s');
      if line(1:3) == ['N' 'u' 'm'],
        total = msscanf(line(4),'Pts,%i')-10;
      end
      if line(1) == '0',
        y1 = msscanf(line(4),'0,%g,,');
        data = [0.0 y1];
140     break
      end
    end // while

      data = mfscanf(-1,fid,'%g,%g,,');
    mclose([fid]);

    xbrut = data(:,1)' * 1e-3;// unit: microns
    ybrut = data(:,2)' * 1e-6;// unit: nm
    nbPoints = length(xbrut);
150 xdata = xbrut;
    ydata = ybrut;
  elseif ext == 'MOD'// Other profilometer
    if nbf < 10,
      datafile = dataPath + '0' + string(nbf) + '.MOD';
    else
      datafile = dataPath + string(nbf) + '.MOD';
    end

    [fid,err] = mopen(datafile,'r');
160 if (err ~= 0)
      x_message_modeless(['could not find file';datafile;...
                          'Operation terminated with error '+string(err)]);
      return
    end

    while (%t)
```

```
        gline=mgetl(fid,1);
        if (meof(fid)~=0)
          x_message_modeless(['Wrong file open';...
                              'eof reached without finding data']);
          return
        end
        line = msscanf(gline,'%c%c%c%s');
        if line(1:3) == ['N' 'U' 'M'],
          total = msscanf(gline,'NUMBER_MOD_POINTS %f');
          gline=mgetl(fid,1);
          data = mfscanf(-1,fid,'%g');
          break
        end
      end // while

      mclose([fid]);

      xdata = data(1:total)';          // unit: mm
      ydata = data(total+1:total*2)';// unit: mm
      nbPoints = total;
    else,
      disp('wrong file extension specified');
    end // if on extension

endfunction

// ------------------------------------------------------------------ //
// Output writing

function [] = output();

  mprintf('%s\n','-----------------------------------------')
  mprintf('%s\n','Data to copy :')

  if ext == 'CSVA', // Dektak Veeco 6M
    mprintf('%s\t%s\t%s\t%s\t%s\t%s\n',...
        'date    ','hour    ','biais    ','error   ','a [mm]   ','Gc [J/m^2]')
    for i = 1:length(a)
    mprintf('%f\t%f\t%f\t%f\t%f\t%f\n',sdatei(i),heurei(i),...
        biais(i),err_p(i),a(i),Gc(i))
    end
  elseif (ext == 'CSV'|ext == 'MOD'), // Dektak Veeco 150 of other
    mprintf('%s\t%s\t%s\t%s\t%s\n',...
        '# sample','biais','error','a [mm]','Gc [J/m^2]')
    for i = 1:length(a)
    mprintf('%i\t%6.4f\t%6.4f\t%7.4f\t%7.4f\n',...
        nbFiles(i),biais(i),err_p(i),a(i),Gc(i))
    end
  else,
    disp('I already said you want a wrong file extension...');
  end // if on extension


endfunction

// ********************************************************** //
//                        Main Program                        //
// ********************************************************** //

defaut = %f;
try
load('param.dat');
catch
defaut = %t;
end

// input parameters reading ------------------------------------ //
//
```

```
if defaut,
  params = x_mdialog('Unable to open file ''param.dat'', defaut values used',...
             ['data path';'file extension';'number of files';...
             'sample parameters (h E nu s_e b)';...
             'wedge thickness in microns'],...
             ['','CSV','1','0.4 200 0.3 215 10','100']);
else
  nf = length(nbFiles);
  tmp = string(nbFiles);
  nbfiles = tmp(1);
  for i = 2:nf,
    nbfiles = strcat([nbfiles,' ',tmp(i)]);
  end
  params = x_mdialog('Parameters input',...
             ['data path';'file extension';'number of files';...
             'sample parameters (h E nu s_e b)';...
             'wedge thickness in microns'],...
             [dataPath,ext,nbfiles,...
             msprintf('%1.1f %i %1.1f %i %i',Pech),...
             msprintf('%i',D*1e3)]);
end
if (isempty(params)),
  messagebox('Operation calcelled by user','end of program',"warning");
  return;
end

dataPath = params(1);
ext      = params(2);
nbFiles  = evstr(params(3));
Pech     = evstr(params(4));
D        = evstr(params(5))*1e-3;

save('param.dat',dataPath,ext,nbFiles,Pech,D)

h  = Pech(1);
E  = Pech(2);
nu = Pech(3);
se = Pech(4);
b  = Pech(5);

E = E/(1-nu^2); // plane strain with our geometry
//
// end input parameters reading ------------------------------------ //
//
mprintf('%s\n','Start calculation ...')

for nb = 1:length(nbFiles), // loop on different files
  nbf = nbFiles(nb);
  biais(nb) = 0;
  // data reading in the ith file form the dektak
  [datafile(nb),xdata,ydata,sdate(nb),heure(nb),nbPoints,err]...
    = data_read();
  if (err ~= 0)
    disp('End ...')
    return
  end

  // data fitting
  [a(nb),err_p(nb),err] = dektakRamlogDP(xdata,ydata,biais(nb));
  if (err ~= 0)
    disp('End ...')
    return
  end


  Gc(nb) = ((3*E*D^2*h^3)/(16*a(nb)^4))...
           *(1+0.64*(h/a(nb)))^2...
           *1e6;
```

```
end// loop on different files

// output writing
output

mprintf('%s\n','... Finish')
```

Appendix D

Numerical values of the results of the FE simulations on the ideal system

The results of the FE simulations made on the ideal system (see Section 6.6) are shown in Table D.1 and Table D.2 on the next two pages.

Table D.1: Results of the FE simulations made on the ideal system without the adhesive layer. The parameters of the interface are $\hat{\sigma} = 2\,\mathrm{GPa}$ and $\Gamma_0 = 1.34\,\mathrm{J/m^2}$.

t^{f}	σ_0^{f}	σ_i^{f}	Γ_p^{s}	Γ_p^{adh}	Γ_p^{f}	Γ_{el}^{s}	$\Gamma_{el}^{\mathrm{adh}}$	Γ_{el}^{f}	$\Gamma_{el}^{\mathrm{f}}\big\vert_{up}$	$\Gamma_p^{\mathrm{f}}\big\vert_{up}$	$\mathcal{G}(\zeta\sigma_i)$	$\mathcal{G}$
[μm]	[MPa]	[MPa]	$[\mathrm{J/m^2}]$	$[\mathrm{J/m^2}]$	$[\mathrm{J/m^2}]$	$[\mathrm{J/m^2}]$	$[\mathrm{J/m^2}]$	$[\mathrm{J/m^2}]$	$[\mathrm{J/m^2}]$	$[\mathrm{J/m^2}]$	$[\mathrm{J/m^2}]$	$[\mathrm{J/m^2}]$
0.5	500	0	82.680	-	4.364	1.600	-	0.400	0.000	0.000	0.000	179.4
0.5	500	250	67.370	-	4.035	1.230	-	0.390	0.149	0.022	0.149	147.4
0.5	500	500	45.590	-	3.690	1.230	-	0.410	0.593	0.091	0.581	103.2
0.5	500	550	32.650	-	3.390	1.600	-	0.420	0.633	0.190	0.608	77.46
1	500	0	4.372	-	3.281	0.100	-	0.013	0.000	0.000	0.000	16.87
1	500	250	4.000	-	4.200	0.056	-	0.085	0.295	0.045	0.133	17.34
1	500	500	2.870	-	5.272	0.056	-	0.162	1.180	0.180	0.634	15.33
1	500	550	2.330	-	5.350	0.056	-	0.181	1.260	0.378	0.655	13.89
10	500	0	0.000	-	3.135	0.001	-	0.000	0.000	0.000	0.000	7.61
10	500	250	0.000	-	3.580	0.436	-	2.040	2.710	0.400	0.054	6.92
10	500	500	0.193	-	9.940	1.230	-	5.450	10.810	4.650	0.936	8.8
0.5	∞	0	0.000	-	0.000	0.000	-	0.000	0.000	0.000	0.000	1.34
0.5	∞	250	0.000	-	0.022	0.002	-	0.146	0.148	0.022	0.000	1.34
0.5	∞	500	0.001	-	0.090	0.006	-	0.583	0.593	0.091	0.000	1.33
0.5	∞	550	0.002	-	0.106	0.006	-	0.708	0.718	0.109	0.000	1.34
1	∞	0	0.000	-	0.000	0.000	-	0.000	0.000	0.000	0.000	1.34
1	∞	250	0.005	-	0.044	0.002	-	0.286	0.295	0.045	0.000	1.33
1	∞	500	0.007	-	0.171	0.020	-	1.147	1.180	0.180	0.000	1.3
1	∞	550	0.003	-	0.206	0.030	-	1.389	1.426	0.220	0.000	1.29
10	∞	0	0.000	-	0.000	0.000	-	0.000	0.000	0.000	0.000	1.34
10	∞	250	0.312	-	0.302	0.225	-	1.980	2.710	0.400	0.006	0.37
10	∞	500	0.869	-	1.170	1.470	-	7.880	10.810	1.650	0.231	−2.75
10	∞	550	1.308	-	1.400	1.225	-	9.550	13.110	1.970	0.281	−3.35

Table D.2: Results of the FE simulations made on the ideal system with the adhesive layer. The parameters of the interface are $\hat{\sigma} = 2\,\mathrm{GPa}$ and $\Gamma_0 = 1.34\,\mathrm{J/m^2}$.

t^{f}	σ_0^{f}	σ_i^{f}	Γ_p^{s}	Γ_p^{adh}	Γ_p^{f}	Γ_{el}^{s}	$\Gamma_{el}^{\mathrm{adh}}$	Γ_{el}^{f}	$\Gamma_{el}^{\mathrm{f}}\big\vert_{up}$	$\Gamma_p^{\mathrm{f}}\big\vert_{up}$	$\mathcal{G}(\zeta\sigma_i)$	$\mathcal{G}$
[μm]	[MPa]	[MPa]	$[\mathrm{J/m^2}]$	$[\mathrm{J/m^2}]$	$[\mathrm{J/m^2}]$	$[\mathrm{J/m^2}]$	$[\mathrm{J/m^2}]$	$[\mathrm{J/m^2}]$	$[\mathrm{J/m^2}]$	$[\mathrm{J/m^2}]$	$[\mathrm{J/m^2}]$	$[\mathrm{J/m^2}]$
0.5	500	0	0.934	2.420	4.930	0.004	0.000	0.100	0.000	0.000	0.000	16.26
0.5	500	250	1.220	2.440	5.530	0.006	0.001	0.121	0.149	0.022	0.125	17.19
0.5	500	500	1.240	2.500	5.900	0.012	0.002	0.156	0.593	0.091	0.477	17.05
0.5	500	550	1.040	2.300	5.850	0.006	0.001	0.156	0.635	0.190	0.515	16.26
1	500	0	0.000	0.082	3.877	0.000	0.000	0.002	0.000	0.000	0.000	9.26
1	500	250	0.017	0.067	3.476	0.001	0.000	0.288	0.295	0.045	0.003	8.32
1	500	500	0.002	0.313	4.320	0.001	0.000	0.450	1.180	0.182	0.212	8.78
1	500	550	0.002	0.312	4.540	0.001	0.000	0.450	1.265	0.379	0.249	8.65
10	500	0	0.000	0.000	3.698	0.001	0.000	0.000	0.000	0.000	0.000	8.75
10	500	250	0.060	0.002	2.960	0.625	0.048	1.020	2.622	0.418	0.349	3.48
10	500	500	1.110	0.039	4.600	1.230	0.169	4.500	10.630	1.640	1.340	−4.58
10	500	550	0.876	0.044	6.430	1.600	0.176	5.120	12.550	2.430	1.685	−5.07
0.5	∞	0	0.000	0.000	0.000	0.000	0.000	0.000	0.000	0.000	0.000	1.35
0.5	∞	250	0.002	0.000	0.021	0.002	0.003	0.140	0.148	0.022	0.000	1.33
0.5	∞	500	0.003	0.000	0.085	0.016	0.001	0.562	0.593	0.091	0.000	1.28
0.5	∞	550	0.006	0.000	0.103	0.016	0.001	0.679	0.718	0.110	0.001	1.26
1	∞	0	0.000	0.000	0.000	0.000	0.000	0.000	0.000	0.000	0.000	1.34
1	∞	250	0.000	0.000	0.040	0.016	0.001	0.265	0.295	0.045	0.001	1.27
1	∞	500	0.028	0.000	0.158	0.042	0.005	1.058	1.180	0.182	0.011	1.06
1	∞	550	0.060	0.001	0.191	0.025	0.005	1.280	1.431	0.136	0.012	1
10	∞	0	0.000	0.000	0.000	0.000	0.000	0.000	0.000	0.000	0.000	1.35
10	∞	250	0.318	0.012	0.092	0.400	0.052	1.070	2.670	0.391	0.362	−2.33
10	∞	500	1.966	0.055	0.399	0.900	0.208	4.230	10.720	1.520	1.480	−13.35
10	∞	550	2.288	0.070	0.432	1.230	0.252	5.120	12.950	1.860	1.790	−16.53

Bibliography

[1] `http://brycoat.com/pvd-tin.html`, last visited on 18$^{\text{th}}$ march 2010.

[2] R. Abermann and R. Koch, *In situ study of thin film growth by internal stress measurement under ultrahigh vacuum conditions: Silver and copper under the influence of oxygen*, Thin Solid Films **142** (1986), no. 1, 65–76.

[3] A. Bagchi and A.G. Evans, *The mechanics and physics of thin film decohesion and its measurement*, Interface science **3** (1996), 169–193.

[4] A. Bagchi, G.E. Lucas, Z. Suo, and A.G. Evans, *A new procedure for measuring the decohesion energy for thin ductile films on substrates*, Journal of material research **9** (1994), no. 7, 1734–1741.

[5] E. Barthel, O. Kerjan, P. Nael, and N. Nadaud, *Asymmetric silver to oxide adhesion in multilayers deposited on glass by sputtering*, Thin solid films **473** (2005), 272–277.

[6] Y. Bertholet, *Measurement, optimisation and multiscale modeling of silicon wafer bonding interface fracture resistance*, Ph.D. thesis, Université catholique de Louvain, 10 2006.

[7] Y. Bertholet, F. Iker, J.-P. Raskin, and T. Pardoen, *Steady-state measurement of wafer bonding cracking resistance*, Sensors and Actuators A **110** (2004), 157–163.

[8] Y. Bertholet, B. Olbrechts, B. Lejeune, J.-P. Raskin, and T. Pardoen, *Molecular bonding aided by dissipative inter-layers*, Acta Materialia **55** (2007), no. 2, 473–479.

[9] B. Bhushan, *Springer handbook of nanotechnology*, 2 nd ed., Springer, 1997.

[10] A. Billard and F. Perry, *Pulvérisation cathodique magnétron*, Traitement sous vide Techniques de l'ingénieur (2005), M 1 654–1–17.

[11] S.J. Bull and E.G. Berasetegui, *An overview of the potential of quantitative coating adhesion measurement by scratch testing*, Tribology International **39** (2006), no. 2, 99–114.

[12] P.G. Charalambides, J. Lund, A.G. Evans, and McMeeking, *A test specimen for determining the fractrure resistance of bimaterials interfaces*, Journal of Applied Mechanics **56** (1989), 77–82.

[13] B. Cotterell, K. Hbaieb, J.G. Williams, H. Hadavinia, and V. Tropsa, *The root rotation in double cantilever beam and peel tests*, Mechanics of Materials **38** (2006), no. 7, 571–584.

[14] R. H. Dauskardt, M. Lane, Q. Ma, and N. Krishna, *Adhesion and debonding of multi-layer thin film structures*, Engineering Fracture Mechanics **61** (1998), no. 1, 141–162.

[15] R.H. Dean and J. W. Hutchinson, *Quasi-static steady crack growth in small-scale yielding*, Fracture Mechanics: 12th Conference, ASTM STP 700, American Socciety for Testing and Materials, 1980, pp. 383–405.

[16] I. Doghri, *Mechanics of deformable solids*, Springer-Verlag, 2000.

[17] T. Ferracin, C. M. Landis, F. Delannay, and T. Pardoen, *On the determination of the cohesive zone properties of an adhesive layer from the analysis of the wedge-peel test*, International Journal of Solids and Structures **40** (2003), no. 11, 2889–2904.

[18] J.A. Floro, E. Chason, and S.R. Lee, *Real time measurement of epi-layer strain using a simplified wafer curvature technique*, Materials Research Society Symposium Proceeding **405** (1996), 381–386.

[19] L. Francis, D. Flandre, T. Pardoen, and J.-P. Raskin, *Elec2895 : Mems design*, 2007.

[20] L.B. Freund and S. Suresh, *Thin film matherials*, Cambridge University press, 2003.

[21] S. Gravier, M. Coulombier, A. Safi, N. André, A. Boé, J.-P. Raskin, and T. Pardoen, *New on-chip nanomechanical testing laboratory – applications to aluminum and polysilicon thin films*, Journal of microelectromechanical systems **28** (2009), no. 3, 555–569.

[22] K. Hbaieb and Y.W. Zhang, *A parametric study of a pressurized blister test for an elastic-plastic film-rigid substrate system*, Materials Science and Engineering A **390** (2005), no. 1-2, 385–392.

[23] J.-L. He, Hon M.-H., Chung H.-S., and Shueh Y., *Behaviors of plasma enhanced cvd deposited tin on low carbon steel*, Plasma and Laser Processing of Materials (Metals & Materials Society K. Upadhya The Minerals, ed.), 1991.

[24] R. J. Hohlfelder, *Bulge and blister testing of thin films and their interfaces*, Ph.D. thesis, Stanford University, 1999.

[25] M. Hommel and O. Kraft, *Deformation behavior of thin copper films on deformable substrates*, Acta Materialia **49** (2001), no. 19, 3935–3947.

[26] M. A. Hopcroft, W. D. Nix, and T. W. Kenny, *What is the Young's modulus of silicon*, Journal of microelectromechanical systems **19** (2010), no. 2, 229–238.

[27] Z. Huang, Z. Suo, G. Xu, J. He, J. H. Prevost, and N. Sukumar, *Initiation and arrest of an interfacial crack in a four-point bend test*, Engineering Fracture Mechanics **72** (2005), no. 17, 2584–2601.

[28] Michael P. Hughey, Dylan J. Morris, Robert F. Cook, Steven P. Bozeman, Brian L. Kelly, Srinivas L. N. Chakravarty, David P. Harkens, and Laura C. Stearns, *Four-point bend adhesion measurements of copper and permalloy systems*, Engineering Fracture Mechanics **71** (2004), no. 2, 245–261.

[29] J.W. Hutchinson and Z. Suo, *Mixed-mode cracking in layered materials*, Advances in Applied Mechanics **29** (1992), 63–191.

[30] ISO-2409, *Paints and varnishes – cross-cut test*, Third edition 05 2007.

[31] ISO-4624, *Paints, varnishes and plastics – pull-off test for adhesion*, 05 2003.

[32] G.C.A.M. Janssen, M.M. Abdalla, F. van Keulen, B.R. Pujada, and B. van Venrooy, *Celebrating the 100th anniversary of the stoney equation for film stress: Developments from polycrystalline steel strips to single crystal silicon wafers*, Thin Solid Films **517** (2009), no. 6, 1858–1867.

[33] M.F. Kanninen, *An augmented double cantilever beam model for studying crack propagation and arrest*, International Journal of Fracture **9** (1973), no. 1, 83–92.

[34] E. Klokholm and B. S. Berry, *Intrinsic stress in evaporated metal films*, J. Electrochem. Soc. **115** (1968), no. 8, 823–826.

[35] R Koch, *The intrinsic stress of polycrystalline and epitaxial thin metal films*, Journal of Physics: Condensed Matter **6** (1994), no. 45, 9519–9550.

[36] K. Kuwahara, T. Sumomogi, and M. Kondo, *Internal stress in aluminium oxide, titanium carbide and copper films obtained by planar magnetron sputtering*, Thin Solid Films **78** (1981), no. 1, 41–48.

[37] R. Lacombe, *Adhesion measurement methods*, Taylor & Francis, 2006.

[38] J. Laconte, F. Iker, S. Jorez, N. André, J. Proost, T. Pardoen, D. Flandre, and J.-P. Raskin, *Thin films stress extraction using micromachined structures and wafer curvature measurements*, Microelectronic Engineering **76** (2004), no. 1-4, 219–226.

[39] C. M. Landis, T. Pardoen, and J. W. Hutchinson, *Crack velocity dependent toughness in rate dependent materials*, Mechanics of Materials **32** (2000), no. 11, 663–678.

[40] J. Laurencin, *Amorçage et propagation d'une fissure à l'interface d'un bi-matériau*, Master's thesis, Concervatoire national des arts et métiers, 2002.

[41] B. Lawn, *Fracture of brittle solids*, Cambridge University press, 1993.

[42] C.-Y. Lee, *Metal/ceramic interface engineering - adhesion strength measurement between dielectric ceramic and electrode metal*, Ph.D. thesis, Université Joseph Fourier-Grenoble 1 and National Taiwan University, Taipei (R.O.C), 2007.

[43] S. Li, J. Wang, and M. D. Thouless, *The effects of shear on delamination in layered materials*, Journal of the Mechanics and Physics of Solids **52** (2004), no. 1, 193–214.

[44] P. Martiny, *CHADAQUS code: User's manual v1.0*, Cenaero, 2004.

[45] J.W. Matthews and A.E. Blakeslee, *Defects in epitaxial multilayers: I. misfit dislocations*, Journal of Crystal Growth **27** (1974), 118–125.

[46] M. B. Modi and Suresh K. Sitaraman, *Interfacial fracture toughness measurement for thin film interfaces*, Engineering Fracture Mechanics **71** (2004), no. 9-10, 1219–1234.

[47] J. Mougin, M. Dupeux, A. Galerie, and L. Antoni, *Inverted blister test to measure adhesion energy of thermal oxide scales on metals or alloys*, Materials Science and Technology **18** (2002), 1217–1220.

[48] D. Müller and E. Fromm, *Mechanical properties and adhesion strength of TiN and Al coatings on HSS, steel, aluminium and copper characterized by four testing methods*, Thin Solid Films **270** (1995), no. 1-2, 411–416.

[49] A. Needleman, *A continuum model for void nucleation by inclusion debonding*, J. Appl. Mech. **54** (1987), no. 3, 525–531.

[50] L. Nicola, Y. Xiang, J.J. Vlassak, E. Van der Giessen, and A. Needleman, *Plastic deformation of freestanding thin films: Experiments and modeling*, Journal of the Mechanics and Physics of Solids **54** (2006), 2089–2110.

[51] W. D. Nix, *Mechanical properties of thin films*, January 2005.

[52] O. Ohring, *Materials science of thin films: Deposition and structure*, second edition ed., Academic Press, 2002.

[53] B. Olbrechts, B. Lejeune, Y. Bertholet, T. Pardoen, and J.-P. Raskin, *Direct wafer bonding enhanced by ductile layers inserted near the interface*, ECS Transactions **3** (2006), no. 6, 279–289.

[54] J. Y. Pan, P. Lin, F. Maseeh, and S. D. Senturia, *Verification of fem analysis of load-deflection methods for measuring mechanical properties of thin films*, IEEE, New York, 1990.

[55] T. Pardoen, *Mapr2481 : Introduction to the deformation and fracture of matherials*, Université catholique de Louvain, 2005 ed.

[56] T. Pardoen, T. Ferracin, C.M. Landis, and F. Delannay, *Constraint effects in adhesive joint fracture*, Journal of the Mechanics and Physics of Solids **53** (2005), no. 9, 1951–1983.

[57] N.R. Philips, M.Y. He, and A.G. Evans, *A wedge fracture toughness test for intermediate toughness materials: Application to brazed joints*, Acta Materialia **56** (2008), no. 17, 4593–4600.

[58] B. C. Prorok, Y. Zhu, H. D. Espinoza, Z. Guo, S. P. Bazant, Y. Zhao, and B. I. Yakabson, *Micro- and nanomechanics*, Encyclopedia of Nanoscience and Nanotechnology **5** (2004), 555–600.

[59] J.-Y. Sener, T. Ferracin, L. Caussin, and F. Delannay, *On the precision of the wedge-opened double cantilever beam method for measuring the debonding toughness of adhesively bonded plates*, International Journal of Adhesion and Adhesives **22** (2002), no. 2, 129–137.

[60] A. Shirani and K.M. Liechti, *A calibrated frature process zone model for thin film blistering*, International Journal of Fracture **93** (1998), no. 1 - 4, 281–314.

[61] K.S. Sree Harsha, *Principles of vapor deposition of thin films*, first ed., Elsevier, Oxford, 2005.

[62] J. Stallard, S. Poulat, and D.G. Teer, *The study of the adhesion of a tin coating on steel and titanium alloy substrates using a multi-mode scratch tester*, Tribology International **39** (2006), no. 2, 159–166.

[63] G. Gerald Stoney, *The tension of metallic films deposited by electrolysis*, Proceedings of the Royal Society of London. Series A, Containing Papers of a Mathematical and Physical Character **82** (May 6, 1909), no. 553, 172–175.

[64] Z. Suo, *Reliability of interconnect structures*, Comprehensive Structural Integrity **8** (2002), 1–61.

[65] Z. Suo and J.W. Hutchinson, *Interface crack between two elastic layers*, International journal of fracture **43** (1990), 1–18.

[66] M. D. Thouless, J. L. Adams, M. S. Kafkalidis, S. M. Ward, R. A. Dickie, and G. L. Westerbeek, *Determining the toughness of plastically deforming joints*, Journal of materials science **33** (1998), 189–197.

[67] Timoshenko and Gere, *Mechanics of materials*, 4th ed., PWS Publishing Company, 1997.

[68] Q-Y Tong and U. Gësele, *Semiconductor wafer bonding science and technology*, Hohn wiley & sons, inc., 1999.

[69] V. Tvergaard, *Effect of fibre debonding in a whisker-reinforced metal*, Materials Science and Engineering: A **125** (1990), no. 2, 203–213.

[70] Ö. Vallin, K. Jonsson, and U. Lindberg, *Adhesion quantification methods for wafer bonding*, Materials Science and Engineering: R: Reports **50** (2005), no. 4-5, 109–165.

[71] J.J. Vlassak and Nix W.D., *A new bulge test technique for the determination of young's modulus and poisson's ratio of thin films*, Journal of Materials Research **7** (1992), 3242–3249.

[72] A. A. Volinsky, N. R. Moody, and W. W. Gerberich, *Interfacial toughness measurements for thin films on substrates*, Acta Materialia **50** (2002), no. 3, 441–466.

[73] Y. Wei and J. W. Hutchinson, *Nonlinear delamination mechanics for thin films*, Journal of the Mechanics and Physics of Solids **45** (1997), no. 7, 1137–1159.

[74] J. G. Williams and H. Hadavinia, *Analytical solutions for cohesive zone models*, Journal of the Mechanics and Physics of Solids **50** (2002), no. 4, 809–825.

[75] Y. Xiang, X. Chen, and J. Vlassak, *The mechanical properties of electroplated cu thin films measured by means of the bulge test technique*, Material Research Society Symposium Proceeding Vol. 695, 2002.

[76] Y. Xiang, X. Chen, and Joost J. Vlassak, *Plane-strain bulge test for thin films*, Journal of Materials Research **20** (2005), 2360–2370.

[77] Y. Xiang, T. Y. Tsui, and Joost J. Vlassak, *mechanical properties of freestanding electroplated Cu thin films*, Journal of Materials Research **21** (2006), 1607–1618.

[78] Y. Xiang and J.J. Vlassak, *Bauschinger and size effects in thin-film plasticity*, Acta Materialia **54** (2006), no. 20, 5449–5460.

[79] Z.H. Xie, M. Hoffman, R.J. Moon, and P.R. Munroe, *Deformation of a hard coating on ductile substrate system during nanoindentation: Role of the coating microstructure*, Journal of Materials Research **21** (2006), 437–447.

[80] J. Zheng and S. K. Sitaraman, *Fixtureless superlayer-driven delamination test for nanoscale thin-film interfaces*, Thin Solid Films **515** (2007), no. 11, 4709–4716.